View metadata, citation and similar papers at core.ac.uk

brought to you by CORE

provided by Illinois Digital Environment for Access to Learning and Scholarship Repository

University of Illinois at Urbana-Champaign

Air Conditioning and Refrigeration Center A National Science Foundation/University Cooperative Research Center

Critical Heat Flux of CO_2 in a Microchannel at Elevated Subcritical Pressures

J. P. Aldana, J. G. Georgiadis, and A. M. Jacobi

ACRC TR-195 March 2002

For additional information:

Air Conditioning and Refrigeration Center
University of Illinois
Mechanical & Industrial Engineering Dept.
1206 West Green Street
Urbana, IL 61801

(217) 333-3115

Prepared as part of ACRC Project #101
Transcritical CO_2: Understanding In-Tube Heat Transfer
J. G. Georgiadis and A. M. Jacobi, Principal Investigators

The Air Conditioning and Refrigeration Center was founded in 1988 with a grant from the estate of Richard W. Kritzer, the founder of Peerless of America Inc. A State of Illinois Technology Challenge Grant helped build the laboratory facilities. The ACRC receives continuing support from the Richard W. Kritzer Endowment and the National Science Foundation. The following organizations have also become sponsors of the Center.

Alcan Aluminum Corporation
Amana Refrigeration, Inc.
Arçelik A. S.
Brazeway, Inc.
Carrier Corporation
Copeland Corporation
Dacor
Daikin Industries, Ltd.
Delphi Harrison Thermal Systems
General Motors Corporation
Hill PHOENIX
Honeywell, Inc.
Hydro Aluminum Adrian, Inc.
Ingersoll-Rand Company
Kelon Electrical Holdings Co., Ltd.
Lennox International, Inc.
LG Electronics, Inc.
Modine Manufacturing Co.
Parker Hannifin Corporation
Peerless of America, Inc.
Samsung Electronics Co., Ltd.
Tecumseh Products Company
The Trane Company
Valeo, Inc.
Visteon Automotive Systems
Wolverine Tube, Inc.
York International, Inc.

For additional information:

Air Conditioning & Refrigeration Center
Mechanical & Industrial Engineering Dept.
University of Illinois
1206 West Green Street
Urbana, IL 61801

217 333 3115

Abstract

The connection between chlorofluorocarbons and ozone depletion has prompted a resurgence in the study of environmentally friendly refrigerants for heat exchanger applications. Recent studies have shown compact heat exchangers using a transcritical CO_2 cycle optimized in a microchannel geometry are competitive with baseline units in terms of physical dimension and thermal performance. However, the critical heat flux may occur at lower-than-expected vapor qualities in the heat absorption portion of the cycle, significantly affecting heat exchanger performance. The purpose of this study is to determine the critical heat flux and associated vapor quality under conditions simulating compact heat exchanger conditions. Non-intrusive wall temperature measurements, in conjunction with standard transducer measurements and flow visualization, were used to detect critical heat flux phenomenon. The vapor qualities associated with the critical heat flux were determined to be lower than would be expected in larger-diameter channels, and the critical heat flux was lower than predicted by the Shah correlation.

Table of Contents

List of Figures

Page

List of Tables

Page

Nomenclature

A	Area
Bo	Boiling Number = $\frac{q}{G \cdot i_{fg}}$
c_p	Specific Heat
D	Diameter
D_h	Hydraulic Diameter
DNB	Departure from Nucleate Boiling
G	Mass Flux
h	Heat Transfer Coefficient
i	Enthalpy
i_{fg}	Latent Heat of Vaporization
LCC	Shah Local Conditions Correlation
$\dot{m}$	Mass Flow Rate
P	Pressure
q	Power
q″	Heat Flux
T	Temperature
R	Heater Resistance
UCC	Shah Upstream Conditions Correlation
V	Volts
x	Vapor Quality
z	Axial Length
z_{eq}	Equivalent Axial Heating Distance (defined in Section 4)

Symbols

a	Temperature Coefficient
δ	Reduced Density (CO_2 Equation of State, Span & Wagner)
Ω	Ohms
?	Density
τ	Reduced Temperature (CO_2 Equation of State, Span & Wagner)
μ	Dynamic Viscosity

Subscripts

crit	Critical (Heat Flux)
d	Dry
e	Exit
f	Saturated liquid
g	Saturated vapor
H	Heated
i	Inlet
lat	Latent
o	Reference Parameter
r	Reduced Thermodynamic Property
sens	Sensible
sub	Subcooled
s	Surface (wall)
T	Total
w	Wet

Chapter 1: Introduction and Literature Review

1.1 Background

Carbon Dioxide (CO_2) was first proposed as a vapor-compression system refrigerant in 1850, and by the 1920s several companies in the US and Europe were manufacturing CO_2-based refrigeration systems (Bodinus, 1999). CO_2 remained a popular refrigerant until the introduction of chlorofluorocarbons (CFCs), which were developed in the early 1930s for use in industrial, commercial, and household applications. CFCs are inert, nontoxic, and nonflammable synthetic chemical compounds that have a high thermal capacitance and excellent transport properties in refrigeration systems. CFC-based refrigerants quickly became the industry standard, and CO_2 refrigeration systems were effectively phased out by the mid-1940s. CFC-12 was determined to have the best overall thermodynamic properties for a compact heat exchanger refrigerant in automotive air conditioning. DuPont became the leading industry manufacturer of R-12 (CFC-12 when used as a refrigerant) under the tradename Freon®.

In 1973, evidence emerged linking chlorine from CFCs with ozone destruction. Farman *et al.* (1985) presented conclusive evidence of stratospheric ozone loss over the Antarctic polar region, and subsequent studies clearly linked chlorine catalytic cycles with ozone depletion, prompting calls to reduce CFC production. These efforts culminated in the 1987 Montreal Protocol, which required developed countries to reduce the production and consumption of the fully halogenated Group I CFCs (those most responsible for ozone depletion, including CFC-12) to 80 percent of 1986 levels by 1994, and 50 percent of 1986 levels by 1999. The U.S. Senate unanimously ratified the protocol in March 1988 and the treaty became effective on January 1, 1989, signaling the whole-scale phase out of CFCs.

DuPont discontinued CFC production by 1996, and the automotive industry adopted R-134a as an environmentally friendly alternative. However, R-134a contains hydrofluorocarbons (HFCs), which have a global warming effect and require strict regulation. These characteristics prompted renewed interest in alternative, "natural" refrigerants including CO_2. Lorentzen and Pettersen (1992) advanced the concept of CO_2 in a transcritical cycle as potential next-generation automotive refrigerant. CO_2 is environmentally benign, cheap to produce, and readily available. CO_2 would be obtained from atmospheric air through a fractionation process, and have no additional impact on global warming. A CO_2-based transcritical cycle offers high volumetric heat capacity and excellent heat transfer properties.

Figure 1.1 shows the transcritical cycle on a temperature-entropy diagram. CO_2 undergoes compression (1-2), resulting in a supercritical state at the heat-rejection high-side (critical point = 7.383 MPa and 303.97K). The single-phase supercritical fluid undergoes isobaric heat rejection (2-3) in a gas cooler, rather than condensation as in conventional cycles. The system then undergoes adiabatic expansion (3-4), and heat absorption occurs through two-phase evaporation (4-1).

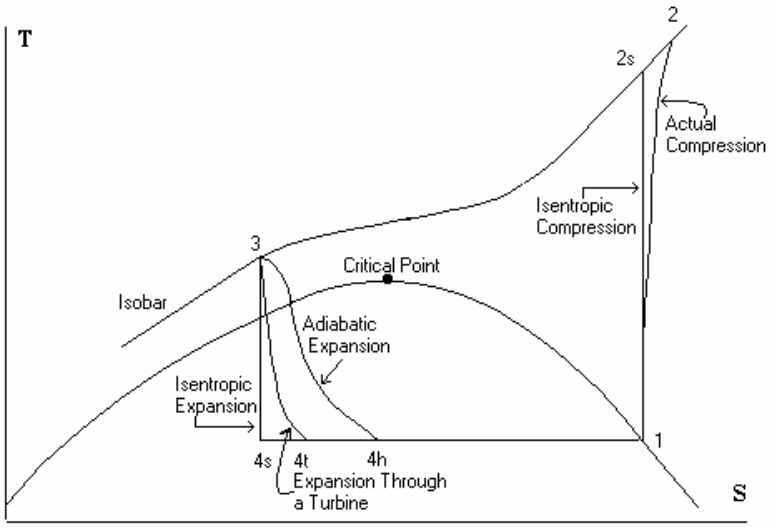

Figure 1.1 The Transcritical Cycle

Pettersen *et al*. (1998) outline developments in CO_2-based compact heat exchanger designs and thermodynamic cycle analyses, and provide an overview of performance tests and comparisons with baseline refrigerants (HCFC-22 and R-134a) for numerous successful prototype CO_2 heat exchangers. Transcritical CO_2 heat exchanger performance is optimized using a microchannel geometry, which maximizes heat transfer while reducing the dimensions, weight and available explosion energy (the product of pressure and volume). Pettersen and co-workers note that in this configuration CO_2-based compact heat exchangers are highly competitive with conventional systems with respect to physical dimensions and thermal performance.

While the system data are encouraging, there is a lack of information concerning local heat transfer coefficients and pressure drop characteristics of CO_2 in a microchannel. There have been significant (although often conflicting) research on single- and two-phase heat transfer in microchannels, and significant research on the effects of property variations in supercritical fluid heat transfer, but almost no research on the combined effects of the two. Questions concerning the application of standard correlations to supercritical and two-phase heat transfer in microchannel geometries must be answered in order to optimize compact heat exchanger designs.

This review is divided into three subsections. The first subsection refers to studies involving heat transfer and pressure drop characteristics of fluids in microchannel geometries. The second subsection is a review of studies performed with supercritical fluid heat transfer. The final subsection pulls together the available information pertaining to transcritical CO_2 in a microchannel geometry and the relationship of this thesis to the existing knowledge base.

1.2 Microchannel Heat Transfer Review

The advent of micro-scale devices and the need for heat transfer in high-density electronics have prompted several studies into convective heat transfer in microchannels that can be applied to compact heat exchangers (defined as heat exchanges with 700 m^2 surface area per m^3 core volume). Mehendale *et al*. (2000) provide a critical review summary of single- and two-phase heat transfer literature in microchannels, and note that there is no standard

for defining the maximum hydraulic diameter (D_h) for microchannels. "Micro-scale" in the literature often refers to studies applicable to high-density electronics (hydraulic diameter = 1-100 μm), while "meso-scale" is more applicable to compact heat exchanger dimensions (100 μm – 5 mm). However, in much of the literature microscale refers to channels of approximately D_h = 2mm or less, and that convention will be used throughout this thesis. Channels with D_h over 5 mm are generally considered macroscale dimensions.

1.2.1 Single Phase Studies - Fluid Flow and Heat Transfer Regimes

Much of the literature reviewed focused on deviations of microchannel flow and heat transfer characteristics from those predicted using standard correlations based on the Navier-Stokes equations for fully developed, incompressible, Newtonian fluids. Fluid flow in large channels shifts from laminar flow to a transition region at approximate Reynolds numbers (Re) of 2000, with fully developed turbulent flow at Re = 4000 (White, 1991). Several studies suggest the transition from laminar to turbulent regimes in microchannels occur at significantly lower Re numbers than for larger channels. Peng *et al.* (1994) studied single-phase liquid (water) flow characteristics in several microchannels with D_h ranging from 0.133-0.343 mm and a height-to-width ratio of 0.333-1. In this study Peng and coworkers observed that the crossover from laminar fluid flow to the transition region occurred at Re = 200 to 700, and that the transition region had a smaller Re number zone than for macro–sized channels. The authors note that for fully developed turbulent flow, friction factors were lower than predicted by the Blasius relation. These results differ from Wu and Little (1983) for gas (nitrogen) in trapezoidal microchannels, where D_h varied from 45 – 83 μm. Wu and Little observed a 30-250% friction-factor increase over the predicted Blasius-relation values, which they attribute to increased dependence on the microchannel surface roughness.

Associated with the transition to turbulence is an increase in random bulk fluid motion which enhances heat transfer due to thermal energy advection throughout the channel. Choi *et al.* (1991) observed the transition from laminar to turbulent heat transfer for single-phase gas (nitrogen) occurred at a Re = 2300 in very small circular microchannels (D_h ranged from 3-81 μm), with friction factors between 10% - 30% lower than those predicted by the Blasius relation. Wu and Little (1984) observed the transition to fully developed turbulent heat transfer occurred between Re = 1000 – 3000 for single-phase gas (nitrogen) flowing in trapezoidal channels with D_h ranging from 0.134-0.164 mm. The authors also determined the Nusselt numbers (Nu) were higher than predicted values by standard correlations, which they again attribute to surface roughness. Wu and Little suggest surface roughness dominates the pressure drop and heat transfer characteristics in very small channels.

Wang and Peng (1994) observed the transition from laminar heat transfer to the transition regime at Re = 300-800 for single-phase liquid (water or methanol) in rectangular microchannels with D_h = 0.331 – 0.747 mm. Wang and Peng also observed the transition to fully developed turbulent heat transfer occurred at Re between 1000-1500, while Peng and Peterson (1996) observed the onset of fully developed turbulent heat transfer in a single-phase liquid (water/methanol binary mixture) to occur at Re = 200-700. Peng *et al.* (1994) observed for single-phase liquid (water) laminar heat transfer ceased at Re between 200 - 700, with fully turbulent convective heat transfer at Re = 400 – 1500. Peng and coworkers note that the Re corresponding to the onset of the transition regime and fully turbulent heat transfer decreases with decreasing D_h.

Pfahler *et al*. (1991) investigated friction factors and viscosities for polar and non-polar liquids and single-phase gases in 0.5-50 μm microchannels. The authors the observed the polar liquid (isopropanal) friction factor agreed with incompressible theory for the larger channels studied. However, the friction factor was lower than predicted for the polar liquid in the smaller channels, and for the non-polar liquid (silicon oil) in all cases. In all single-phase gas flows (He and Ni), the friction factor was consistently smaller than that predicted by incompressible theory. Webb and Zhang (1997) determined the friction factor data for turbulent single-phase liquid (R-134a) in circular (D = 0.96 mm) and rectangular (D_h = 1.31 mm) microchannels were in good agreement with the Blasius relation. Wang and Zhang also determined the heat transfer coefficient was well predicted by standard single-phase correlations (Petukhov and Dittus-Boelter). These results contrast the results reported by Wang and Peng (1994), who determined Dittus-Boelter held with modification of constants in turbulent regime for smaller channels.

Mehendale *et al*. (2000) note specific conclusions reached by the various authors may not be applicable to general trends in microchannels due to possible experimental errors or data interpretation methodology. Additionally, several studies (Wu and Little, 1993 and 1994; Pfahler *et al*., 1991; Choi *et al.*, 1991) pertain to microchannels with much smaller D_h than would be used in a compact heat exchanger. However, the general trend in the literature suggests fully developed turbulent flow and heat transfer occurs at lower Re than for macro-sized channels, and that decreasing the channel hydraulic diameter strongly decreases the transition Re number. Additionally, with the exception of Wu and Little (1994), friction factors are lower than predicted by the Blasius correlation, and decrease with smaller D_h (although that trend may manifest at D_h much smaller than those used in a compact heat exchanger). Finally, Peng and Peterson (1995) conclude that the shape of the microchannel plays a negligible role in heat transfer and flow friction.

1.2.2 Two- Phase Studies - Characteristics of Boiling in Microchannels

Two-phase heat transfer has several advantages over single-phase heat transfer. By relying on latent heat exchange, the two-phase coolant maintains a constant bulk temperature equal to the saturation temperature at the coolant pressure. Additionally, very high heat fluxes can be achieved for a constant flow rate while maintaining a relatively constant wall surface temperature. Comparable heat transfer with single-phase coolants requires either a decrease in the channel D_h or an increase in the flow rate, which both include an undesirably large increase in pressure drop. A CO_2-based heat exchanger would capitalize on the advantages of two-phase heat transfer in the heat-absorbing portion of the refrigeration cycle.

Studies investigating two-phase heat transfer phenomena in microchannels provide comparisons between the observed heat transfer coefficients and those predicted by standard correlations. In all cases reviewed, heat transfer enhancement was observed in microchannels, and correlations for standard channels underpredicted microchannel heat transfer experimental results. This trend has prompted studies into microchannel boiling phenomena characteristics; specifically, whether convection boiling dominates (as in macroscale channels), or whether nucleate boiling is the dominating heat transfer mechanism.

As described by Carey (1992), the onset of nucleate boiling represents the initial transition from a subcooled liquid to a two-phase flow. The onset of nucleate boiling occurs when vapor embryos form along wall

nucleation sites. In the fully developed nucleate boiling regime, nucleate boiling dominates the heat transfer process. Heat transfer is independent of mass flow rate and quality, dependent on heat flux, and sensitive to the coolant saturation pressure. As the vapor quality increases, however, a vapor core develops in the center of the flow and evaporation from the liquid-vapor interface results in two-phase forced convection boiling. In this region, the heat transfer coefficient is independent of heat flux and dependent on mass flow rate and quality, and heat transfer increases with increasing mass flow rate and quality. Eventually the liquid film evaporates, resulting in liquid droplets entrained in the vapor core which do not wet the channel walls. This condition, known as dryout, results in heat transfer from the channel well to vapor only, and there is a significant reduction in the heat transfer coefficient in this regime (accompanied by an increase in wall superheat). At higher heat fluxes, nucleate boiling goes directly into film boiling (DNB). Regardless of mechanism, the drop in the heat transfer coefficient corresponds to the critical heat flux.

Figure 1.2 shows a boiling map indicating the transition regimes encountered during the boiling process at a constant heat flux. The regimes encountered, and the vapor quality at which they are encountered, depend on the magnitude of the heat flux. However, this map was developed from large-diameter channel data, and neither Carey (1992) nor Collier and Thome (1996) describe the dependence of channel diameter on the boiling mechanism. The current literature suggests that Figure 1.2 may not be applicable to microchannel geometries, as described in the following sections.

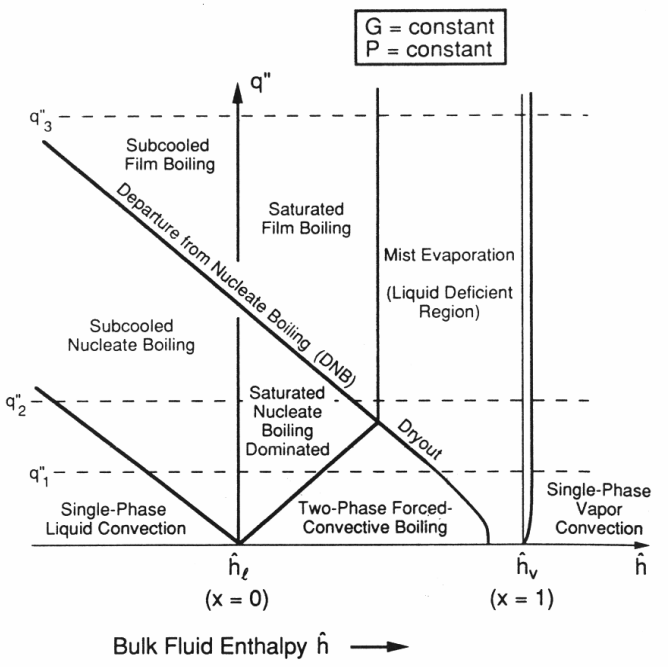

Figure 1.2 Boiling Regimes For A Constant Wall Heat Flux Condition (Carey, 1992)

Studies performed with R-12 and R-134a in circular channels (D=2.46 mm) by Tran *et al.* (1996) and rectangular microchannels (D_h=2.46 mm) by Tran *et al.* (1993) suggest that for all but very low wall superheats heat transfer was dependent on heat flux rather than the mass flow rate. By comparing microchannel heat transfer data to

several standard correlations which exhibit distinct transitions between the nucleation and convection-dominated boiling regions (Kandlikar, 1991; Jung and Radermacher, 1991; Liu and Winterton, 1990), Tran and coworkers suggest that nucleation boiling dominates over convective boiling in microchannels with vapor qualities up to 80%. This result differs from boiling patterns in larger channels, where convective boiling dominates over nucleation boiling at qualities > 20%. Tran and coworkers observed significant heat transfer enhancement in the small channels at a given wall superheat, and that standard correlations significantly underpredicted microchannel heat transfer for vapor qualities of 30%, 50%, and 80%. In the region of very low wall superheat (<2.75°C), Tran and coworkers determined that heat transfer was dependent on mass flow rate rather than heat flux, and that convective-dominated boiling dominated the heat-transfer process. They conclude that the domination of the nucleate-boiling region of the large range of vapor qualities contributed to the enhanced heat transfer in microchannels over large channels. Finally, very little difference was observed in the heat transfer coefficient between circular and rectangular channels with the same hydraulic diameter.

Peng and Wang (1993) performed studies of boiling liquid (water) in rectangular microchannels and similarly observed enhanced heat transfer over large channels. The measured heat transfer coefficients were independent of mass flow rate and quality, and were dependent on heat flux, which suggests nucleate boiling was the dominant heat transfer process. Peng and Wang suggest that nucleate boiling intensified in a microchannel, leading to smaller wall surface superheat than in large channels with the same wall heat flux.

Ravigururajan *et al.* (1996) studied heat flux and boiling characteristics of R-124 in rectangular microchannels (D_h = 0.475 mm), and observed that the heat transfer coefficient reached a maximum for a wall superheat less than 5°C (~24,000 W/m^2-C), then decreased significantly between the maximum and a wall superheat of 10°C. The heat transfer coefficient continued to decrease steadily for wall superheats up to 80°C, indicating the heat transfer coefficient decreases as wall superheat increases with a maximum at very low superheats. This trend was noticed for all mass flow rates; however, there was no correlation between the heat transfer coefficient and the mass flow rate. Ravigururajan and coworkers note that the heat transfer coefficient for a wall superheat of 10°C was approximately 300% higher than predicted by Chen's (1966) correlation for two-phase flow in a large channel, and that the heat transfer coefficient decreased significantly with small increases in fluid pressure. The heat transfer coefficient dependence on wall superheat (and related heat flux) and fluid pressure is consistent with nucleate boiling.

In their 1996 study, Ravigururajan *et al.* also observed that the heat transfer coefficient decreased by approximately 27% as the vapor quality increased from 1% to 65%. This decreasing trend was noticed at all flow rates, although the heat flux increased as the flow rate increased at any vapor quality. Ravigururajan and coworkers note that this trend is different than in large tubes, where the heat transfer coefficient increases in the nucleate boiling region ($x < 0.3$) before decreasing in the film boiling regime. These results suggest nucleation boiling is not the dominant heat transfer mechanism. One mechanism suggested for this trend is the choking of the channel width by bubbles released from the channel wall, although the authors caution that this conclusion cannot be confirmed by this study. Finally, a dramatic pressure drop increase was observed to accompany both an increase in wall superheat

(corresponding to a heat transfer coefficient decrease) and increase in heat flux, with both trends more pronounced at higher flow rates.

Ravigururajan (1998) investigated the effects of subcooled and saturated flow boiling experiments in a 54-channel diamond-shaped microchannel heat exchanger (D_h=425 μm) using R-124. The results are similar to the 1996 study. High heat fluxes were achieved with small wall superheat in subcooled boiling, and the effects of quality, pressure drop, and flow rate on the heat transfer coefficient and the heat flux were the same as noted in the 1996 study. Ravigururajan notes that pressure drop decreased marginally when the heat flux was reduced, and increased with an increasing vapor quality.

The current literature suggests that heat transfer is enhanced in microchannels, and that correlations for larger-diameter channels (>5mm) cannot accurately predict microchannel heat transfer. Conclusions differ as to the boiling heat transfer mechanisms in small channels over the entire quality range. Results from heat exchanger tests suggest a nucleation-dominate mechanism, as supported by studies of boiling in small smooth channels (circular and rectangular; Wambsganss *et al.*, 1993, Tran *et al.*, 1993, Peng and Wang, 1993). However some studies show the exact opposite, suggesting convection boiling is the dominant heat transfer mechanism, and that nucleate boiling is unimportant (as referenced by Tran *et al.*, 1996). In their study Tran and coworkers seem to resolve this discrepancy, and several recent studies suggest nucleate boiling is dominant to very high vapor qualities when compared to large-channel boiling map. A thinning boundary layer and bubble-generating mechanism that differs between large-diameter channels and microchannels may be responsible for the increased nucleate-boiling region (Ravigururajan, 1998).

Kasza and Wambsganss (1994) note that a reduction in channel size may lower the critical wall superheat associated with the transition to fully developed nucleate boiling. The authors suggest that multiphase flow regimes are drastically different in small channels due to vapor bubble confinement and bubble interactions and provide a theoretical approach to bubble growth and bubble/bubble and bubble/channel interactions. Peng *et al.* (1998) propose a thermodynamic analysis of bubble growth in a microchannel. Both studies are semi-mechanistic in nature, and further studies are required to develop predictive correlations for geometrically confined small-channel flows.

1.2.3 Very Small Microchannels and Thermophysical Effects

Researchers investigating thermophysical effects in very small microchannels (0.5μm – 50μm) have determined interfacial effects can retard fluid flow, creating an apparent viscosity which can be much greater than the predicted viscosity based on macroscopic flow measurements (Peng et al., 1994; Wang and Peng, 1994; Mala *et al.*, 1997). However, the separation distance between the bounding parallel walls where these effects are significant is much smaller than the channels used in compact heat exchangers, and fluid viscosity variations due to this mechanism are negligible.

1.3 Supercritical Heat Transfer

1.3.1 CO_2 Thermodynamic Data and Property and Transport Effects in the Pseudocritical Region

Supercritical CO_2 undergoes sudden reductions in density, thermal conductivity, and viscosity with increasing temperature near the critical point. Thus, while supercritical CO_2 remains a single-phase fluid, the fluid

thermophysical properties undergo a transition from "liquid-like" values to "gas-like" values. This region is often referred to as the "pseudocritical" region in the literature. Additionally, by definition the specific heat approaches infinity at the critical point. The temperature at which the specific heat attains a maximum value at a constant supercritical pressure is defined as the pseudocritical temperature. Figure 1.3 shows examples of supercritical CO_2 property variations about the critical point.

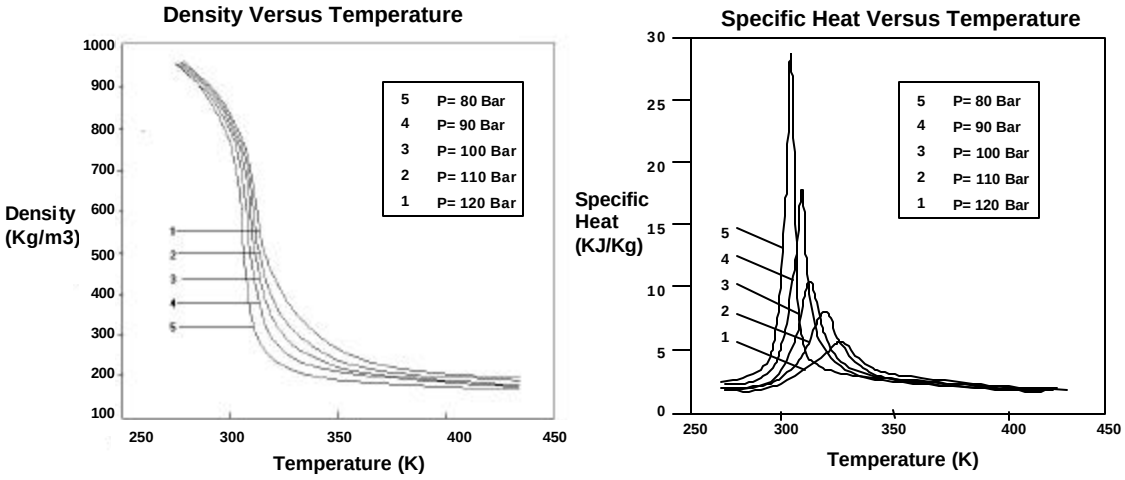

Figure 1.3 Examples of CO_2 Thermophysical Variations in the Pseudocritical Region (cf. Pitla *et al.*, 1998)

From a macroscopic standpoint, changes in density through the critical point are continuous. However, on a molecular scale the fluid is not homogeneous. Hall (1971) notes that the phenomenon of "critical opalescence" indicates the presence of a structure large enough to produce scattering of light, while x-ray diffraction patterns characteristic of liquids have been detected in supercritical fluids with a macroscopic density significantly less than the liquid. As temperature is increased and the fluid passes through the critical point, it appears the liquid structure transforms to liquid-like clusters in a gas matrix, which then reduce in size.

The dimensions of compact heat exchangers allow the supercritical CO_2 to be treated as a continuum. However, variations of physical properties with temperature in the pseudocritical region become extremely important when evaluating supercritical heat transfer. These variations, which in single-phase fluids may be treated as small perturbations of the constant-property idealization, may dominate the heat transfer process and invalidate theoretical models and empirical correlations. Both the compressibility and the specific heat become infinite at the critical point. Although a transcritical CO_2 cycle will not pass precisely through the critical point, the property variations are significant even at pressures considerably greater than the critical point (cf. Figure 1.3). Therefore, at pseudocritical temperatures the increase in compressibility implies small height or pressure variations may lead to significant density fluctuations, while the increase in specific heat implies a slow approach to thermal equilibrium.

Hall (1971) notes that the pseudocritical region may be thought of as that region in which boiling and convection merge. When the pressure is sufficiently subcritical or supercritical, the problem tends towards either a boiling problem or a constant-property convection problem, and existing correlations are adequate. The pseudocritical region is generally found in a range of pressures from the critical up to about 1.2 times the critical,

and the largest property variations occur when the critical temperature lies between the wall and bulk fluid temperatures.

At a given supercritical pressure, the heat transfer coefficient increases with increasing temperature below the pseudocritical temperature, reaching a maximum at the pseudocritical temperature. At temperatures greater than the pseudocritical temperature the heat transfer coefficient decreases with increasing temperature. This increasing-decreasing behavior about the pseudocritical temperature is asymptotic, with the greatest slope at the critical point. Likewise, the pseudocritical-temperature heat transfer coefficient reaches a maximum at the critical pressure and decreases asymptotically with increasing supercritical pressure.

CO_2 thermodynamic data were provided by Span and Wagner (1996), who developed an equation of state for CO_2 explicit in Helmholtz free energy. The Helmholtz energy was first nondimensionalized, then ideal gas behavior was separated from residual fluid behavior:

$$A(r,T)/(RT) = f(d,t) = f^0(d,t) + f^r(d,t) \tag{1.1}$$

where δ and τ are the reduced density and temperature, respectively. The Helmholtz equation is a fundamental equation, and all thermodynamic properties of a pure substance can be obtained by combining derivatives of Eq. (1.1). Span and Wagner estimate uncertainty of the equation in the range of 0.03% - 0.05% for density, 0.03% - 1% for the speed of sound, and 0.15% - 1.5% for the specific heat at a constant pressure.

The majority of supercritical heat transfer research has been devoted to determining the effects of the thermophysical property variations to predicted heat transfer, including both CO_2 and non-CO_2 supercritical fluids.

1.3.2 Pseudocritical and Supercritical Heat Transfer

1.3.2.1 Non-CO_2 Fluids

Several studies have used supercritical helium to investigate heat transfer phenomena in supercritical fluids. Kasao and Ito (1989) provide a literature survey of experimental findings for forced convective heat transfer in supercritical helium. The authors determined that an increased heat flux reduces the heat transfer coefficient in the pseudocritical region, where variations in thermophysical properties and shearing stress by buoyancy forces are the proposed mechanisms causing deviations from the predicted values. Deviations from the Dittus-Boelter correlation are greatest near the critical point; however, the Dittus-Boelter correlation accurately predicts supercritical helium heat transfer away from the pseudocritical region. Kasao and Ito note that proposed supercritical heat transfer correlations in the supercritical and pseudocritical regions are generally variations of the Dittus-Boelter equation that account for property variations. Mori and Ogata (1991) performed studies of natural-convection heat transfer of supercritical helium in laminar flow, and conclude that conventional single-phase subcritical correlations accurately predict the observed heat transfer. However, their channel cross-section (10mm x 0.4mm) is much larger than the calculated thermal boundary layer (several micons) and smaller channels may influence the heat transfer. Mori and Ogata note the appropriate temperature to use for evaluating fluid properties should be the film temperature (the average of the coolant and wall temperature) in the sub-critical region, and the pseudocritical temperature in the pseudocritical and supercritical region.

Yanovskii and Kamenetsdii (1991) performed a study on heat transfer coefficients in supercritical hydrocarbon fuels and determined significant turbulent heat transfer reduction in the pseudocritical region, when the

pseudocritical temperature falls between the mass-averaged streamwise temperature and the wall temperature ($t_f<t_p<t_w$). The authors determined the region of heat transfer reduction is governed by fluctuations of density and viscosity between the supercritical fluid near the wall and in the core flow. These property variations are accounted for in a proposed modified Dittus-Boelter correlation.

Bellinghausen and Renz (1990) performed studies on heat transfer to pseudocritical fluids in vertical tubes. The authors determined that fluid property variations in the pseudocritical region can either improve or reduce heat transfer, depending on the flow conditions. Improvements capitalize on the enhanced heat transport caused by the increased heat capacity of the fluid, while reductions occur due to reduction in turbulence (and corresponding heat transfer by convection) from buoyancy and gravitational effects. These results were observed for supercritical CO_2 in buoyancy-related experiments as noted below.

1.3.2.2 Supercritical CO_2 Heat Transfer

The majority of supercritical and pseudocritical heat transfer researchers have investigated the accuracy of established heat transfer correlations to various geometries. Table 1.1 summarizes several correlations used to predict supercritical CO_2 heat transfer. The base relationship was developed by Petukhov *et al.* (1961) for supercritical CO_2 without accounting for temperature variations in the thermophysical properties. Gnielinski (1976) modified the Petukhov correlation for constant thermophysical properties, extending the applicable range over $2300 < Re < 5 \times 10^6$ and $0.5 < Pr < 2000$, with a stated accuracy of 10%. The Petukhov-Gnielinski correlation has been used as the most accurate constant-property, in-tube heat transfer correlation (Olsen and Allen, 1998).

Krasnoshchekov and Protopopov (1971) accounted for variations in thermophysical properties by assuming a bulk-temperature Nusselt number and introducing correction factors for density and specific heat ratio. This relationship was developed for supercritical turbulent flow with a constant-heat-flux boundary condition. Krasnoshchekov and Protopopov used the original Petukhov correlation for the bulk-temperature Nusselt number, although it has been applied to the Petukhov-Gnielinski correlation (Olsen and Allen, 1998).

Krasnoshchekov *et al.* (1971) note that the Krasnoshchekov-Protopopov correlation multiplied by a correction function predicted the heat transfer to CO_2 from a heated stainless-steel tube (D=2.05 mm) with constant heat flux and wall temperatures up to 850°C to ± 15%. Likewise, Krasnoshchekov *et al.* (1969) showed a modified Krasnoshchekov-Protopopov correlation predicts supercritical CO_2 heat transfer under cooling conditions in a countercurrent heat exchanger (D = 2.22 mm).

Table 1.1 Supercritical Heat Transfer Correlations

Researchers	Correlation	Notes
Petukhov-Popov-Kirilov (1958) (Friction Factor from Filonenko)	$Nu_o = \frac{(f/8)\,Re\,Pr}{12.7\sqrt{f/8}(Pr^{2/3}-1)+1.07}$ Where $f = [0.79\ \ln(Re) - 1.64]^{-2}$	Constant Thermophysical Properties, friction factor for smooth tubes
Gnielinski modification of Petukhov correlation (1976) (Friction Factor from Karman-Nikuradse) (Friction Factor from Haaland)	$Nu_{PG} = \frac{f/2\,(Re-1000)\,Pr}{1+12.7\sqrt{f/2}(Pr^{2/3}-1)}\left[1+\left(\frac{D}{L}\right)^{2/3}\right]$ Where $\frac{1}{f} = 4.0\log_{10}(Re\cdot\sqrt{f}) - 0.4$ Or $f = \left\{-1.8\cdot\log\left[\frac{6.9}{Re}+\left(\frac{e/d}{3.7}\right)^{1.11}\right]\right\}^{-2}$ Where ε is the tube roughness	May not be applicable to regions where thermophysical properties are temperature-dependent Stated accuracy of 10% over $2300 < Re < 5 \times 10^6$ and $0.5 < Pr < 2000$ (Rohsenow *et al.*, 1985)
Krashnoschekov-Protopopov Modification of Gnielinski-Petukhov correlation (Generalized, 1971)	$Nu_{KP} = Nu_{PG}\left(\frac{r_w}{r_b}\right)^m\left(\frac{\bar{c}_p}{c_{p,b}}\right)^n$ Where $\bar{c}_p = \frac{i_w - i_b}{T_w - T_b}$ $\quad n = f(pc)\left(\frac{T_w}{T_b}\right)$ $m = 0.35 - 0.05p$ $\quad p = \frac{p}{p_c} = 1.02 - 5.25$	Used in horizontal heat transfer by Olsen and Allen (1998)
Dittus-Boelter	$Nu_{DB} = 0.023\,Re_b^{0.8}\,Pr_b^{0.4}$	Constant thermophysical properties. Works well in the supercritical range.
Griem (1995)	$Nu_G = 0.0169\ Re_b^{0.8356}\ Pr_b^{0.432}$	Applies to supercritical CO_2 in vertical smooth tube. May not apply in the pseudocritical region.
Jackson-Fewster (1975)	$Nu_{b,JF} = aRe_b^b\,Pr_b^c\left(\frac{r_w}{r_b}\right)^d\left(\frac{\bar{c}_p}{c_{p,b}}\right)^n$ Where a, b, c, and d are curve-fit constants and: $T_b < T_w = T_{pc}$ and $T_w > T_b = 1.2T_{pc}$, n=0.4 $T_b = T_{pc} < T_w$, $n = 0.4 + 0.2(T_w/T_{pc} - 1)$ $T_{pc} = T_b = 1.2T_{pc}$ and $T_b < T_w$, $n = 0.4 + 0.2(T_w/T_{pc} - 1)[1-5(T_b/T_{pc}-1)]$	Forced Convective heat transfer. Best for predicting pseudocritical heat transfer (Ghajar and Asadi)

Olsen and Allen (1998) conducted experiments using supercritical CO_2 in 10.9-mm ID channels for turbulent flow in horizontal tubes ($34{,}300 \leq Re \leq 154{,}600$). They employed convective boundary conditions (CO_2 and hot deionized water in a countercurrent heat exchanger) rather than a constant temperature or constant heat flux boundary condition to determine the heat transfer coefficient under applied conditions, although in these experiments supercritical CO_2 was heated rather than cooled. Olsen and Allen observed enhanced supercritical CO_2 heat transfer at low heat flux and degraded heat transfer at high heat flux, with the optimum heat flux at 30 kW/m^2. However, the constant-property Petukhov-Gnielinski correlation held within 6.6% for $Re > 72{,}000$ and a heat flux greater than 47 kW/m^2. Under conditions where buoyancy is negligible and the heat flux is constant, the Krashnoschekov-Protopopov correlation held to within ±3%. Olsen and Allen conclude the Krashnoschekov-Protopopov correlation can be used to predict heat transfer over their experimental range, but warn against extrapolating beyond the tested conditions.

Walisch and Trepp (1997) performed a study of supercritical CO_2 in tubes with mixed convection. The authors investigated heat transfer characteristics in the supercritical and pseudocritical states by heating CO_2 with a constant wall temperature, and conclude forced-convection turbulent correlations that neglect buoyancy effects accurately describe supercritical heat transfer above the pseudocritical region. Walisch and Trepp also conclude that within the pseudocritical region Dittus-Boelter type equations can be used if buoyancy-effects and fluctuations of ρ, c_p and λ are taken into account.

Ghajar and Asadi (1986) performed a review of several proposed heat transfer correlations for supercritical CO_2 and determined under forced convection, the correlation given by Jackson and Fewster (1975) was determined to be the most accurate (average absolute error of 6%, with 93% predicted with less than 15% derivation). For CO_2, Ghajar and Asadi suggest the following curve-fit constants: a = 0.025, b = 0.8, c = 0.417, and d= 0.32. However, Griem (1996) suggests that the high c_p at pseudocritical temperatures is not relevant in turbulent pipe flow, and proposes a procedure for determining a representative specific heat over a range of temperature or enthalpy values. Using this procedure Griem proposes a heat transfer correlation for turbulent flow in a smooth vertical tube at or near the critical point. Both the Jackson and Fewster and the Griem correlations are Dittus-Boelter type heat transfer correlations.

Kurganov and Kaptilnyi (1993) provide experimental data on the velocity and temperature fields of a heated turbulent supercritical-pressure CO_2 flow in a 22.7 mm diameter vertical tube with mixed convection. The authors conclude that buoyancy effects result in a rearrangement of velocity fields and shear stresses in upward flows. A near-wall fluid layer forms with reduced turbulence, hindering heat transfer and creating localized wall temperature peaks. These effects are not present in high Reynolds flows. Experimental results also showed buoyancy effects enhance turbulent heat transfer in downward flows. Adebiyi and Hall (1976) investigated the effects of buoyancy on supercritical CO_2 heat transfer in a horizontal pipe. Although the researchers determined there was enhanced heat transfer in the tube bottom due to increased turbulent heat transfer from buoyancy effects, the authors note these effects were still in development after 100 diameters of heated length in a 22.14 mm inner diameter pipe. Taking into account microchannel transport transitions occur at lower Re than in macro-sized tubes,

it is expected that buoyancy effects and pseudocritical property variations in a compact heat exchanger would have little-to-no effect on supercritical CO_2 heat transfer. This result was confirmed by Pettersen *et al.* (2000).

1.4 CO_2 Heat Transfer in Compact Heat Exchangers

Pettersen *et al.* (2000) performed a series of tests using 25 circular microchannels (D = 0.79 mm, L = 540 mm) soldered in manifolds at both ends. These tests were designed to investigate heat transfer and pressure drop phenomena inside transcritical CO_2-based compact heat exchangers, using optimum test designs based on previous studies on prototype CO_2 compact heat exchangers (Pettersen *et al.*, 1998). This study incorporated a refrigerant (CO_2)/coolant (water) dual loop and focused on supercritical gas cooling and subcritical evaporation tests. The results of the supercritical cooling and subcritical evaporation tests are as follows.

1.4.1 Supercritical Cooling

Pettersen and coworkers performed cooling tests with various heat fluxes and mass flow rates, and the observed measurements were compared to several supercritical heat transfer correlations including variations of Gnielinski and Dittus-Boelter. Results showed that both the heat transfer coefficient data and pressure drop data closely followed standard single-phase correlations, including a 4% mean deviation from the predicted heat transfer coefficient using Gnielinski with the Haarland friction factor and a 2% mean deviation from the predicted pressure drop using either the Colebrook & White or Swamee models.

Pettersen and coworkers (2000) tested the effects of heat flux, mass flow rate, and pressure on the heat transfer coefficient for supercritical cooling. The authors note a very minor heat flux influence on the heat transfer coefficient at a given temperature and supercritical pressure, with a 1.4% average increase in the heat transfer coefficient for increasing heat flux (10 – 20 kW/m^2) between 10-80°C at a constant supercritical pressure. However, a significant rise in the heat transfer coefficient was observed for an increasing mass flow rate at a given supercritical temperature and heat flux (42% increase from 600-900 $kg/m^2 \cdot s$ and 82% increase from 600-1200 $kg/m^2 \cdot s$). Finally, the heat transfer coefficient decreased approximately 52% at the pseudocritical temperature for increasing pressure greater than the critical pressure (21 $kW/m^2 \cdot K$ at 81 bar to 10 $kW/m^2 \cdot K$ at 101 bar). As expected, this drop is asymptotic and becomes negligible below 25 °C and above 80°C. All observed heat transfer coefficients were accurately predicted using Gnielinski (with minor deviations at high temperatures).

1.4.2 Subcritical Evaporation

During this study, Pettersen *et al.* (2000) investigated the influence of mass flow rate, evaporation temperature, and heat flux on the local heat transfer coefficient at different vapor qualities. Pettersen and coworkers note that a specific calculation model for evaporating CO_2 could not be found in the available literature. They compared their results to six available correlations for large-diameter tubes and found considerable discrepancies ($\sigma_{mean} \geq 55\%$ for six different models).

In all tests, the heat transfer coefficient increased with increasing saturation temperature for vapor qualities less than $x < 0.55$. At these qualities, the heat transfer coefficient was 13, 15, and 22 $kW/m^2 \cdot K$ at 0, 10, and 20°C, respectively. However, the heat transfer coefficient dropped lower than 5.5 $kW/m^2 \cdot K$ at qualities greater than 55% above a critical mass flow rate (~300 $kg/m^2 \cdot sec$). Pettersen and coworkers conjecture that dryout was responsible for the heat transfer coefficient decrease. Several tests were run to determine the effect of mass flow rate, heat flux,

and evaporation temperature on the heat transfer coefficient, and the results were compared to a calculation model which incorporated dryout. They conclude dryout is the most likely cause for the drop in heat transfer at high vapor qualities, but note that effects such as flow maldistribution could not be ruled out.

1.5 Conclusions and Project Goals

When considering heat transfer in the transcritical CO_2 cycle, the regions of interest are supercritical cooling and two-phase heat absorption. Although considerable study has been given to property variations and transport effects in the pseudocritical region, these effects are greatest in large-diameter channels at low Re, and are minimized in fully turbulent flow in microchannels. As confirmed by Pettersen *et al.* (2000), single-phase correlations are adequate for predicting heat transfer in the supercritical region.

The effects of microchannel geometry on two-phase heat absorption are not clearly understood. Certainly flow patterns and boiling regimes may differ in microchannels from those in larger channels. Transition to turbulence seems to occur at much lower Re than predicted by standard correlations, and heat transfer is enhanced. Several studies suggest nucleate boiling dominates at all but very low wall superheats, although this theory has not been confirmed. Of special interest is the increase in the heat transfer coefficient observed by Pettersen *et al.* (2000), which they interpreted as dryout. Dryout occurs at significantly higher qualities in large tubes; dryout at the relatively low quality of 55% could have considerable impact on heat exchanger design and performance. The goal of this project is to gain additional insight into flow regimes in subcritical and supercritical CO_2, and to directly observe the temperature increase associated with the decrease in the heat transfer coefficient reported by Pettersen *et al.* (2000).

This project, designated ACRC Project 101, was divided into two phases. The first phase was the design and development of the experimental setup, including a microchannel test section where flow visualization and non-intrusive temperature measurements of supercritical and subcritical CO_2 were conducted. The experimental setup also included a CO_2 delivery system, which allowed control of the CO_2 thermodynamic state properties and fluid flow parameters at the microchannel inlet. A non-intrusive thermometer and associated optics system were incorporated to record a temperature distribution along the channel without disturbing the flow. A throttling setup was inserted into the flow of subcooled liquid to create an isenthalpic pressure drop, allowing calculation of the post-throttle vapor quality. Finally, standard thermocouples and pressure transducers were incorporated into the test section to record additional wall and fluid data, and a data acquisition system was incorporated into test loop to automatically record transducer data. The second phase of Project 101 involved performing a series of tests to ensure control of the thermodynamic state of the CO_2, observing microchannel flow patterns measuring microchannel pressure drop, and confirming the decrease in the heat transfer coefficient.

Chapter 2: Experimental Apparatus

2.1 System Overview Test Loop and CO_2 Delivery System

A once-through, open-loop, CO_2 delivery system was designed to allow control of the CO_2 thermodynamic state entering the test section inlet. The test loop is shown in Figure 2.1. The CO_2 source was a 9.1 kg liquid-CO_2 cylinder with a central riser tube that allowed liquid to be siphoned from the cylinder bottom. Electric heating blankets were used to increase the CO_2 cylinder temperature and pressure to a desired value. Once a target pressure was research, the regulator was opened and the CO_2 flowed down a chilled inlet section, which ensured subcooled liquid entered the test section inlet. Mass flow rates were calculated from the decrease in source-cylinder mass over time. A throttle valve in the exhaust line was used to adjust the mass flow rate. Transducer data allowed monitoring of flow conditions, and were imputed into a PC-based Data Acquisition System (DAS). Specific aspects of the test loop are as follows.

2.1.1 Control of CO_2 Inlet Pressure and Temperature

A pressure relief valve, bleed valve, temperature alarm, and pressure transducer were placed in-line before the pressure regulator. The in-line relief valve (designed to begin opening at 10.32 MPa) and a built-in cylinder relief valve (designed to open at 24.07 MPa) ensured emergency removal of over-pressurized CO_2 far below the cylinder burst pressure of 41.27 MPa. The bleed valve allowed removal of the in-line pressure between the cylinder outlet and the closed regulator valve. A temperature alarm served as both an independent temperature measurement of the CO_2 exiting the cylinder and an alarm if the CO_2 fluid temperature exceeded the set alarm temperature. The pressure transducer allowed pressure measurements of the source cylinder. The pressure regulator could accommodate liquid and vapor CO_2 at up to 27.51 MPa at both the regulator inlet and outlet.

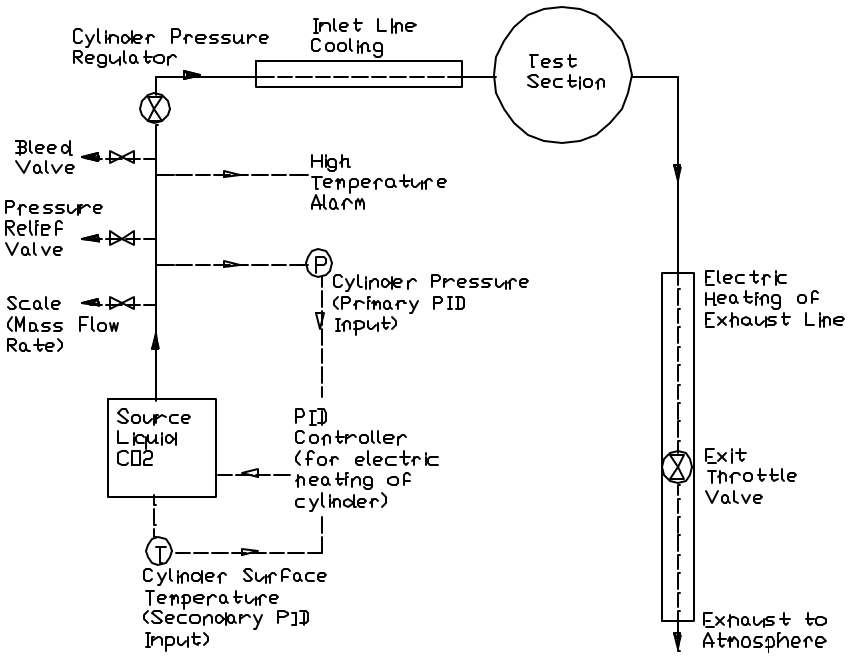

Figure 2.1 CO_2 Open Loop Delivery System

The first step in running the CO_2 experiment was to obtain the desired pressure within the source cylinder. Two 15.5 kW/m^2 heating blankets were clamped to the cylinder, and insulated with fiberglass. The tank valve was fully opened with the pressure regulator fully closed. The heating blankets increased the source cylinder internal pressure by raising the CO_2 temperature (and corresponding pressure) to the desired level. A control box was used to regulate and monitor the cylinder conditions with a PID (Proportional Integral Differential) feedback loop, which provided power to the heating blankets. The PID controller fed power to the blankets when two independent circuits were closed. These circuits were controlled by transducer voltage inputs. The primary input was from the in-line pressure transducer, which measured the static cylinder pressure (or the pressure of the liquid CO_2 exiting the cylinder once the regulator was opened). This circuit was closed if the voltage input (corresponding to the CO_2 pressure) was less than the set voltage (corresponding to the desired pressure). The second input was a thermocouple reading taken from the cylinder surface using a type-K thermocouple. This circuit was closed until the cylinder surface temperature exceeded the set temperature. Continuous power was supplied to the blankets unless either the primary or secondary inputs caused an open circuit. The secondary (temperature) circuit was a cutoff switch, and remained closed until the cylinder surface exceeded the set temperature, in which case the circuit remained open until the surface temperature fell below the set temperature. The primary input was opened and closed depending on the rate that the cylinder pressure approached the set pressure, which allowed the PID controller to maintain the target pressure within the cylinder even with the regulator open. A variable transformer allowed variable control of the blanket heat density (0 – 15.5 kW/m^2).

Once the cylinder target pressure was achieved, the pressure regulator was fully opened, and CO_2 flowed through a chilled inlet line to the test section inlet. PVC tubing connected to a 50% water - 50% ethylene glycol temperature bath was wrapped around the CO_2 inlet line. The temperature bath was cooled to -15°C, allowing the CO_2 to cool below the saturation temperature enter the test section as a subcooled liquid. The CO_2 inlet line and PVC tubing was placed in foam insulation to minimize heat transfer to the environment.

2.1.2 Control of the Mass Flow Rate

Mass flow rates were determined by using a 1-gram resolution scale. The cylinder, including the heating blankets, insulation, and tubing, was placed on the scale and the total weight measured. As CO_2 exited the cylinder, the reduction in mass was measured over time. A needle valve at the line exit was used to throttle the flow, controlling the mass flow rate. Heating rope was wrapped around the exit line downstream from the test section to allow the CO_2 to exit the test apparatus as a single-phase gas, which reduced the chances of blockage and constriction of the exit flow. All CO_2 was discharged to the atmosphere.

2.2 Test Section

The test section consisted of a rectangular microchannel milled into an aluminum substrate. Figure 2.2 shows the layout of the test section, while Figure 2.3 shows the dimensions and configuration. Aluminum was chosen as the substrate material to model conditions within a compact heat exchanger. The section consisted of a lower frame, including the microchannel, piping, and instrumentation; a glass window that allowed for flow visualization and non-intrusive temperature measurements; and an upper frame, which clamped down over the window onto the lower frame and provided a pressure seal. The 0.794-mm x 0.397-mm x 50.8-mm microchannel

had 1.59-mm diameter inlet and outlet ports bored at right angles into the substrate, allowing an o-ring groove to be milled around both ports and encircle the channel.

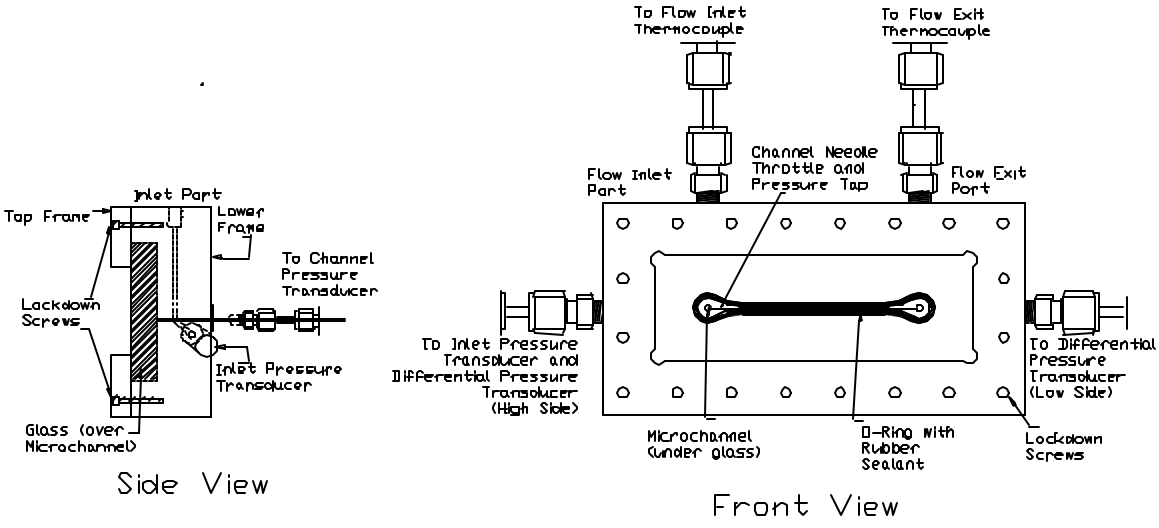

Figure 2.2 Microchannel Test Section

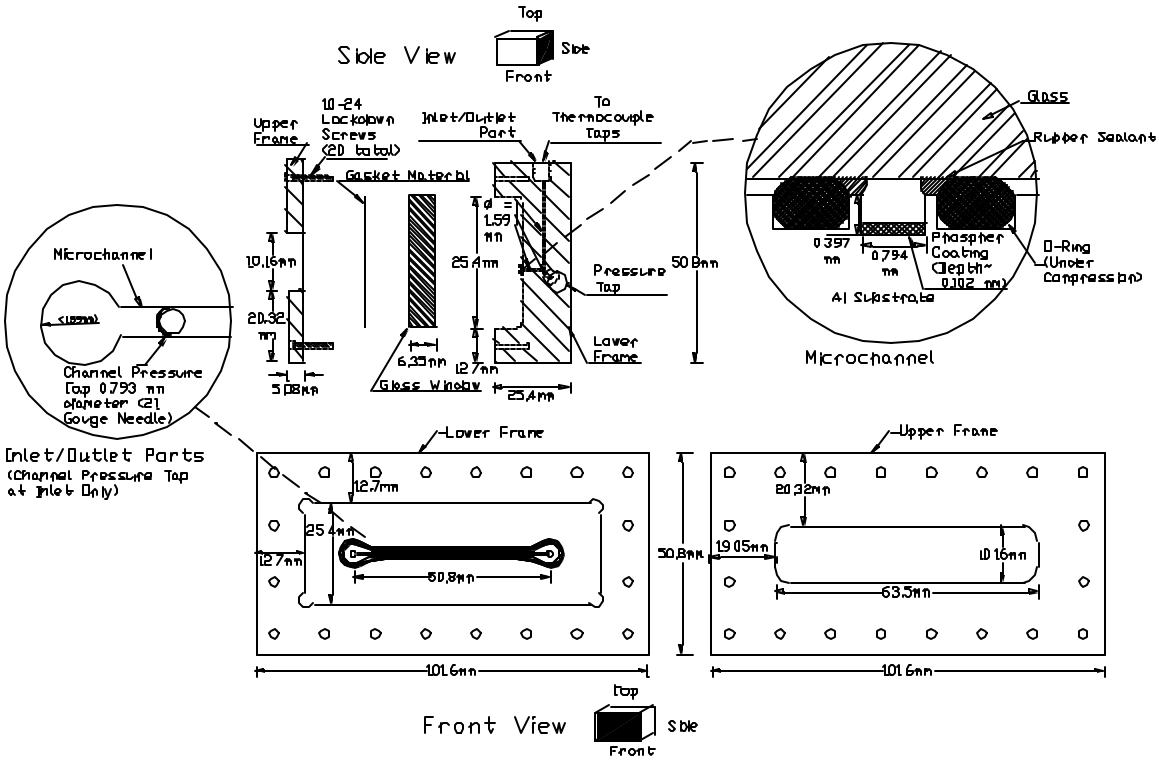

Figure 2.3 Test Section Dimensions

The aluminum substrate provided three of the four microchannel walls. The fourth wall was a 6.35-mm rectangular glass window that cradled inside the lower frame. The rectangular upper frame bolted to the lower

frame with 20 lockdown screws, compressing the glass onto the o-ring and providing the pressure seal. The widow was protected from the upper frame by gasket material. The upper frame provided a 10.16-mm x 63.5-mm viewing area of the entire microchannel.

CO_2 entered the test section at the top, 6.35-mm behind the microchannel through 3.18-mm diameter piping. All flow pipes within the test section were 1.59-mm diameter bored tubes. CO_2 entering the test section traveled 25.4-mm down the substrate tube, then was directed towards the microchannel inlet. The CO_2 traveled the 6.35-mm to the microchannel inlet, then flowed within the 50.8-mm microchannel length across the test section front towards the outlet port. The outlet piping configuration was the same as the inlet configuration. A 50.8-mm x 50.8-mm square ultra-thin heating blanket (15.5 kW/m^2) was attached to the back of the lower frame to provide a constant heat flux to the CO_2 in the microchannel. Temperature and pressure transducers were set to measure inlet temperature and pressure, temperatures along the microchannel, pressure drop along the microchannel, pressure drop from the inlet to outlet, and wall temperatures immediately after the inlet and before the outlet. The entire test section was insulated to maximize heat transfer into the microchannel.

2.3 Instrumentation

2.3.1 Thermocouples

Figure 2.4 shows the layout of the test section instrumentation with respect to the fluid flow. Test section thermocouples were placed directly in the CO_2 flow at the inlet and outlet, and at four wall locations. All thermocouples are grounded, type-K thermocouples with stainless-steel sheaths. The inlet and outlet flow thermocouples were immersed directly in the flow using face-sealing connectors. Four 0.794-mm diameter block thermocouples, designated BL1-BL4 and positioned counterclockwise from the inlet top, were used to determine the block substrate (wall) temperature at the inlet and outlet. Access holes were drilled into the lower frame adjacent to the inlet and outlet ports along the microchannel (cf. Figure 2.5).

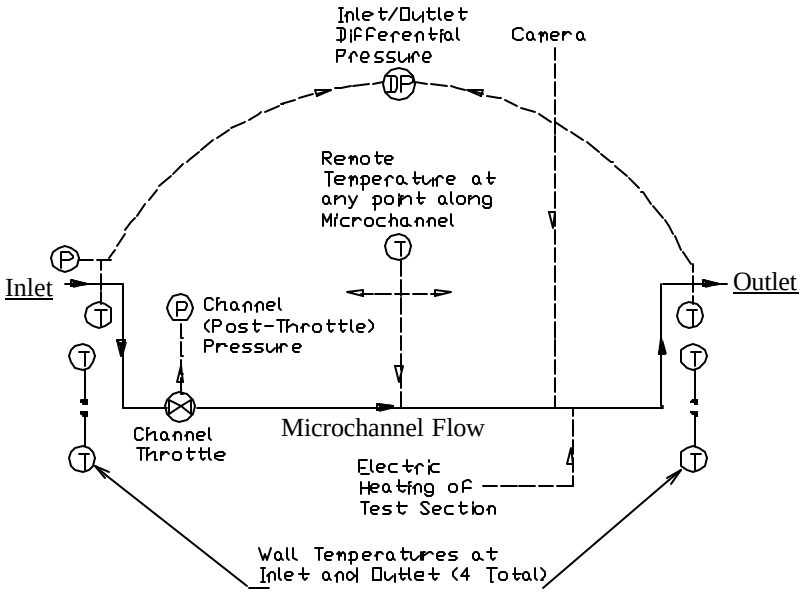

Figure 2.4 Test Section Transducer Layout

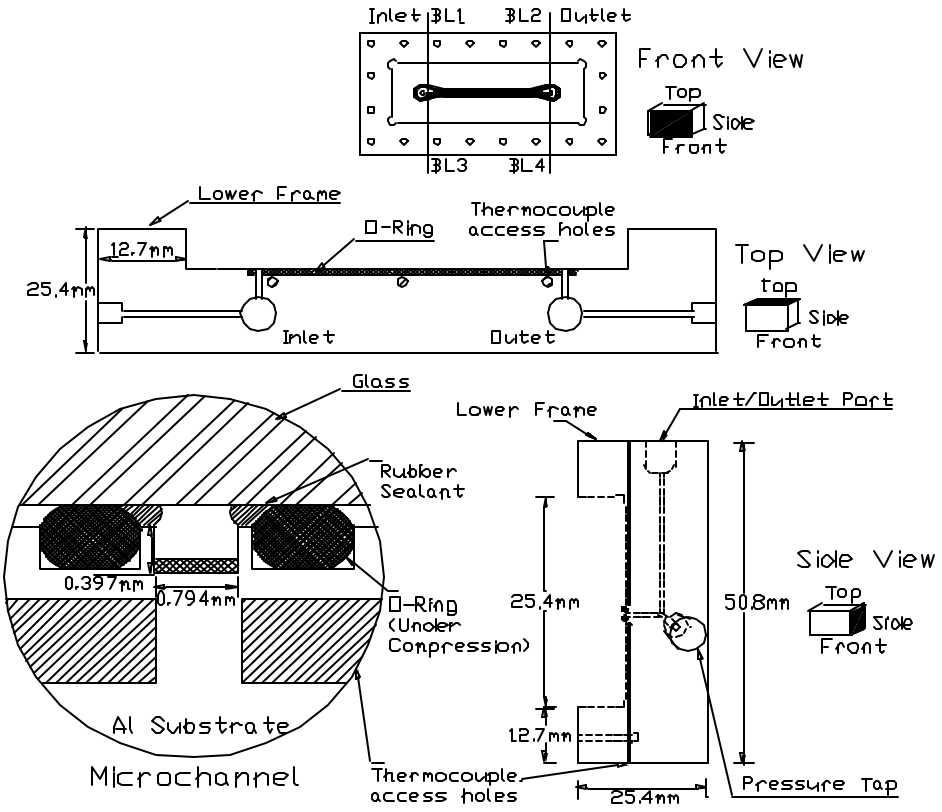

Figure 2.5 Block Thermocouple Access Holes

2.3.2 Pressure Transducers

One differential- and two absolute-pressure transducers were connected to the test section. One absolute- and the differential-transducer high side were connected to the inlet pressure tap, and the differential-pressure low side was connected to the outlet pressure tap. These allowed measurements of the inlet pressure and the pressure drop across the channel. Additionally, a second absolute-pressure transducer was connected to a channel pressure tap to measure the back-pressure after a throttling process (cf. Section 2.4). All absolute-pressure transducers were set to give 0.1-5.1 volts corresponding to 0-10.32 MPa. The differential pressure transducer was set to give 4-20 mA current corresponding to 0-172 kPa. A 249-Ω load resistor was used to convert the current to a voltage output and connected directly the DAS. All pressure transducers were powered by an external 24-V DC source.

2.3.3 Non-Invasive Temperature Measurements

In addition to the thermocouple temperature measurements, temperature measurements were also performed non-intrusively along the microchannel length using a fluoroptic thermometer. A thin layer of fluorescent phosphor coating the microchannel lower wall had had direct contact with both the channel wall and the CO_2. The thermometer generated an excitation pulse that traveled through a fiber optic cable to the phosphor lining the microchannel. The excitation pulse interacted with the phosphor, causing it to fluoresce. The fluorescent signal was conveyed back to the fluoroptic thermometer through the fiber optic cable. The thermometer measured the fluorescent decay time, which was temperature-dependent. By measuring the decay time, the thermometer

calculated the flow temperature at the measurement point. Once calibrated, this non-invasive method of measuring the phosphor temperature had an accuracy of approximately ± 0.5°C.

The thickness of the test section window was chosen to withstand the experimental pressures. However, signal attenuation by the window prevented direct measurements using the fiber optic cable. An optics system was incorporated into the system that focused the excitation pulse onto the microchannel and collected the fluorescent signal back onto the fiber optic cable. The microchannel test section was mounted on a high-precision X-Y stage that allowed control of spatial measurements.

2.3.3.1 Fluoroptic Thermometer

The Luxtron® 790 fluoroptic thermometer is a general purpose, multichannel remote thermometer. An internal xenon flash lamp generated a 420-nm excitation pulse that traveled through a fiber optic cable to the phosphor. The phosphor emitted a 650-nm exponentially decaying fluorescent signal that traveled back through the fiber optic cable to the thermometer. The thermometer measured the temperature-dependent fluorescent signal decay rate and calculated the phosphor temperature.

The fluorescent decay time is the only parameter that determines the phosphor temperature. The decay time does not depend on signal level or optical configuration, and the phosphor fluorescent signal is independent of excitation intensity. Therefore, temperature measurements were stable once the thermometer registered a minimum threshold fluorescent signal intensity. The phosphor was chemically insoluble and not reactive to CO_2; however, the material was susceptible to blowdown due to the shear force of the CO_2 as it traveled down through the test section. If the phosphor was reduced to the point where the minimum signal strength was not returned, the phosphor was recoated onto the microchannel.

The fluoroptic thermometer has an accuracy of ±0.1°C root mean square (RMS) at the point of calibration and ±0.5°C RMS within ±50°C of the calibration point. The thermometer and associated optics setup were calibrated in an icebath at 0°C, as all temperature measurements remained within the ±50°C window.

2.3.3.2 Optics and Mounting

A focusing lens was installed to counteract signal attenuation and dispersion through the test section window. The associated optics system transported the excitation signal from the thermometer, focused the signal onto the microchannel, and collected the fluorescent signal, focused it onto the fiber optic cable, and returned the signal to the thermometer (cf. Figure 2.6). A fiber optic coupler was secured to the fiber optic patch cable using an aspheric lens adapter. This adapter allowed the back lens focal length to be set and held on the fiber optic cable SMA connector. The fiber optic patch cable and coupler were set in a 25.4-mm lens tube and mounted to a thin 25.4-mm optics mount, which allowed control of the front lens focal point location to maximize the fluorescent signal strength. A vertical translation stage and rotation mount allowed vertical-height and axial-direction control of the signal.

The test section was mounted on a high-precision X-Y translational stage that was fixed along the length of the rail to minimize the distance between the fiber optic coupler and the test section window. Various measurements were taken along the microchannel length by translating the stage perpendicular to the optics rail. All stages were secured to an optics rail.

2.4 Vapor Quality Measurements

The CO_2 quality at the critical heat flux could be determined by forcing the CO_2 to change from a single-phase liquid to a two-phase fluid using a throttling process, then calculating the change of enthalpies and comparing to single-phase enthalpies to determine the quality.

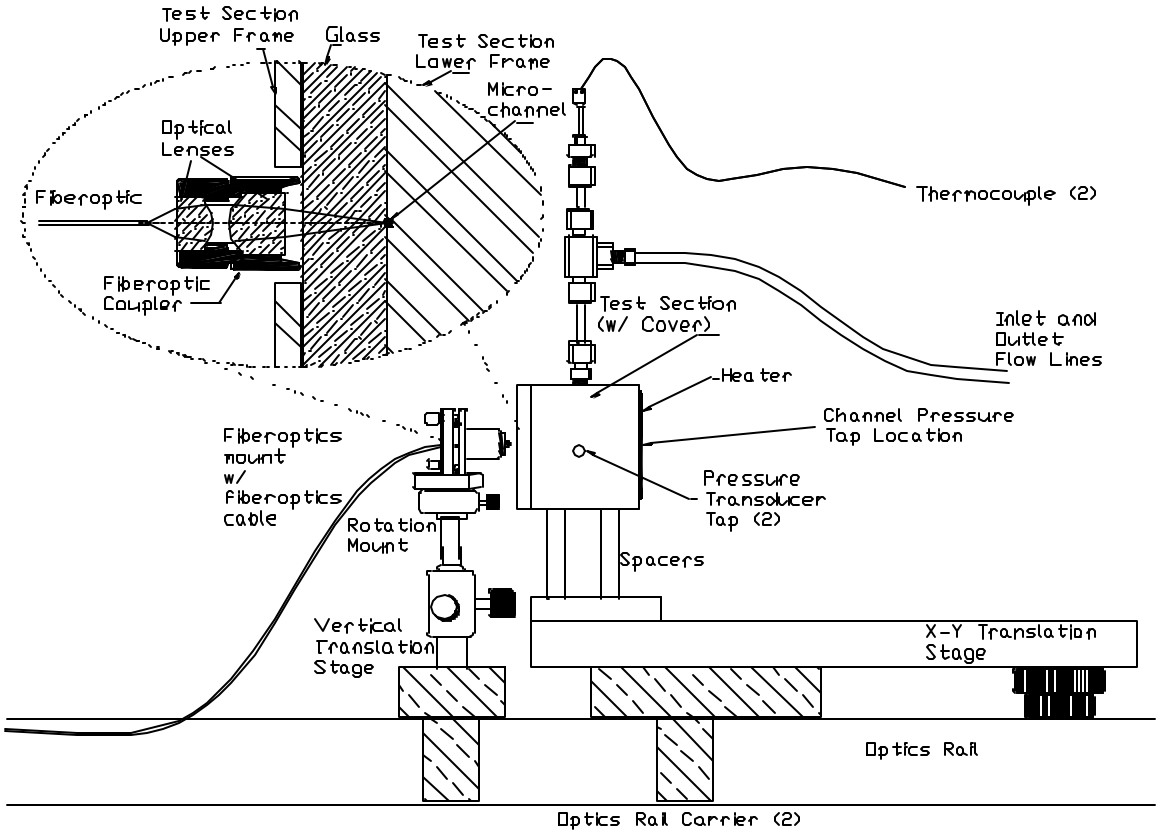

Figure 2.6 Setup of Test Section and Associated Optics

2.4.1 Throttling Process

After reaching the desired cylinder pressure, the pressure regulator was opened, and subcooled liquid entered the test section inlet. The inlet temperature and pressure was determined using the inlet transducers. The CO_2 then passed over a gate, creating an adiabatic throttling process (negligible heat transfer is assumed due to the limited area and rapidity of the process). A first law analysis is based on equation 2.1

$$\dot{Q}_{c.v.} + \dot{m}\left(i_i + \frac{\dot{V}_i^2}{2} + gZ_i \right) = \dot{W}_{c.v.} + \dot{m}\left(i_e + \frac{\dot{V}_e^2}{2} + gZ_e \right) \qquad (2.1)$$

There is no work or change in potential energy, and a negligible increase in kinetic energy for this throttling process. Therefore, the flow is modeled as a steady-state, steady-flow process in which heat transfer, work, and changes in kinetic and potential energy are all considered negligible. Therefore, Equation 2.1 reduces to a change in exit and entrance enthalpies:

$$i_i = i_e \tag{2.2}$$

The quality of the two-phase fluid can be determined using the enthalpies of the saturated liquid and saturated vapor:

$$i_e = i_i = i_f + x_e(i_g) \tag{2.3}$$

Knowing the inlet temperature and pressure will fix the saturated liquid enthalpy. Knowing the back-pressure of the two-phase fluid after the throttling process will fix the saturated liquid and vapor qualities, which in turn determines the fluid vapor quality.

2.4.2 Throttle Instrumentation

The throttling gate consisted of a 21-gauge (0.794-mm diameter) needle that could translate the full channel height (cf. Figure 2.7). The needle diameter equaled the channel width, and could be oriented to both restrict the CO_2 flow in a throttle process and provide the back-pressure measurement using the needle hollow. The head of the needle was flattened to maximize the microchannel cross-sectional area that was cut-off by the needle gate. The needle hollow was connected to an absolute-pressure transducer and signal inputs were recorded using the DAS.

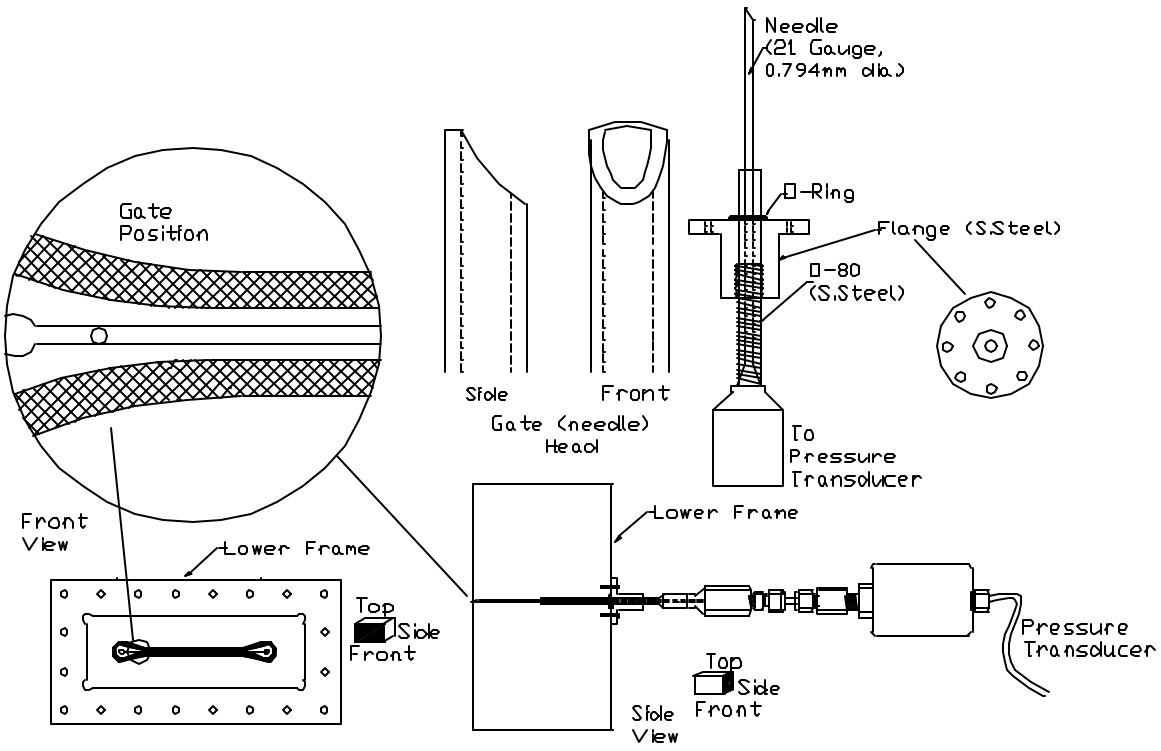

Figure 2.7 Throttle Gate

The throttle needle was placed in a screw/flange configuration to maintain the correct gate orientation while allowing control of the gate translational distance. The throttling needle was soldered inside a hollowed stainless-steel screw with 31.5 threads/cm (80 threads/inch, i.e., O-80), allowing the throttling gate to raise or lower with respect to the channel wall by rotating the needle/screw. However, in this configuration the correct gate orientation could only maintained by rotating the needle one full turn. With a channel height of 0.397-mm, the throttle could only be set in two correctly oriented gate positions within the channel (zero throttle and two intermediate throttle

heights). In order to increase the number of available gate heights, a flange with female threads was designed to mate with the O-80 male threads. This new setup allowed the flange to translate up-or-down the O-80 screw while keeping the needle in a fixed (desired) orientation. The flange was then bolted directly into the test section lower frame, which corresponded to a gate height translation in the microchannel. The flange could be bolted 1/8 of a turn, corresponding to a gate translation of 0.0397-mm in the microchannel and allowing for 9 available vertical positions within the channel.

Soldering and an o-ring at the flange/lower frame junction minimized CO_2 leakage to below detectable levels as it traveled to the pressure transducer. However, it was found that as the gate moved to the maximum height (corresponding to increasing the pressure drop across the throttle gate), the CO_2 deformed the channel o-ring and moved into the area between the compressed o-ring and the glass, bypassing the throttling process. To solve this problem, rubber sealant was used to fill this dead area. The sealant was applied with a hypodermic needle and jewelers screwdriver, and placed under compression for the 24-hour curing period. In order to prevent adhesion to the glass, Teflon tape was temporarily placed between the o-ring/rubber sealant and the glass. Once cured, the sealant deformed with the o-ring under compression, maintaining the channel integrity.

2.5 Data Acquisition System

A PC-based Data Acquisition System (DAS) was used to process transducer data collected from the microchannel test section. Thermocouple and pressure readings were hardwired into a National Instruments™ data acquisition board and routed directly to a PC. Data interpretation and manipulation was performed using the software package LabVIEW 5.0 by National Instruments™. The process is diagramed in Figure 2.8.

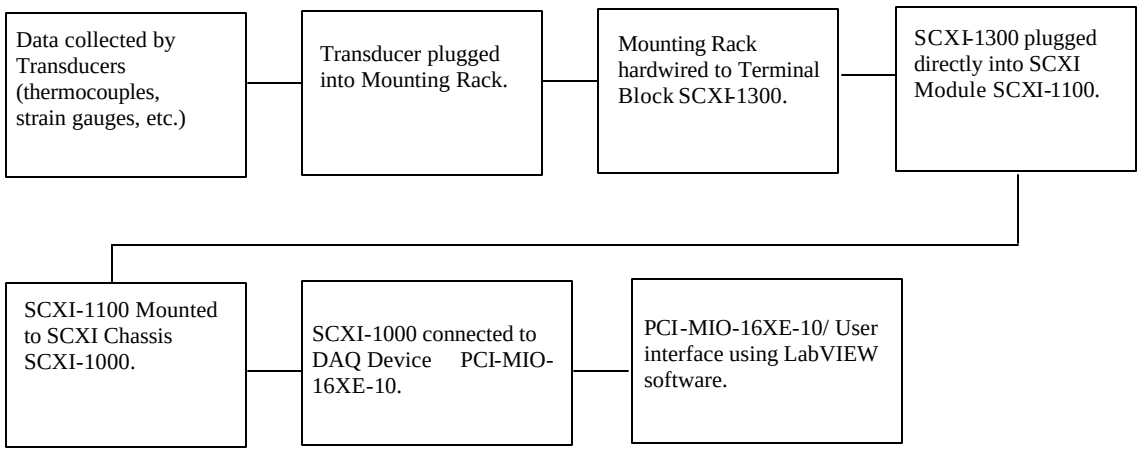

Figure 2.8 Data Transmission Flowchart

2.5.1 Hardware

The following hardware was used to receive and interpret the input data. All hardware was configured using NI-DAQ 6.1 Edition by National Instruments©

Hardware	Item Identification Number
Data Acquisition Device:	PCI-MIO-16XE-10
SCXI Chassis:	SCXI – 1000
SCXI Module:	SCXI – 1100
Terminal Block:	SCXI – 1300

2.5.2 Software

Virtual instruments (VIs) were created using LabVIEW for data acquisition and analysis. The VI written for data acquisition contained temperature readouts for the inlet and outlet thermocouples and the six block thermocouples. The cold junction on the SCXI-1100 was bypassed and a reference thermocouple was kept in an ice bath. All thermocouples were individually calibrated with respect to the ice bath (see Appendix B), and the block diagram written to incorporate the individual calibration curves. The VI also recorded the pressure measurements from the inlet, differential, and channel pressure transducers, again incorporating calibration curves for each transducer. All data were written to a file, which was then imported into an appropriate data-manipulation program. Specific acquisition parameters are included in Appendix C.

Chapter 3: Experimental Approach and Methods

3.1 Description of Critical Heat Flux

The critical heat flux condition phenomenologically corresponds to a sudden decrease of the heat transfer coefficient compared to the heat transfer coefficient for nucleate and forced-convective boiling. Owing to the de-wetting of the heated surface by the liquid phase, heat is transferred through the relatively poorly conducting gas rather than the highly conductive liquid, resulting in a corresponding increase in channel wall temperature.

In pool boiling, nucleate boiling increases until a vapor film prevents the interaction of liquid with the heated surface. This lack of heated-surface wetting is accompanied by a large temperature increase in which the dominant (relatively poor) heat transfer mechanisms are conduction and convection through the vapor film and, at higher temperatures, radiative heat transfer. This de-wetting of the heated surface and the corresponding drop in the heat transfer coefficient occurs at the critical heat flux. During in-tube boiling, the critical heat flux can occur while the fluid is a subcooled liquid, while nucleate boiling is the dominant two-phase heat transfer process, or after the formation of a vapor core around a liquid film. If the critical heat flux is exceeded while the fluid is a subcooled liquid or undergoing nucleate boiling, the critical condition is termed "departure from nucleate boiling" (DNB). In the region of higher enthalpies, where an annular vapor core forms around a liquid film that wets the channel walls, the critical condition is termed "dryout". This term associates the decrease in heat transfer with the evaporation of the liquid film. The CO_2 microchannel evaporation experiments were designed to probe two-phase heat transfer at higher enthalpies, in which the critical condition is achieved outside the nucleate boiling region.

The critical heat flux is a function of the mass flux, inlet subcooling, pressure, channel diameter, and heated length:

$$q''_{crit} = fn(G, (\Delta T_{sub})_i, P, D, z) \tag{3.1}$$

The critical heat flux estimate is constrained in two ways: The wall temperature must exceed the fluid saturation temperature, and the critical heat flux must occur before the fluid becomes a saturated vapor. These experiments were designed to operate within these two constraints, while minimizing the error in the critical heat flux parameters.

3.2 Predicted Behavior at the Critical Heat Flux

The ideal critical heat flux measurement would minimize heat flux, mass flux, and data acquisition errors while observing the predicted temperature increase associated with the heat transfer coefficient decrease under steady state conditions. This measurement was difficult to make, as the heated surface de-wetting is a dynamic phenomenon, and limitations in both the experimental apparatus and diagnostic instrumentation reduced the measurement accuracy. However, techniques were incorporated to determine the *maximum* possible heat flux associated with the critical heat flux at a particular mass flux. This allows a comparison between the predicted critical heat flux and an upper bound for the measured critical heat flux.

The decrease in the heat transfer coefficient at the critical heat flux has an attendant wall temperature increase that will be probed by using the fluoroptic thermometer. The temperature increase can be estimated by

performing an energy balance on a control volume enclosing the region where the critical heat flux occurs, cf.. Figure 3.1.

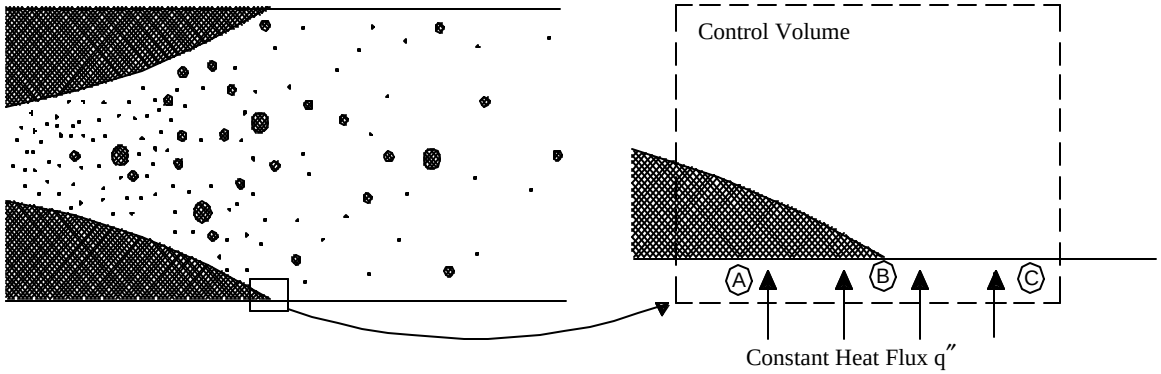

A. Wet Wall B. Point of De-wetting C. Dry Wall (vapor only)

Figure 3.1 Control Volume for Critical Heat Flux Phenomenon

Assuming a constant mass flow rate, wall heat flux, and fluid temperature during the phase change throughout the control volume, a relationship between the heat transfer coefficients before and after the critical heat flux can be developed:

$$q' = h_w \Delta T = h_d \Delta T = \text{constant} \tag{3.2}$$

or

$$q' = h_w (T_{s,w} - T_f) = h_d (T_{s,d} - T_g) \tag{3.3}$$

Solving for Ts,w and Ts,d and rearranging (noting Tf = Tg):

$$T_{s,w} = \frac{q''}{h_w} + T_f \tag{3.4}$$

$$T_{s,d} = \frac{h_w}{h_d}(T_{s,w} - T_f) + T_g \tag{3.5}$$

$$T_{s,d} = \frac{h_w}{h_d}\left(\frac{q''}{h_w} + T_f - T_f\right) + T_g = \frac{q'}{h_d} + T_g \tag{3.6}$$

The expected temperature difference, ($T_{s,d}$ - $T_{s,w}$) can now be determined:

$$T_{s,d} - T_{s,w} = \left[\left(\frac{q''}{h_d} + T_g\right) - \left(\frac{q''}{h_w} + T_f\right)\right] \tag{3.7}$$

or

$$\Delta T_s = q''\left(\frac{1}{h_d} - \frac{1}{h_w}\right) \tag{3.8}$$

As expected, the change in wall temperature before and after the de-wetting phenomenon is dependent on the magnitude of the critical heat flux and the heat transfer coefficient at the critical heat flux. The heat transfer coefficients observed by Pettersen *et al.* (2000) were used to estimate the change in wall temperature vs. the applied heat flux, cf. Figure 3.2.

The fluoroptic thermometer averages 8 samples taken at a frequency of 4 Hz for one temperature measurement (See Section 3.3.4). Therefore, to observe the predicted temperature increase the imaging spot must be maintained at a discrete axial location for at least 2 seconds. However, the de-wetting phenomenon is subject to spatio-temporal variations. De-wetting will occur sporadically and within a local region rather than at a discrete axial point, and constant drying/rewetting of the wall was expected to reduce the observed temperature increase. Additionally, the above analysis ignores the heat transfer to the liquid droplets entrained in the vapor core, and all enthalpy goes into sensible heat for superheating the vapor. Although thermodynamic behavior after the de-wetting phenomenon for low pressure and velocity is consistent with this assumption, this analysis gives an order-of-magnitude prediction of the critical heat flux temperature increase, or at best, an upper bound.

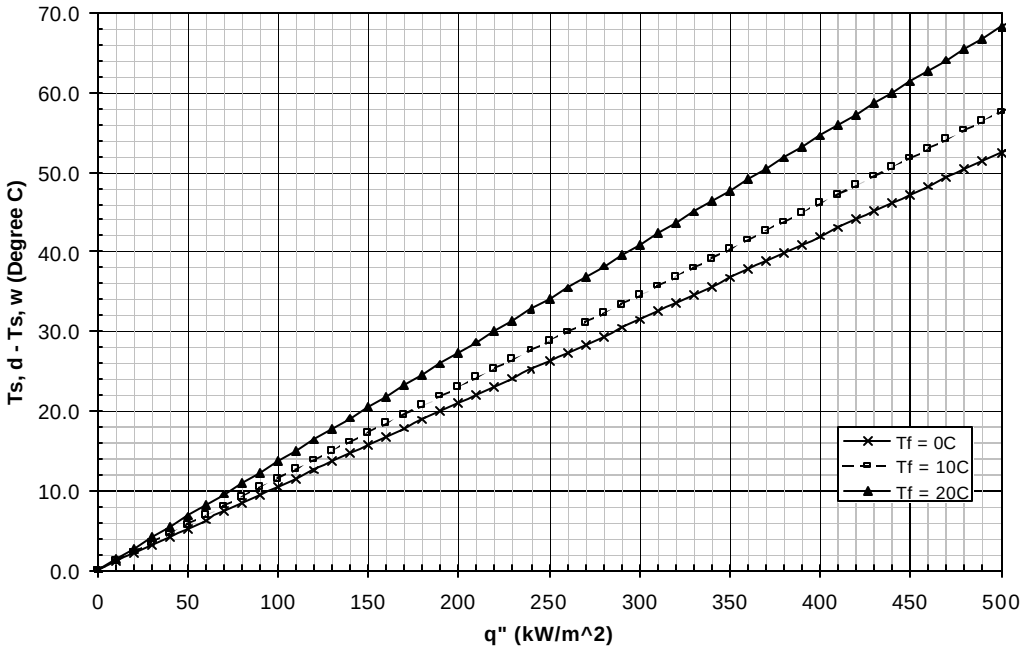

Figure 3.2 Change in Wall Surface Temperature as a Function of Constant Surface Flux

3.3 Experimental Methods

3.3.1 Control of the CO_2 Thermodynamic Properties

To determine the vapor quality at the critical heat flux, CO_2 had to enter the microchannel inlet as a subcooled liquid. The inlet flow thermocouple allowed measurement of the CO_2 bulk fluid temperature entering the test section; however, this temperature was not equal to the temperature at the microchannel inlet owing to the finite heat transfer coefficient and relatively low thermal diffusivity of CO_2. The temperature of the CO_2 rose significantly between the test section inlet and the microchannel inlet port. Therefore, the inlet flow thermocouple was used to

indicate the CO_2 thermodynamic state leading to the test section, but the fluoroptic thermometer was required to confirm the subcooled liquid state at the microchannel inlet.

Experimentally, subcooled liquid was observed at the channel inlet only when the cylinder pressure was greater than ~5.5 MPa. Below this pressure, the CO_2 always entered the test section as a two-phase fluid, regardless of the amount of inlet-line cooling. Above this pressure, the CO_2 could enter the test section as a subcooled liquid, with heat input from the test section leading to the microchannel inlet bringing the CO_2 into the two-phase region. To avoid this condition, the pressure regulator was opened with the exit throttle closed, allowing stagnant CO_2 to subcool in the inlet section prior to increasing the mass flow rate. In order to cool the test section area leading to the microchannel inlet, the exit throttle was nudged open slightly then quickly closed, allowing the subcooled liquid CO_2 to enter the test section and the microchannel inlet. This process was repeated until the fluoroptic thermometer confirmed that the CO_2 microchannel inlet was below the saturation temperature at the testing pressure.

Pressure readings were recorded using the inlet and channel pressure transducers. Preliminary tests using the throttling instrumentation showed that fluid velocities at the mass fluxes of interest were too low to cause an appreciable drop in pressure, equivalent to an increase in vapor quality. Therefore, during the channel heating experiments the throttling instrumentation was removed, although the channel pressure transducer was incorporated into the DAS. Preliminary tests also confirmed the pressure drop across the channel was negligible, and a single reference pressure was used for all tests.

3.3.2 Control of the Mass Flux

The mass flux was controlled by throttling the flow with a needle valve at the flow exit. In order to approximate conditions in compact heat exchangers, the mass flux was generally kept at or below 1000 kg/m^{2}sec, which required a very slight opening of the needle valve. Two conditions arose that hindered the attempt to maintain a constant mass flow rate. The large pressure difference and throttling process caused the needle valve to freeze over, restricting the flow. High temperature rope heaters were placed around the valve and line leading to the valve to maintain a superheated vapor throughout the throttling process. However, overheating could cause thermal expansion of the valve, again restricting the flow. A variable transformer was used to control the heat flux to the exit line, although this did not completely solve the problem. Therefore, scale weight measurements were recorded at approximate one-minute intervals, and tests were acceptable only if there was no greater than a 5% deviation from the mean flow rate over at least 3 minutes prior to the observation of the critical heat flux.

3.3.3 Control of the Heat Flux

A 15.5 kW/m^2 heating blanket was attached to the back of the test section, and the test section insulated to minimize heat transfer to the environment. The test section heater leads were attached to both a power cord leading to a variable transformer and a voltmeter which read the applied voltage. The voltmeter allowed the calculation of the total applied heat to the test section.

3.3.4 Effect of the Fluoroptic Thermometer and the Observed Temperature Increase

Two settings on the fluoroptic thermometer were chosen so as to maximize the temperature measurement accuracy at the highest possible measurement frequency: the number of samples-per-measurement and the measurement update time. The measurement update time was set to “continuous”, so that a new temperature

measurement began with each sample. The samples-per-measurement setting could be varied from 1 to 999, with lower settings for faster temperature measurements. The flashlamp produced excitation pulses at 4 Hz, allowing a maximum of 4 temperature measurements per second. At the lower settings, however, 2°C-3°C fluctuations on a constant-temperature surface indicated the temperature measurements were unacceptably inaccurate. A setting of 8 samples-per-measurement setting improved the temperature measurement stability (within 0.2°C of the mean) with a mean temperature within 0.5°C of the thermocouples under completely static conditions (no CO_2 flow). However, at an excitation frequency of 4 Hz, temperature measurements must remain stable for 2 seconds for accurate readings, which could not be maintained at the de-wetting axial location.

In order to surmount this difficulty, the 8 samples-per-minute were used with continuous updating. The critical heat flux condition produced a rapid fluctuation of temperatures ranging from the saturation temperature to a few degrees about the saturation temperature, which was above the instrument measurement error. To ensure that this was the unequivocal manifestation of de-wetting, steady temperature measurements were then recorded at both the microchannel inlet and exit ports. If the inlet temperature was below the saturation temperature and the exit temperature above the saturation temperature, the rapid temperature fluctuation was interpreted as the de-wetting condition at the critical heat flux.

3.3.5 Experimental Procedure

The test section and associated diagnostic sensors were set up before any tests were conducted. The fluorescent phosphor on the channel wall and the rubber sealant around the o-ring were given a 24-hour curing period prior to performing a series of tests. Additionally, the sealant over the phosphor was given an additional 8 hour cure time. Once the test section was ready, the window was secured over the channel and the wall thermocouples inserted into the test section. Insulation was placed around the section minimize heat transfer to the environment during the experiments, and electrical tape was placed over the top frame both to reduce glare while videotaping the flow and to assist in minimizing heat transfer out the top. The insulated test section was secured to the translation stage and the flow thermocouples, pressure transducers, and heat blanket voltmeter were reattached to the test section. The vertical height of the lens setup was readjusted and the fluoroptic thermometer signal tested to confirm the non-invasive temperature measurements were recorded. Finally, the CCD camera was remounted for video recording and observation of the flow. Pressure tests were performed to ensure there was no blowdown of the phosphor, the sealant around the o-ring remained intact, and there were no leaks from the various fittings.

The experiments began by allowing the inlet section chiller to cool down to -15°C. Once cooled, the source cylinder was fully opened with the regulator closed and the DAS started. The exit throttle was closed and the regulator opened to the testing pressure. Once the subcooled liquid was observed at the channel inlet, the exit throttle was opened, increasing the mass flow rate. Weight measurements were recorded approximately every minute, and the heat flux to the exit line adjusted to maintain a constant mass flow rate.

The fluoroptic thermometer measurements were the primary indication of the de-wetting event. Once a saturated liquid was confirmed at the inlet, the test section was positioned just before the channel outlet port, as this is the location of the maximum fluid enthalpy (and highest vapor quality). As the limiting conditions for the critical heat flux is a wall temperature greater than the CO_2 saturation temperature, the heat flux was initially set high until

the wall thermocouples approached the saturation temperature. The heat flux was then reduced until the wall thermocouples were at a steady state just under the saturation temperature, then the heat flux was steadily increased until exit wall thermocouples were above the saturation temperature. In this region, all temperature measurements remained stable with a gentle increase in the heat flux, indicating the applied heat flux increased the flow vapor quality prior to the de-wetting phenomenon. This condition continued until the fluoroptic thermometer displayed the rapid temperature fluctuations towards the channel outlet port. Several iterations were made until a flux was achieved that allowed steady (1-2 sec) fluoroptic temperature measurements to confirm the inlet temperature was less than the saturation temperature, the outlet temperature was greater than the saturation temperature, and the 2-3 degree temperature fluctuations which were interpreted as the de-wetting phenomenon. It was observed that this phenomenon did not remain in a static axial position but moved around in the channel.

3.3.6 Acceptance or Rejection of Experimental Results

Several factors contributed to the possible rejection of experimental data. Often a subcooled liquid could not be maintained at the microchannel inlet. Blowdown of the phosphor or tearing of the rubber sealant during testing conditions would invalidate an experimental run. Maintaining the de-wetting condition in the channel long enough to retake measurements at the channel inlet and exit was sometimes not possible, and fluctuations in the mass flow rate would invalidate an experimental run. Additionally, failure of sensitive diagnostic equipment would cause an experimental test to be aborted. After several experimental tests, the accepted data were reduced and presented in Section 4.

Chapter 4: Data Analysis and Results

4.1 Experimental Parameters

Figure 4.1 depicts a typical thermodynamic process involved in the microchannel experiments on a CO_2 temperature-enthalpy diagram.

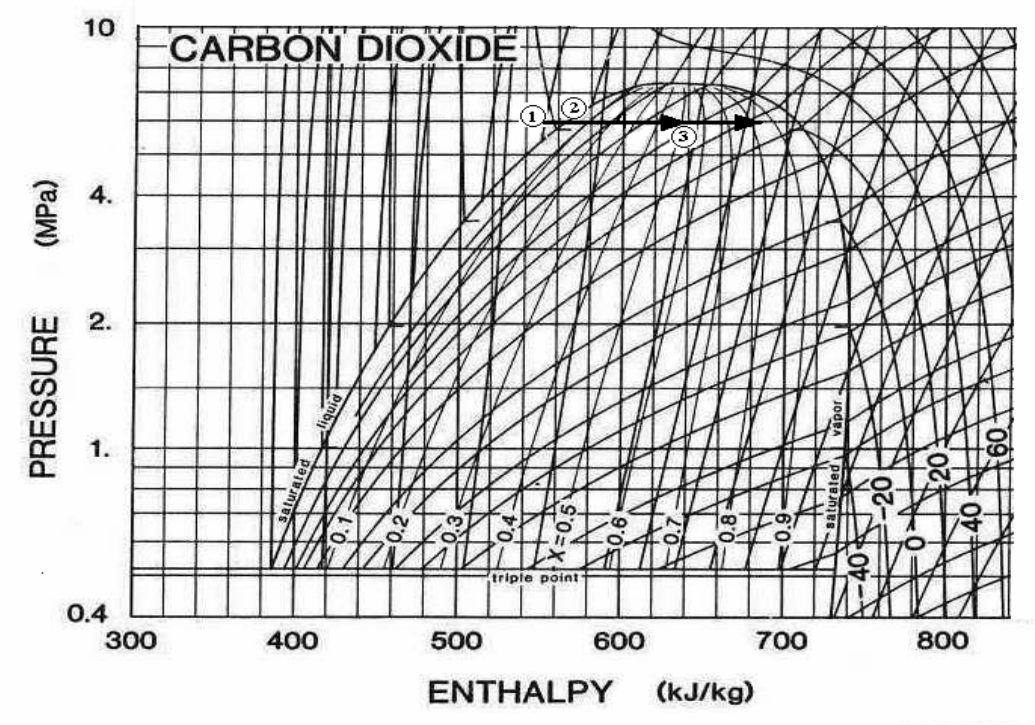

1 – Subcooled Liquid 2 – Saturated Fluid 3 – Critical Heat Flux

Figure 4.1 Thermodynamic State of CO_2 during an Experimental Run

At the mass fluxes tested, the small pressure drop along the channel (<0.08 MPa) allowed the estimation that the CO_2 remained at a constant pressure throughout the microchannel. The CO_2 enters the microchannel inlet as a subcooled liquid (State 1). The imposed heat flux corresponds to sensible heat input, raising the CO_2 temperature to the saturation temperature (State 2). After this, the heat input is assumed to be associated with latent heat. The CO_2 remained isothermal until the point of de-wetting (State 3), with the input enthalpy increasing the vapor quality.

The calculation of the flow quality at at the critical heat flux requires knowledge of the mass flux, the total heat input from the heater, and the inlet subcooling. The mass flux was calculated knowing the mass flow rate and the channel area:

$$G = \frac{\dot{m}}{A} \tag{4.1}$$

The total heat input from the test section heating blanket to the flow is estimated from the applied heating power and the heated channel area, and the total enthalpy input to the flow is calculated from the heating power and the mass flow rate:

$$q = \frac{V^2}{R} \cdot A_H \tag{4.2}$$

$$A_H = (2 \cdot height + width) \cdot length$$

$$\Delta i_T = \frac{q}{\dot{m}} \tag{4.3}$$

The use of these equations is subject to errors associated with measuring the applied voltage and mass flow rate, and heater resistance dependence on temperature. An uncertainty analysis is included in Appendix B.

To determine the quality at the critical heat flux, the sensible heat was subtracted from the total enthalpy. The CO_2 temperature and pressure at the microchannel inlet determined the entering enthalpy of the subcooled liquid, and the thermodynamic data from Span and Wagner (1996) were used to determine the total sensible heat input to the subcooled liquid:

$$\Delta i_{sens} = i_i - i_f \tag{4.4}$$

$$\Delta i_{lat} = \Delta i_T - \Delta i_{sens} \tag{4.5}$$

Most experiments conducted had typically 1°C - 2°C inlet subcooling, corresponding to approximately 3-7 kJ/kg sensible enthalpy. Finally, the quality at the critical heat flux is determined by comparing the input latent enthalpy to the total enthalpy of vaporization:

$$x = \frac{\Delta i_{lat}}{i_{fg}} \tag{4.6}$$

4.2 Assumptions

Before the critical heat flux, it is possible to have regions of superheated liquid, i.e., the imposed heat flux is converted to sensible heat rather than latent enthalpy at the saturation temperature. However, superheated liquid is a non-equilibrium state, and the bulk fluid remained at the saturation temperature. Sensible heat in the two-phase region is assumed negligible. This assumption is conservative, as the vapor quality at the critical heat flux is overestimated.

After the critical heat flux, enthalpy input continued to increase the vapor quality through evaporation of the liquid droplets entrained in the vapor core. The flow remained in the two-phase fluid region at the saturation temperature, which was confirmed by the outlet flow thermocouple measuring the bulk fluid temperature exiting the test section. However, at the wall, conduction and convection to the saturated vapor resulted in a superheated vapor. Neither the CO_2 vapor quality exiting the test section, nor the temperature of the superheated vapor immediately above the wall could be determined. Therefore, quantifying the enthalpy input after the critical heat flux was not possible. As a conservative assumption, the total heating power minus the sensible heat (used to raise the subcooled liquid to the saturation temperature) is assumed to be applied to the fluid prior to the critical heat flux. This assumption overestimates the vapor quality at the critical heat flux. Additionally, the heat loss to the environment is assumed to be negligible. Although the test section insulation minimized environmental heat loss, piping and diagnostic instrumentation served as conduits for heat loss. The combined effect of these assumptions gave an upper limit bounding the vapor quality at the critical heat flux.

4.3 Results

4.3.1 CO_2 Flow Quality at the Critical Heat Flux

Out of 59 experimental tests varying in length from 3 to 45 minutes, 12 instances of the critical heat flux were recorded which met the acceptable data criteria set in Section 3. Table 4.1 provides a summary of the test conditions, input enthalpy, and the observed quality at the critical heat flux, while Table 4.2 provides the pertinent thermodynamic data. Figure 4.2 shows the vapor quality at the critical heat flux versus mass flux. The DAS output and fluoroptic record sheets are included in Appendix A.

Table 4.1 Data for Flow Vapor Quality at the Critical Heat Flux

Test Date-Number	Mass Flux	Power	Latent Heat of Vaporization	Input Latent Enthalpy	Quality at the Critical Heat Flux
	kg/m^2-sec	W	kJ/kg	kJ/kg	
7/15-3	500.8	4.17	129.0	31.6	0.25
7/15-6	1166.6	10.20	135.0	37.6	0.28
7/15-7	343.2	4.21	135.0	46.4	0.34
7/16-4	362.4	6.79	120.0	81.3	0.68
7/16-7	525.0	6.74	140.5	57.1	0.41
7/17-1	481.2	4.43	144.1	35.9	0.25
7/19-1	523.8	6.88	144.1	54.5	0.38
7/19-2	333.3	5.07	144.1	66.4	0.46
7/21-1	293.6	5.85	141.5	82.8	0.59
7/21-2	2864.9	43.24	142.2	69.9	0.49
7/21-3	714.2	4.73	144.1	27.6	0.19
7/21-4	2380.8	30.47	147.6	58.9	0.40

Table 4.2 Applicable Thermodynamic Data

Test Date-Number	Pressure	P_r	Saturation Temperature	T_r	Subcooled Liquid Temp	Δi_T	Δi_{sens}	Δi_{lat}	i_{fg}
	MPa		°C		°C	kJ/kg	kJ/kg	kJ/kg	kJ/kg
7/15-3	6.25	0.85	24.0	0.78	22.2	39.6	8.0	31.6	129.0
7/15-6	6.2	0.84	23.5	0.76	22.5	41.6	4.0	37.6	135.0
7/15-7	6.18	0.84	23.1	0.75	20.3	58.4	12.0	46.4	135.0
7/16-4	6.25	0.85	23.8	0.77	22.8	89.3	8.0	81.3	120.0
7/16-7	6.0	0.81	22.0	0.71	21.3	61.1	4.0	57.1	140.5
7/17-1	5.95	0.81	22.0	0.71	20.0	43.9	8.0	35.9	144.1
7/19-1	5.9	0.80	21.9	0.71	20.3	62.5	8.0	54.5	144.1
7/19-2	5.9	0.80	21.5	0.70	19.9	72.4	6.0	66.4	144.1
7/21-1	6.0	0.81	22.0	0.71	19.3	94.8	12.0	82.8	141.5
7/21-2	5.95	0.81	21.9	0.71	21.1	71.9	2.0	69.9	142.2
7/21-3	5.9	0.80	21.3	0.69	20.4	31.6	4.0	27.6	144.1
7/21-4	5.85	0.79	21.0	0.68	20.4	60.9	2.0	58.9	147.6

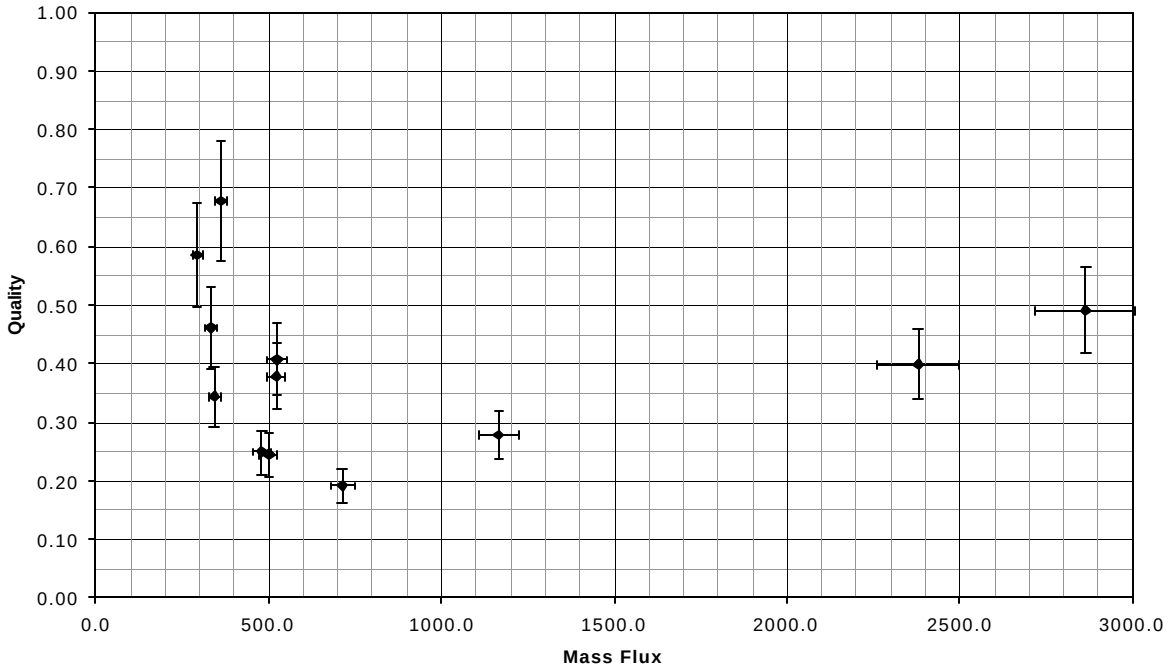

Figure 4.2 Quality vs. Mass Flux at the Critical Heat Flux

4.3.2 Comparison of the Observed Critical Heat Flux with Predicted Values

Several correlations are available which predict the critical heat flux in tube flow (Collier and Thome, 1996). The Shah upstream conditions correlation (UCC) was chosen to compare the experimental data to predicted values, as the experimental parameters fall under the suggested parameter limits. The UCC is an experimental curve fit based on 1046 data points (for $x_{crit} > 0$) from 23 fluids and 62 sources, with a mean deviation of 15.4% and with 12.3% of the data points with deviations of greater than 30% from the mean.

$$q''_{crit} = (Bo)(G)(i_{fg}) \tag{4.7}$$

$$Bo = 0.124\left(\frac{D}{z_{eq}}\right)^{0.89}\left(\frac{10^4}{Y}\right)^{n}\left(1 - x_{i\,eq}\right) \tag{4.8}$$

$$Y = \left[\frac{GDc_{pf}}{k_f}\right]\left[\frac{G^2}{r_f^2 gD}\right]^{0.4}\left[\frac{m_f}{m_g}\right]^{0.6} \tag{4.9}$$

This correlation is used when the critical heat flux depends on the upstream conditions, including inlet subcooling and heated channel length. The Shah local conditions correlation (LCC) relates the critical heat flux to the local fluid quality. The choice of which to use is dependent on the parameter Y. For all test conditions, $Y \leq 10^6$, for which the UCC is recommended. The UCC parameter limits are as follows:

$0.315 < D < 37.5$ mm
$1.3 < z/D < 940$
$4 < G < 29{,}051$ kg/m^{2}s
$0.0014 < P_r < 0.96$

$$-4 < x_i < +0.85$$
$$-2.6 < x_{crit} < +1$$

The experimental parameters were as follows:

$$D_h = 0.53 \text{ mm}$$
$$z/D_h = 95$$
$$300 < G < 2900 \text{ kg/m}^2\text{s}$$
$$P_r \leq 6.2/7.383 = 0.84$$
$$x_i \approx 0$$
$$0 < x_{crit} < 1$$

The parameter z_{eq} is the effective tube length, which for a subcooled liquid at the channel entrance is equal to the channel length from the inlet to the point of the critical heat flux. This length was difficult to determine experimentally; therefore, z_{eq} is taken as the total channel length of 0.051 m. For $Y \leq 10^4$, n = 0, and for $Y > 10^4$ n is given by the relationship:

$$n = \left(\frac{D}{z_{eq}}\right)^{0.33} = \left(\frac{0.53}{51}\right)^{0.33} = 0.222 \qquad (4.10)$$

An EES program was developed to compute the critical heat flux using the Shah UCC. The program determines all property values using the Span and Wagner (1996) data for a given temperature and pressure. Table 4.3 shows the calculated parameter values of the Shah UCC, and Figure 4.3 shows the comparison of the observed critical heat flux to the predicted UCC values.

Table 4.3 Critical Heat Flux Using the Shah UCC

Temp.	G	Y	Pres.	i_{fg}	n	Bo	Predicted q_crit	Observed q_crit
°C	kg/m^{2}s		kPa	kg/kJ			kW/m^2	kW/m^2
24.1	500.8	861.9	6200	129	0	0.002133	137.8	53.87
23.5	1166.6	4013	6150	135	0	0.002133	336	131.89
23.1	343.2	483.6	6150	135	0	0.002133	98.9	54.44
24.5	362.4	474.2	6230	120	0	0.002133	92.8	87.86
22.3	525.0	238.3	6000	140.5	0	0.002133	75.5	87.13
21.3	481.2	755.9	5900	144.1	0	0.002133	147.9	57.34
21.8	523.8	813.9	5900	144.1	0	0.002133	161.0	88.95
21.5	333.3	377.3	5900	144.1	0	0.002133	102.5	65.53
22.3	293.6	298.6	5970	141.5	0	0.002133	88.7	75.61
21.9	2864.9	17912	5930	142.2	0.222	0.001874	763.6	559.14
21.3	714.2	1539	5900	144.1	0	0.002133	219.6	61.21
21	2380.8	12291	5820	147.6	0.222	0.002038	716.1	394.03

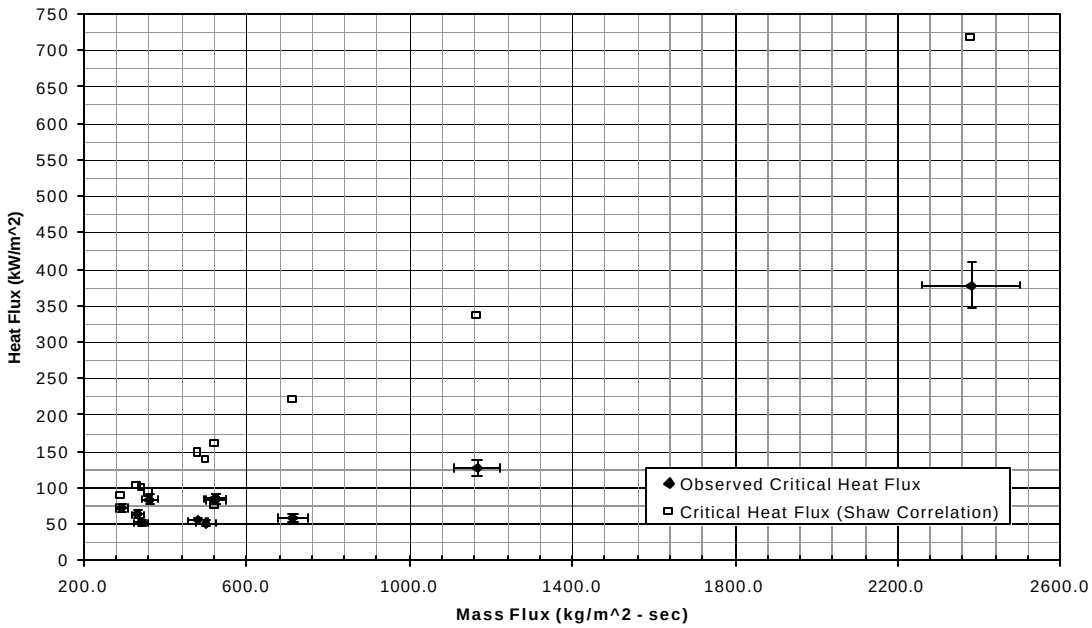

Figure 4.3 Observed vs. Predicted Critical Heat Flux

4.4 Discussion

Figure 4.1 shows that the critical heat flux phenomenon occurs at less that x = 0.8 for all experimental tests, and lower than x=0.5 for 8 of the 12 tests. These qualities correspond to critical heat fluxes which in all but one case were lower than predicted by the Shah correlation (exception at G = 525.0 kg/m^2-sec). All tests except July 21 Tests 2 and 4 are conducted with mass fluxes applicable to compact heat exchangers. Tests 2 and 4 are included for completeness. However, the applied heat flux was greater than that seen in compact heater applications. If use of the Shah correlation is applicable to CO_2 under these conditions, then the critical heat flux in these tests are occurring at much lower vapor qualities than expected, and would confirm the observations of Pettersen *et al.* (2000). It is noted that the observed temperature increase along the wall after the critical heat flux was less than predicted – at a heat flux of 100 kW/m^2 the predicted temperature jump is approximately 12°C, whereas the observed temperature jump was approximately 3-5°C. The fluoroptic thermometer temperature sampling limitations, rewetting of the channel wall, and over-prediction of the applied heat flux can account for the discrepancy.

Visually, the flow appeared clear in the saturated liquid and vapor states, and became milky-white in the two-phase region. This milky-white appearance occurred when the applied heat flux brought the CO_2 into the two phase region, and also when a high mass flux (~2000 kg/m^2-sec) underwent significant throttling in the channel. Both situations effectively moved the CO_2 into a region of higher vapor quality. It is hypothesized that the presence of bubbles with diameters much smaller than the channel width caused the opaque appearance. At the critical heat flux, a thin, uniform flow of these bubbles was observed. The density of bubbles in the flow was not sufficient to affect the transmissivity of the fluorescent temperature signal. Under the high mass flow rate throttling process, however, the bubble density became great enough to make the flow completely opaque.

Chapter 5: Conclusions and Recommendations

5.1 Conclusions

A microchannel test section has been developed to perform flow visualization and non-invasive temperature measurements on near-critical CO_2. A glass window allows direct observation of the CO_2 flow characteristics in the microchannel and non-invasive temperature measurements along the channel using a fluoroptic remote-sensing thermometer. A CO_2 delivery system was designed to allow thermodynamic control over the CO_2 state at the test section inlet. The fluoroptic thermometer was used to detect rapid temperature fluctuations at locations along the channel wall. The fluoroptic thermometer was also used to establish that a subcooled liquid entered the microchannel and that the wall temperature exceeded the saturation temperature at the microchannel exit, establishing that the rapid temperature fluctuations indicated the de-wetting associated with the critical heat flux.

The fluoroptic thermometer was used to measure channel wall temperatures during the evaporation of CO_2 in the microchannel geometry. The resolution of and dynamic response of this measurement system allowed the detection of a precipitous drop in local heat transfer coefficient, manifest as rapid temperature fluctuations at measured locations along the channel. During the experiments, the fluoroptic thermometer was also used to verify that CO_2 entered the test section as a subcooled liquid. Thus, the location at which a precipitous drop in the heat transfer coefficient during evaporation heat transfer was observed is taken as the de-wetting phenomenon associated with the critical heat flux.

Although this inference and nomenclature is consistent with the existing technical literature, it should be noted that no direct measurements of wall de-wetting were obtained in these experiments. The de-wetting mechanism causing the sudden drop in the heat transfer coefficient is not absolutely clear. The importance of this work lies in confirming that a behavior consistent with the de-wetting phenomenon associated with the critical heat flux occurs at a relatively low quality for CO_2 in a microchannel under the conditions of this study.

The data presented in Section 4 show that critical heat flux generally occurs at vapor qualities at or below $x = 0.5$, and that the observed critical heat flux is below the values predicted using the Shah (1987) correlation. These data are in agreement with the findings of Pettersen *et al.* (2000). However, while the mass flux fell in the same range as tested by Pettersen *et al.*, the heat flux was approximately 4-10 times higher (not including data points significantly out of the applied heat and mass flux range). The boiling regimes encountered in these experiments may not be the same as those encountered at a lower heat flux, which may affect the conclusion of a critical heat flux below predicted values. Additionally, the Shah correlation is empirical, which questions the applicability of its use with regards to CO_2.

The Shah UCC was chosen because the experimental parameters fell within the recommended applicable correlation parameters, and because the Shah correlation was developed using several different fluids. The Shah correlation does not distinguish between DNB and dryout, but instead predicts the critical heat flux corresponding to the decrease in the heat transfer coefficient. Additionally, the Shah correlation is applicable to reduced pressures of up to 0.96. Therefore, the correlation should account for near-critical effects, in addition to the mass and heat flux effects. However, the UCC does not specifically account for property variations of CO_2, and may not be applicable

to near-critical CO_2. Pettersen *et al.* (2000) hypothesize that dryout accounts for the heat transfer coefficient decrease at low vapor qualities. While the data in this thesis supports this claim, the test conditions between the two studies are somewhat different. Therefore, it is desired to know whether the flow regimes encountered in this study are equivalent to the lower heat flux studies.

At a low heat fluxes dryout is associated with the critical heat flux, whereas at a greater heat fluxes DBN is associated with the critical heat flux (see Figure 1.2). In this region convective boiling is never reached, and nucleate boiling transcends directly to saturated film boiling. At very high heat flux levels, subcooled liquid may enter the film boiling regime at the channel inlet. The fluoroptic thermometer and wall thermocouples confirm that condition did not occur in these experiments.

As the heat flux increases, the critical heat flux occurs at decreasing vapor qualities, including x=0 for a sufficiently large heat flux. However, the transition from dryout to DNB with increasing heat flux is smooth (see Figure 1.2). The Shah correlation predicts the critical heat flux regardless of the mechanism, suggesting the important parameter is the critical heat flux value. Under this criterion it does not matter whether dryout or DNB is the mechanism for the decrease in the heat transfer coefficient. What is important is that the critical heat flux occurs at lower values than predicted by the Shah correlation, corresponding to lower-that-expected vapor qualities.

5.2 Experimental Apparatus Modifications

The greatest uncertainties associated with observing and maintaining the critical heat flux in the test section were inaccuracies in the mass flow rate, achieving and maintaining subcooled liquid at the channel inlet, and interpreting the fluoroptic thermometer signal.

5.2.1 Mass Flow Rate

The use of a source cylinder venting to the atmosphere and a needle valve at the exit line to control the mass flow rate caused a number of experimental uncertainties. Numerous tests were discarded due to unsteady flow in the channel at low mass flow rates, especially when the subcooled liquid underwent a phase change in the channel. These flow effects may be responsible for oscillations in the temperature and pressure observed in some preliminary tests. Additionally, the alternating freezing and heating of the exit needle valve made an integrated approach to determining the mass flow rate difficult, and many tests were discarded due to inaccurate mass flow rate interpretation. A significant help would be acquiring a voltage signal output from the scale to the DAS, so that a time stamp is associated with the source cylinder mass during the test. The mass flow rate could then be determined at the exact point the critical heat flux was maintained in the system. Alternatively, the use of a mass flow rate meter could be examined, although this concept was initially disregarded due to the low mass flow rates.

5.2.2 Inlet Test Section Conditions

The test section was designed to incorporate several possible test parameters – visual observations and non-intrusive temperature measurements, conventional temperature and pressure measurements, and supercritical and evaporation test conditions. Flow visualization and the non-intrusive temperature measurements necessitated a removable glass window that could maintain high-pressure flow within the microchannel. It was determined the best way to incorporate this window was to have the inlet and outlet ports at right angles to the microchannel, so that an o-ring could encircle both ports and the channel. Lockdown screws could then compress the window, creating a

seal. In practice this approach had several problems. First, a glass-on-metal seal at the channel lip could result in either overcompression of the glass, cracking the window, or undercompression of glass, resulting in an ineffective seal. This problem was alleviated by injecting a rubber sealant in the dead areas around the o-ring. However, pressure and/or viscous forces required reapplication of the sealant after a few runs, with the associated 24-hour curing period. Additionally, the sealant could run into the microchannel, required the process to be repeated.

The inlet piping geometry also was not ideal. The constriction in piping diameter leading to the channel inlet and the right-angle bends made maintaining a subcooled liquid at the channel inlet difficult. A chemical sealing process, rather than the mechanical o-ring process, might have reduced both this problem and the sealing problem described above. Crystalbond™ is a hard wax used to temporally glue silicon wafers or glass samples for various cutting applications. Below 100°C this and similar adhesives exhibit high bond strength and adhere readily to metals, glass and ceramics. However, above 100°C the adhesive loses this bond strength and the viscosity becomes very low. The window could be removed by heating the test section to the wax melting point and cleaning with the appropriate solvent. This heat would not affect the fluorescent phosphor.

Using this adhesive to bond the glass window to the microchannel (in conjunction with lockdown screws, if required) would negate the need for the o-ring, reducing the sealing problems while relieving the restriction that the inlet and outlet port approach at right angles to the microchannel. The line from the regulator to the test section could be cooled using the ethylene glycol bath, then thermally isolated with a Teflon washer or other device. The CO_2 would then be cooled until just before it entered the test section, undergoing one reduction in piping diameter before entering the microchannel in-line, with pressure transducers and flow thermocouples coming at right-angles to the flow. This would significantly reduce the problem of flow-heating before entering the test section

5.2.3 Non-Invasive Temperature Measurements

Instrumentation limitations prohibit the use of the fluoroptic thermometer for highly precise rapid temperature measurements, although the techniques used in these experiments were adequate for determining the critical heat flux condition. As the de-wetting phenomenon is not a stagnant condition that occurs at signal point downstream of the channel inlet, one modification may be a temperature sensor which is able to read a temperature profile across the axial length, instead of at discrete points.

5.3 Further Research

Microchannel heat transfer is a poorly understood phenomenon, and while significant inroads have been made in recent years towards understanding specific heat transfer mechanisms, much work is needed for a complete understanding. Significant questions remain concerning the flow patterns and regimes encountered at different mass and heat fluxes, including the importance of nucleate vs. force convective heat transfer, which in turn will determine the mechanism responsible for the heat transfer coefficient decrease at the critical heat flux. A microchannel flow map would assist in understanding the different flow and heat transfer regimes as a function of quality, heat flux, and mass flux. This experimental setup with the suggested modifications and a high-resolution camera could assist in flow visualization and correlating flow patterns to observed heat transfer. This work could be used to further understand CO_2 transport characteristics in microchannels.

This research indicates the critical heat flux is underpredicted by the Shah correlation, and that the vapor quality at the critical heat flux is lower than in conventional refrigeration systems. In addition to achieving a better understanding of microchannel transport phenomenon, new compact heat exchanger design criteria should be developed which incorporate early critical heat fluxes.

List of References

Adebiyi, G.A., Hall, W.B. (1976) Experimental Investigation of Heat Transfer to Supercritical Pressure Carbon Dioxide in a Horizontal Pipe. J. Heat Mass Transfer, v.19 pp. 715-720

Bellinghausen, R., Renz, U. (1990) Pseudocritical Heat Transfer Inside Vertical Tubes. Chemical Engineering & Processing, v.28 no.3 pp.183-186

Bodinus, W.S. (1999) The Rise and Fall of Carbon Dioxide Systems. ASHRAE Journal: pp.37-42

Carey, V.P. (1992) Liquid-Vapor Phase-Change Phenomena, Series in Chemical and Mechanical Engineering. Hemisphere Publishing Inc.

Choi, S.B., Barron, R.F., Warrington, R.O. (1991) Liquid Flow and Heat Transfer in Microtubes. Micromechanical Sensors, Actuators, and Systems, ASME DSC 32: 123-134

Collier, J.G., Thome, J.R. (1996) Convective Boiling and Condensation, Third Edition (paperback). Oxford Engineering Science Series, Oxford University Press

Farman, J., Gardiner, B, Shanklin, J. (1985) Large Losses Of Total Ozone In Antarctica Reveal Seasonal Cl0x/Nox Interaction. Nature 315: 207-10.

Ghajar, A.J., Asadi, A. (1986) Improved Forced Convective Heat-Transfer Correlations For Liquids In The Near-Critical Region. AIAA Journal. v. 24 n 12 p 2030-2037

Gnielinski, V. (1976) New Equations for Heat and Mass Transfer in Turbulent Pipe and Channel Flow. International Chemical Engineering, v.16, no.2 pp.359-368

Griem, H. (1996) New Procedure For The Prediction Of Forced Convection Heat Transfer At Near- And Supercritical Pressure. Heat and Mass Transfer. v 31 n 5. p301-305

Hall, W.B. (1971) Heat Transfer Near the Critical Point. Advances in Heat Transfer 7:1-86

Incropera, F.P., DeWitt, D.P. (1996) Fundamentals of Heat and Mass Transfer, Fourth Ed., John Wiley & Sons, Inc.

Jackson, J.D., Fewster, J. (1975) AERE-R8158, Harwell

Kasao, D., Ito, T. (1989) Review Of Existing Experimental Findings On Forced Convection Heat Transfer To Supercritical Helium 4. Cryogenics. v 29 n 6 p 630-636

Kasza, K.E., Wambsganss, M.W. (1994) Development of a Small-Channel Nucleate-Boiling Heat Transfer Correlation. Argonne National Laboratory Report, ANL-94/32

Krasnoshchekov, E.A., Kuraeva, I.V., Protopopov, V.S. (1969) Local Heat Transfer Of Carbon Dioxide At Supercritical Pressure Under Cooling Conditions. [Journal Paper] Teplofizika Vysokikh Temperatur, vol.7, no.5, pp.922-30. USSR.

Krasnoshchekov, E.A., Protopopov, V.S. (1971) A Generalized Relationship For Calculation Of Heat Transfer To Carbon Dioxide At Supercritical Pressure (pi =1.02-5.25). [Journal Paper] Teplofizika Vysokikh Temperatur, vol.9, no.6, pp.1314. USSR.

Krasnoshchekov, E.A., Protopopov, V.S. Parkhovnik, I.A., Silin, V.A. (1971) Some Results Of An Experimental Investigation Of Heat Transfer To Carbon Dioxide At Supercritical Pressure And Temperature Heads Of Up To 850C. [Journal Paper] Teplofizika Vysokikh Temperatur, vol.9, no.5, pp.1081-4. USSR.

Kurganov, V.A., Kaptilnyi, A.G. (1993) Flow Structure And Turbulent Transport Of A Supercritical Pressure Fluid In A Vertical Heated Tube Under The Conditions Of Mixed Convection. Experimental Data. International Journal of Heat & Mass Transfer. v 36 n 13 p 3383-3392

Lorentzen, G. (1994) Revival Of Carbon Dioxide As A Refrigerant Part 2. H&V Engineer. v 67 n 722 p 10-12

Lorentzen, G. (1994) Revival Of Carbon Dioxide As A Refrigerant H&V Engineer. v 66 n 721. p 9-14

Lorentzen, G., Pettersen, J. (1992) New Possibilities for Non-CFC Refrigeration. Proceedings of IIR International Symposium on Refrigeration, Energy and Environment, Trondheim, Norway, 22-24 June 1992, PP 147-163

Mala, G.M., Li, D., Dale, J.D. (1997) Heat Transfer And Fluid Flow In Microchannels. International Journal of Heat & Mass Transfer. v 40 n 13 p 3079-3088

Mehendale, S.S., Jacobi, A.M., Shah, R.K. (2000). Fluid Flow and Heat Transfer at Micro- and Mesos-Scales with Application to Heat Exchanger Designs. Applied Mechanics Reviews, v 53 n 7 p 175-193

Mori, H., Ogata, H. (1991) Natural Convection Heat Transfer Of Supercritical Helium In A Channel. Trans. JSME,. v 57 n 542 B p 3465-3468

Morrisette, P.M. (1989) The Evolution of Policy Responses to Stratospheric Ozone Depletion. Natural Resources Journal 29 pp. 793-820.

Olsen, D.A., Allen, D. (1998) Heat Transfer in Turbulent Supercritical Carbon Dioxide Flowing in a Heated Horizontal Tube. U.S. Department of Commerce, Technology Administration. NISTIR Report 6234

Peng, X.F., Hu, H.Y., Wang, B.X (1998) Boiling Nucleation During Liquid Flow in Microchannels. International Journal of Heat & Mass Transfer. v 41 n 1 PP. 101-106

Peng, X.F., Peterson, G.P., Wang, B.X. (1994) Frictional Flow Characteristics of Water Flowing Through Rectangular Microchannels. Experimental Heat Transfer. v 7 n 4 PP 249-264

Peng, X.F., Peterson, G.P., Wang, B.X. (1994) Heat Transfer Characteristics of Water Flowing Through Microchannels. Experimental Heat Transfer. v 7 n 4 PP 265-283

Peng, X.F., Pettersen, G.P. (1995) Convective Heat Transfer and Flow Friction for Water Flow in Microchannel Structures. International Journal of Heat & Mass Transfer. v 39 n 12 PP. 2599-2608

Peng, X.F., Wang, B.X. (1993) Forced Convection And Flow Boiling Heat Transfer For Liquid Flowing Through Microchannels. International Journal of Heat & Mass Transfer. v 36 n 14 pp. 3421-3427

Pettersen, J., Hafner, A., Skaugen, G., Rekstad, H. (1998) Development Of Compact Heat Exchangers For CO2 Air-Conditioning Systems. International Journal of Refrigeration. v 21 n 3 p180-193

Pettersen, J., Rieberer, R., Munkejord S.T. (2000) Heat Transfer and Pressure Drop for Flow of Supercritical and Subcritical CO2 in Microchannel Tubes. Final Technical Report, for United States Army, Contract Number N-68171-99-M-5674. Through SINTEF Energy Research/Norwegian University of Science and Technology

Petukhov, B.S., Krasnoshchekov, E.A., Protopopov, V.S. (1961) An Investigation of Heat Transfer to Fluids Flowing in Pipes Under Supercritical Conditions. Proceedings of the 2nd International Heat Transfer Conference, pp.569-578

Pfahler, J., Harley, J., Bau, H., Zemel J.N. (1991) Gas and Liquid Flow in Small Channels. Micromechanical Sensors, Actuators, and Systems, ASME DSC 32: 49-60

Pitla, S.S., Robinson, D.M., Groll, E.A., Ramadhyani S. (1998) Heat Transfer from Supercritical Carbon Dioxide in Tube Flow: A Critical Review, HVAC&R Research, v3 Issue 4, PP.: 281-301

Ravigururajan, T.S. (1998) Impact Of Channel Geometry On Two-Phase Flow Heat Transfer Characteristics Of Refrigerants In Microchannel Heat Exchangers. Journal of Heat Transfer-Transactions of the ASME. v 120 n 2 p 485-491

Ravigururajan, T.S., Cuta, J., McDonald, C.E., Drost, M.K. (1996) Effects Of Heat Flux On Two-Phase Flow Characteristics Of Refrigerant Flows In A Micro-Channel Heat Exchanger. American Society of Mechanical Engineers, Heat Transfer Division, (Publication) HTD. v 329 n 7 ASME, New York, NY, USA. p 167-178

Span, R., Wagner, W. (1996) A New Equation of State for Carbon Dioxide Covering the Fluid Region from the Triple-Point Temperature to 1100K at Pressures up to 800 MPa. J. Phys. Chem. Ref. Data., v.25 no.6

Tran, T.N., Wambsganss, M.W., France, D.M. (1996). Small Circular- And Rectangular-Channel Boiling With Two Refrigerants. International Journal of Multiphase Flow. v 22 n 3 pp. 485-498

Tran, T.N., Wambsganss, M.W., France, D.M., Jendrzejczyk, J.A (1993) Boiling Heat Transfer In A Small, Horizontal, Rectangular Channel. Heat Transfer–Atlanta, 1993, AIChE symposium Series, Vol. 89 PP. 253-261

Walisch, T., Dorfler, W., Trepp Ch. (1997) Heat Transfer to Supercritical Carbon Dioxide in Tubes with Mixed Convection. Proceedings of the 32nd National Heat Transfer Conference, v.12 pp.79-98

Wambsganss, M.W., France, D.M., Jendrzejczyk, J.A., Tran, T.N. (1993) Boiling Heat Transfer in a Horizontal Small-Diameter Tube. ASME J. Heat Transfer 115(4), 963-972

Wang, B.X., Peng, X.F. (1994) Experimental Investigation On Liquid Forced-Convection Heat Transfer Through Microchannels. International Journal of Heat & Mass Transfer. v 37 n SUPPL 1 Mar 1994. p 73-82

Webb, R.L., Zhang, M. (1997) Heat Transfer and Friction in Small Diameter Channels. Presented at the Workshop on Thermophysical Phenomena in Microscale Sensors, Devices and Structures. 1997 National Heat Transfer Conference, Baltimore, WA

White, F.M. (1991) Viscous Fluid Flow, Second Ed., McGraw-Hill Series in Mechanical Engineering, McGraw-Hill, Inc.

Wickersheim K.A, Sun, M.H. (1987). Fiberoptic Thermometry and its Applications. Journal of Microwave Power & Electromagnetic Energy, vol.22, no.2, pp.85-93.

Wu, P., Little, W.A. (1983) Measurement of Friction Factors for the Flow of Gases in Very Fine Channels used for Microminiature Joule-Thompson Refrigerators. Cryogenics, 23, 273-277

Wu, P., Little, W.A. (1984) Measurement of Heat Transfer Characteristics Of Gas Flow In Fine Channel Heat Exchangers Used For Microminiature Refrigerators. Cryogenics, 24, 415-423

Yanovskii, L.S., Kamenetsdii, B.Ya. (1991) Heat Exchange During The Forced Flow Of Hydrocarbon Fuels At Supercritical Pressures In Heated Tubes. Journal of Engineering Physics (English Translation of Inzhenerno-Fizicheskii Zhurnal). v 60 n 1 p 38-42

Appendix A: Experimental Data Sheets

The following are the DAS transducer and fluoroptic thermometer data sheets associated with the dryout measurements.

Fluoroptic Thermometer Temperature Measurements (deg C)

Sat. Temp = 24.0

Date 7/15 12:03:30 PM Test # 3 MFR 6.3 g/min HBVoltage 37.9

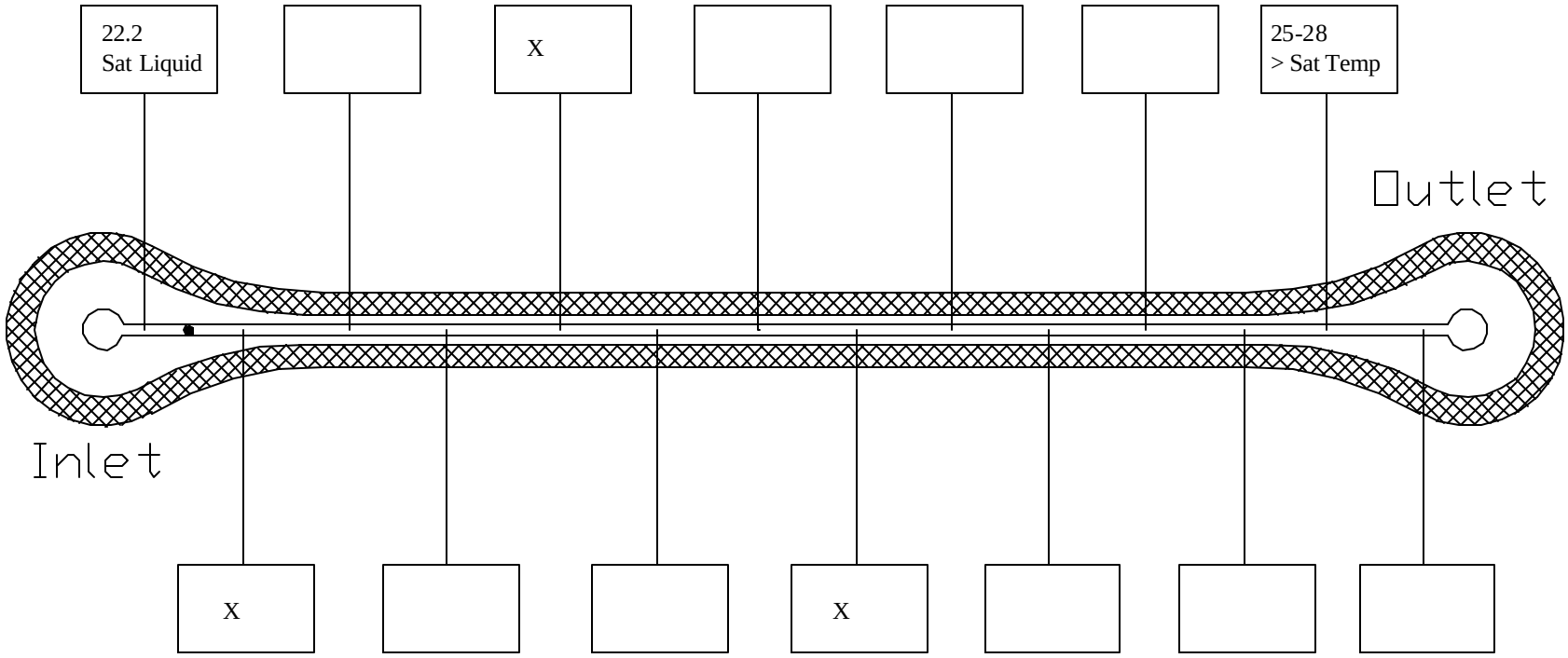

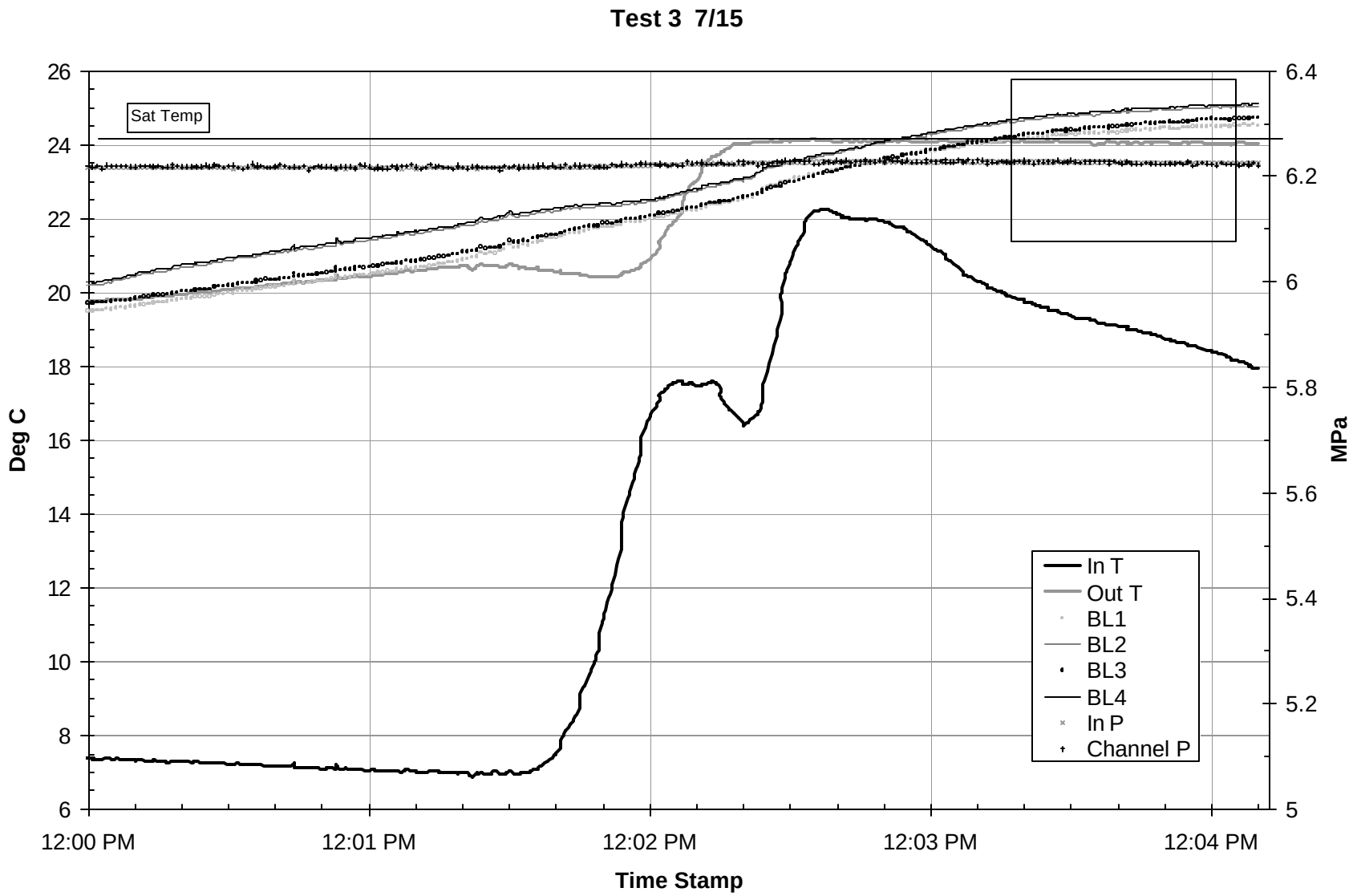
Test 3 7/15
Sat Temp
Deg C
MPa
Time Stamp
12:00 PM
12:01 PM
12:02 PM
12:03 PM
12:04 PM
In T
Out T
BL1
BL2
BL3
BL4
In P
Channel P

Fluoroptic Thermometer Temperature Measurements (deg C)

Sat. Temp = 23.5

Date 7/15 2:18:20 PM Test # 6 MFR 14.7 g/min HB Voltage 59.3

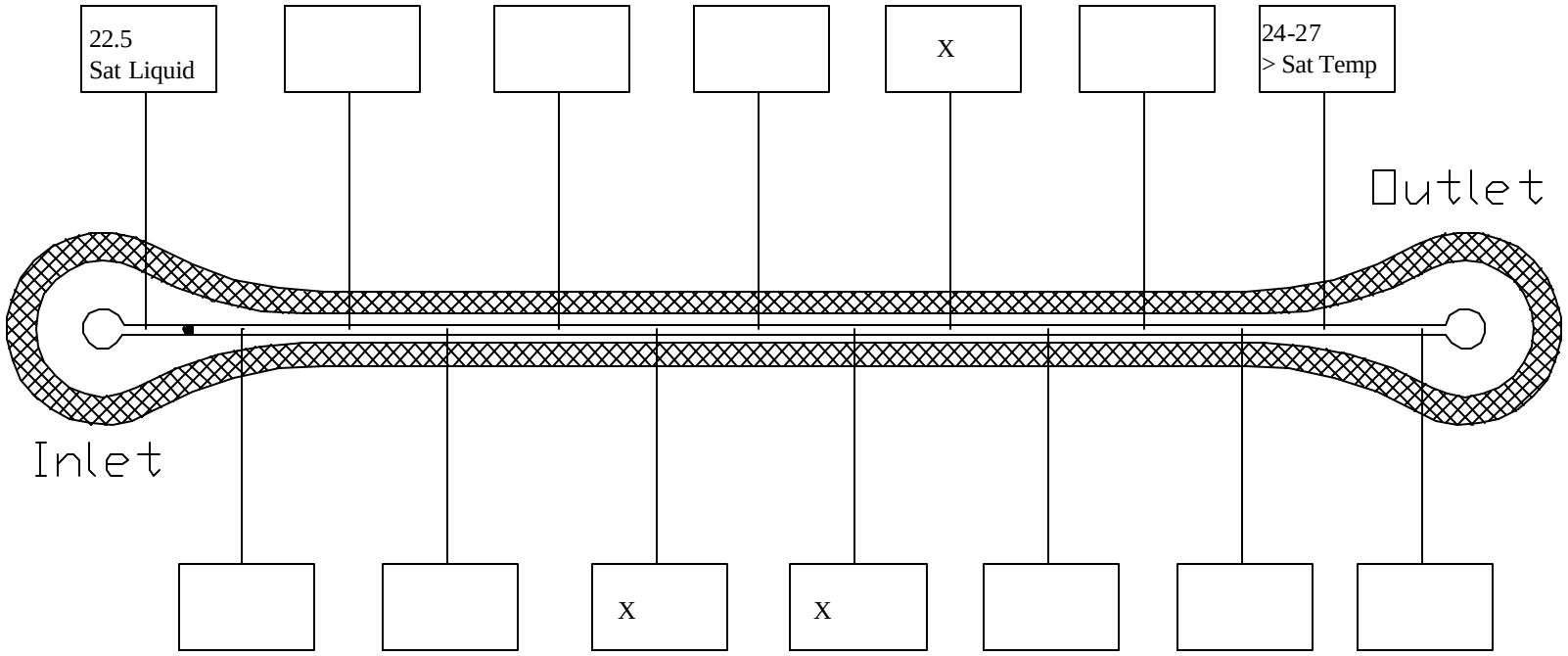

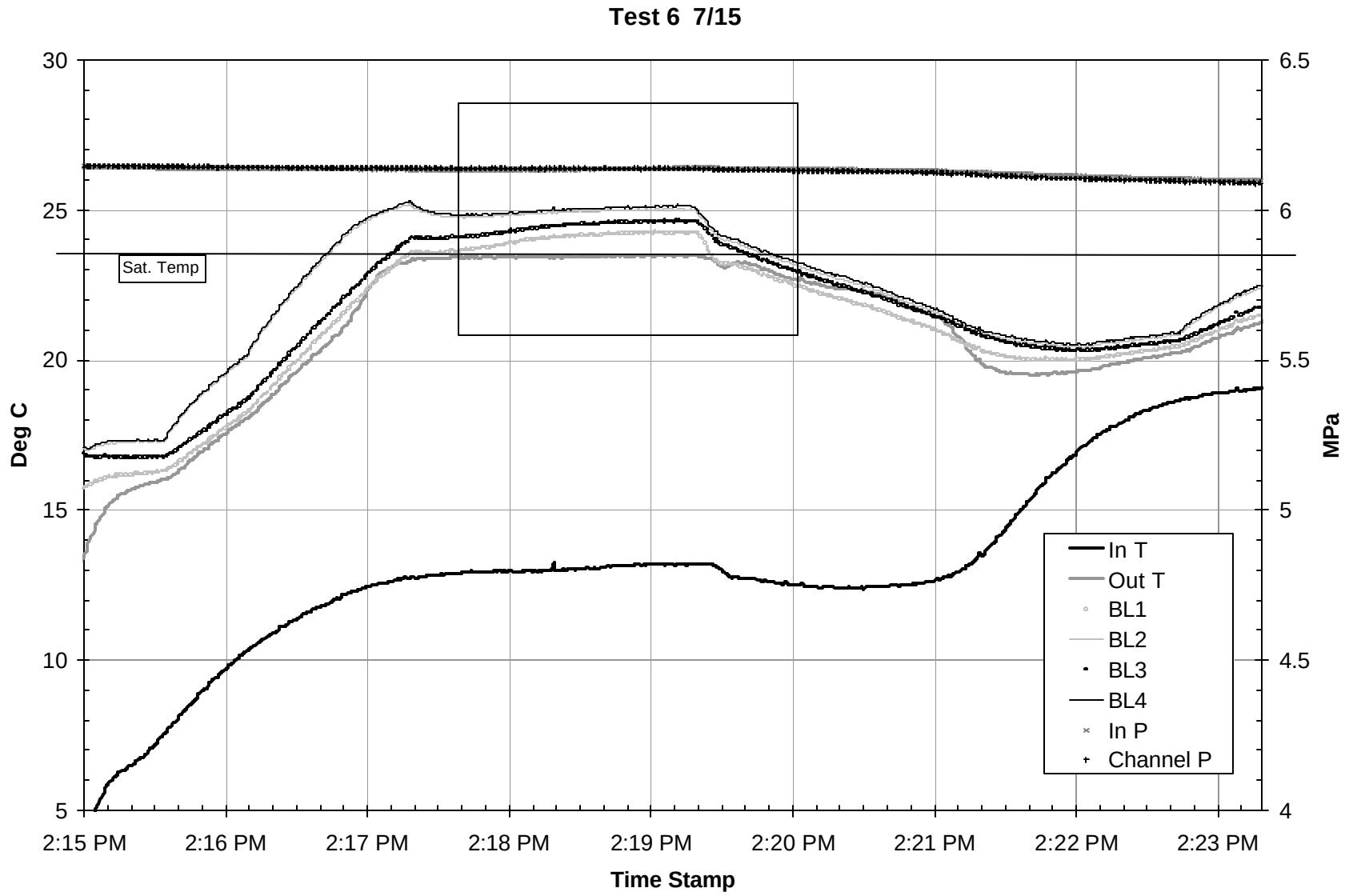
Test 6 7/15
Sat. Temp
Deg C
MPa
Time Stamp
30
25
20
15
10
5
6.5
6
5.5
5
4.5
4
2:15 PM
2:16 PM
2:17 PM
2:18 PM
2:19 PM
2:20 PM
2:21 PM
2:22 PM
2:23 PM
In T
Out T
BL1
BL2
BL3
BL4
In P
Channel P

Fluoroptic Thermometer Temperature Measurements (deg C)

Sat. Temp = 23.1

Date 7/15 4:28:20 PM Test # 7 MFR 4.3 g/min HB Voltage 38.1

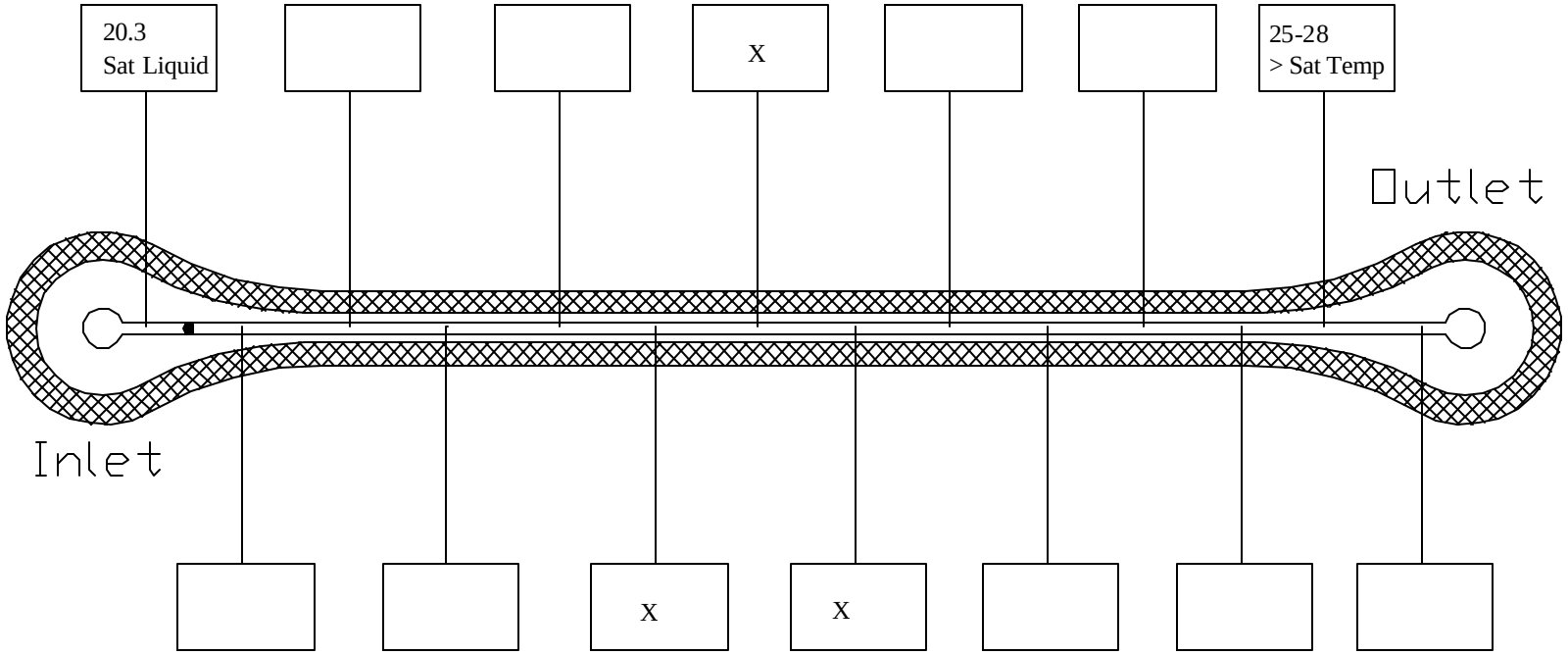

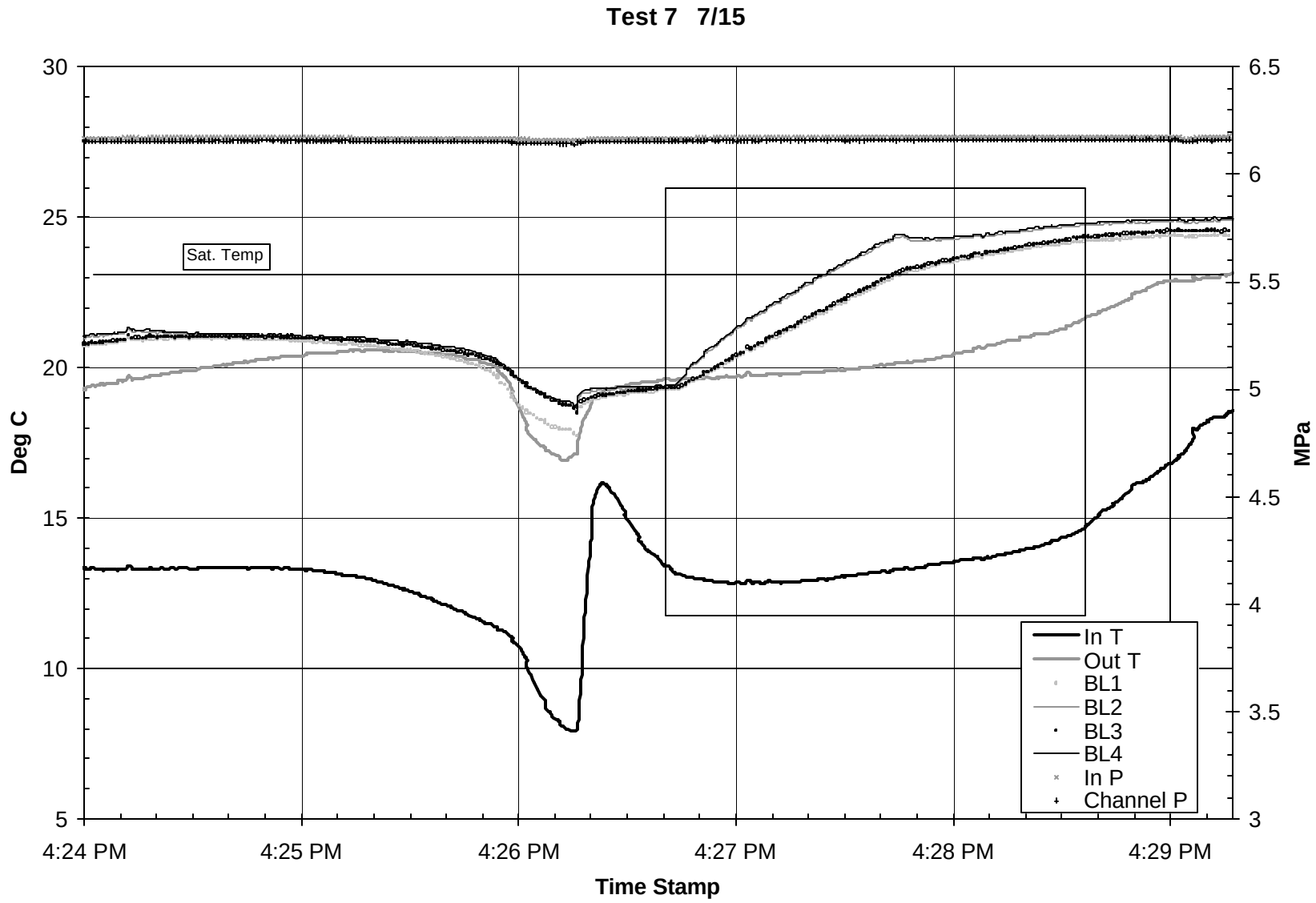
Test 7 7/15
Sat. Temp
Deg C
MPa
Time Stamp
30
25
20
15
10
5
6.5
6
5.5
5
4.5
4
3.5
3
4:24 PM
4:25 PM
4:26 PM
4:27 PM
4:28 PM
4:29 PM
In T
Out T
BL1
BL2
BL3
BL4
In P
Channel P

Fluoroptic Thermometer Temperature Measurements (deg C)

Sat. Temp = 23.8

Date 7/16 1:10:30 PM Test # 4 MFR 4.6 g/min HBVoltage 48.4

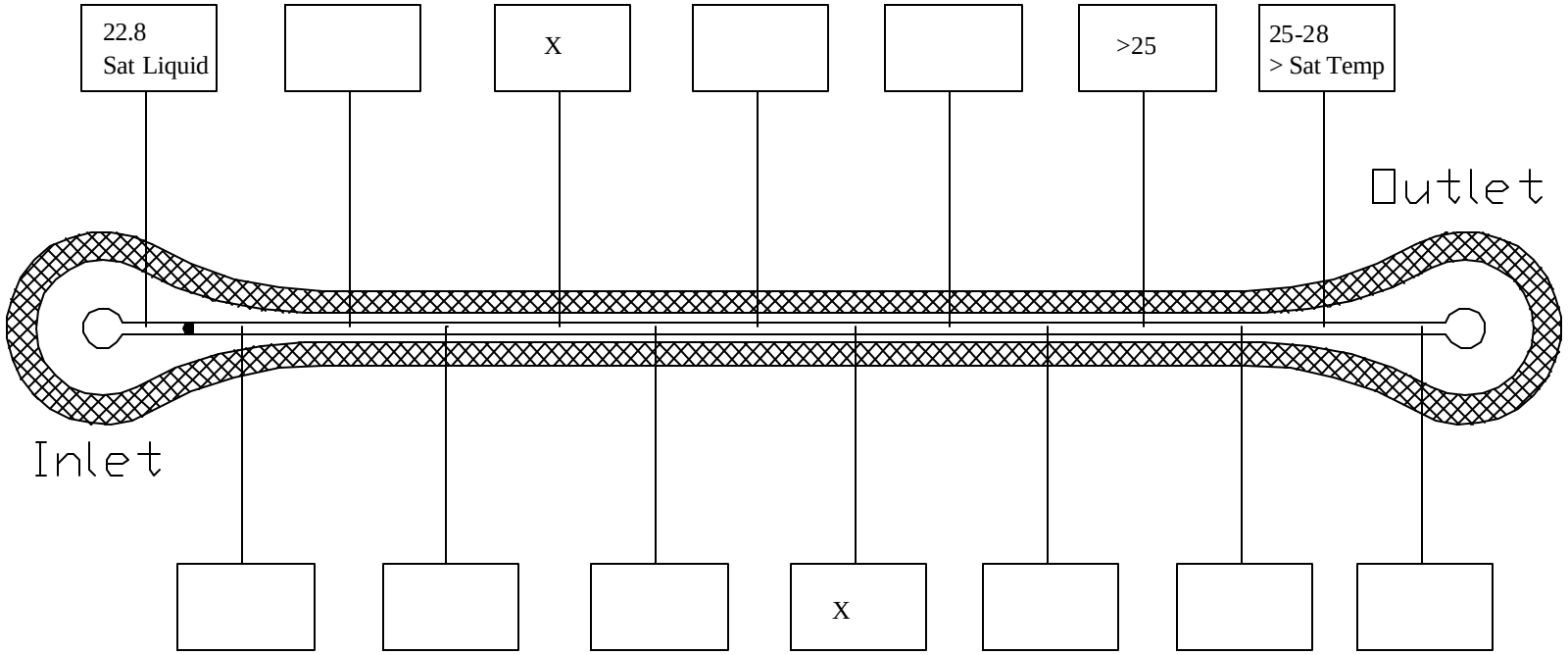

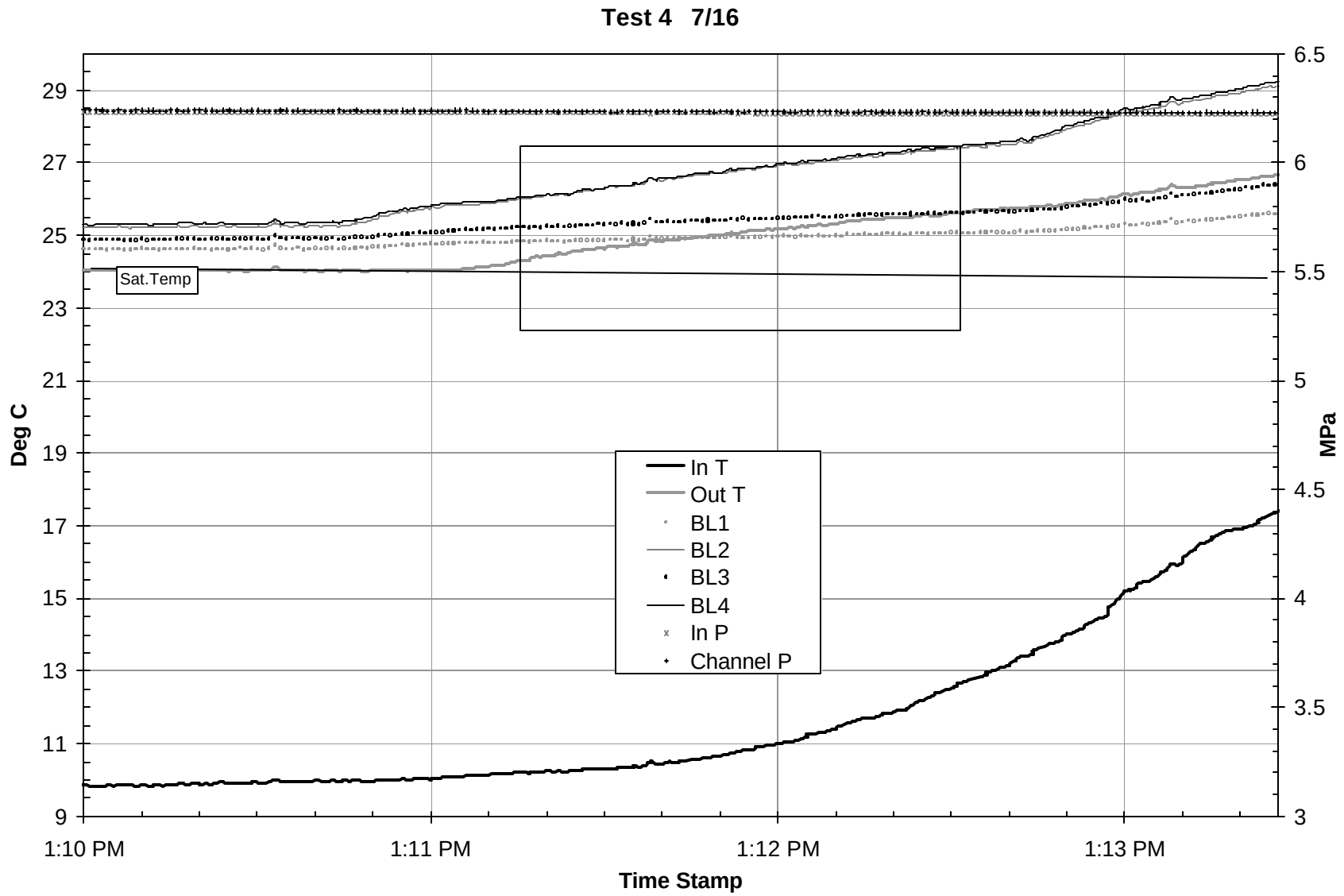
Test 4 7/16
Deg C
MPa
Time Stamp
1:10 PM
1:11 PM
1:12 PM
1:13 PM
9
11
13
15
17
19
21
23
25
27
29
3
3.5
4
4.5
5
5.5
6
6.5
Sat.Temp
In T
Out T
BL1
BL2
BL3
BL4
In P
Channel P

Fluoroptic Thermometer Temperature Measurements (deg C)

Sat. Temp = 22.0

Date 7/16 3:19 – 3:20 PM Test # 7 MFR 6.6 g/min HB Voltage 48.2

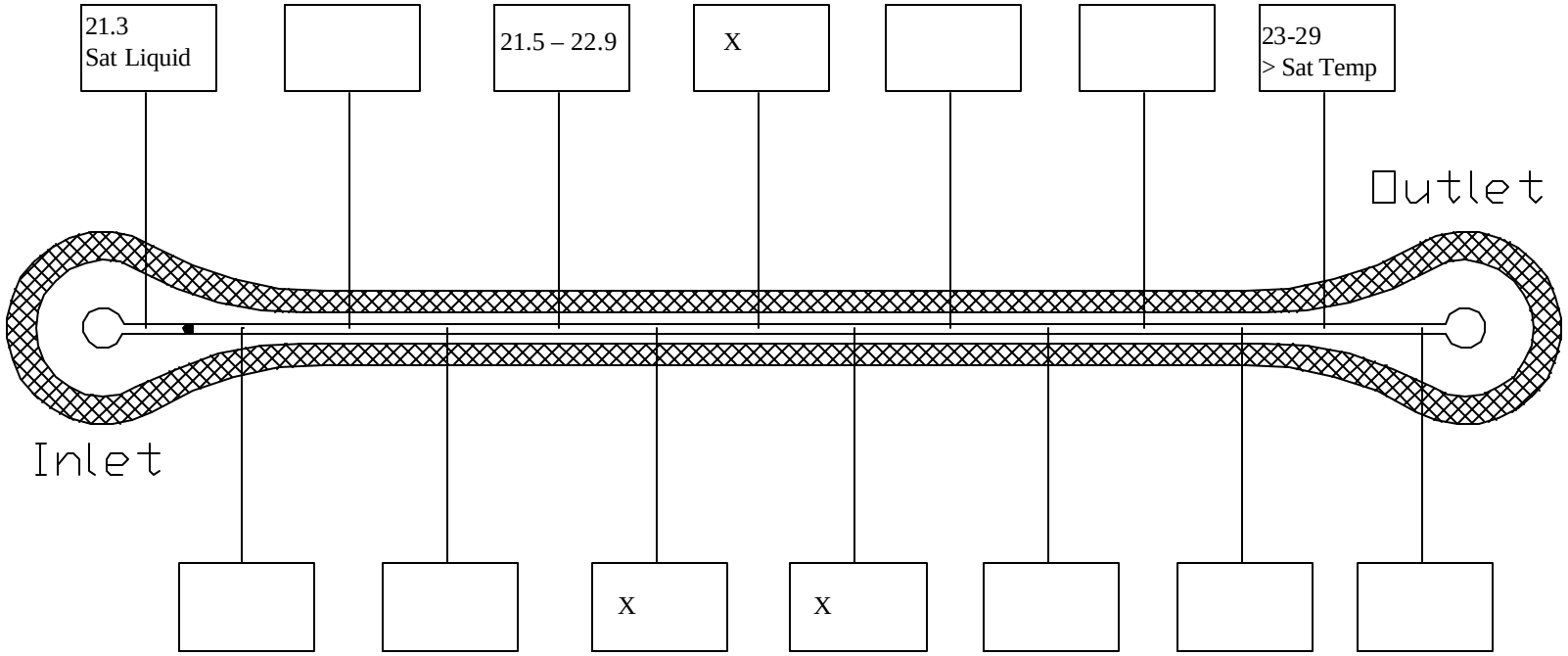

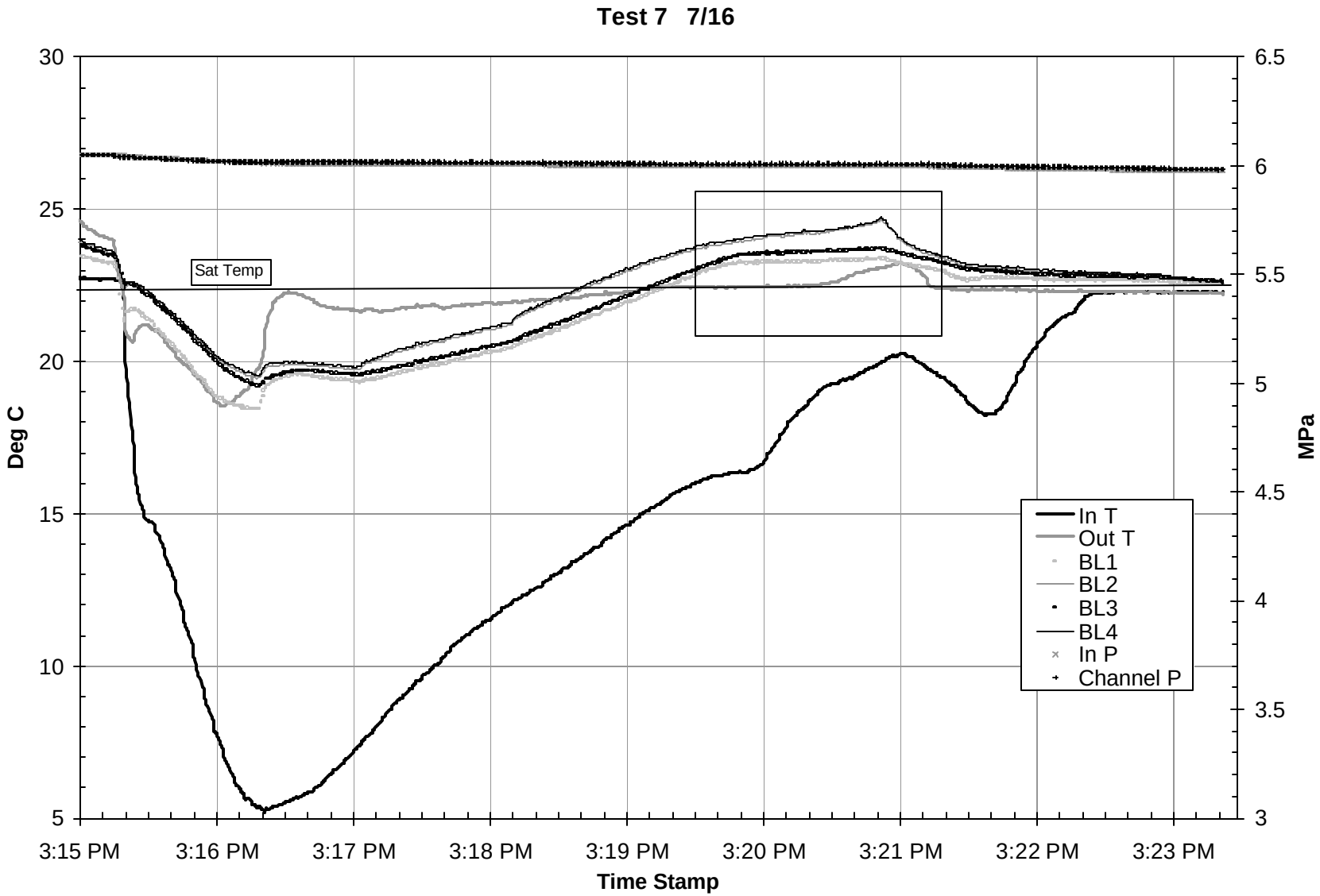
Test 7 7/16
Sat Temp
Deg C
MPa
Time Stamp
30
25
20
15
10
5
6.5
6
5.5
5
4.5
4
3.5
3
3:15 PM
3:16 PM
3:17 PM
3:18 PM
3:19 PM
3:20 PM
3:21 PM
3:22 PM
3:23 PM
In T
Out T
BL1
BL2
BL3
BL4
In P
Channel P

Fluoroptic Thermometer Temperature Measurements (deg C)

Sat. Temp = 22.0

Date 7/17 2:49:00 PM Test # 1 MFR 6.1 g/min HBVoltage 39.1

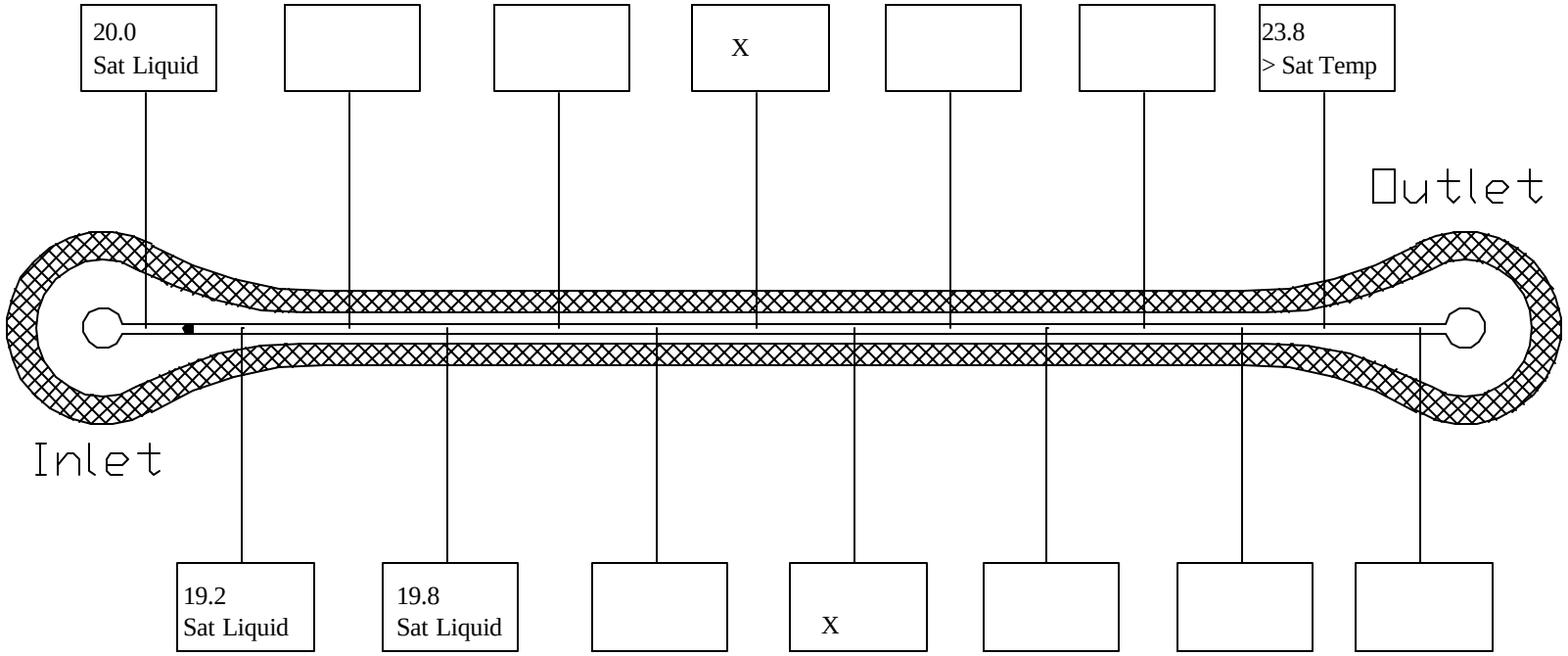

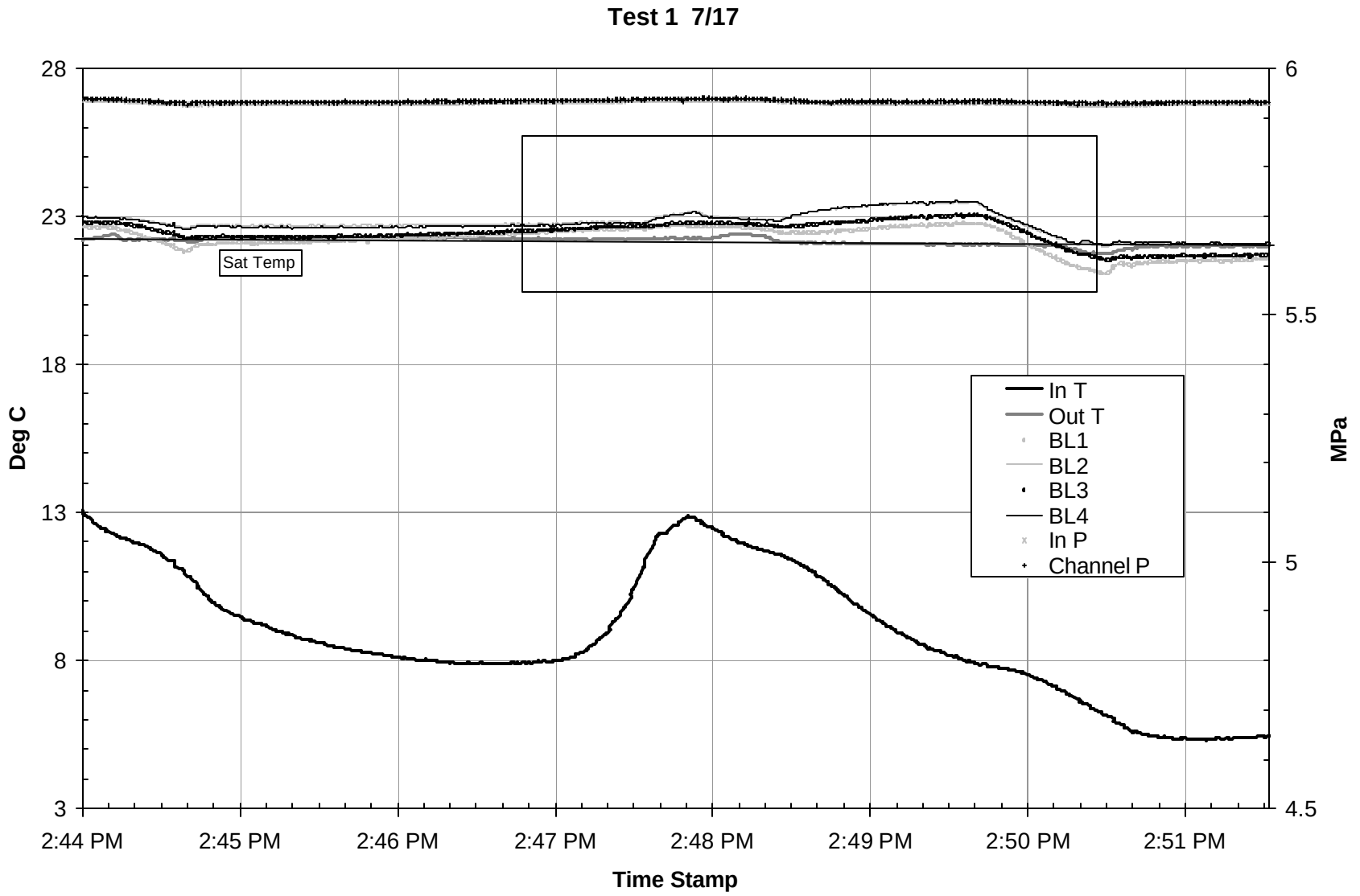
Test 1 7/17
28
23
18
13
8
3
6
5.5
5
4.5
Deg C
MPa
Sat Temp
In T
Out T
BL1
BL2
BL3
BL4
In P
Channel P
2:44 PM
2:45 PM
2:46 PM
2:47 PM
2:48 PM
2:49 PM
2:50 PM
2:51 PM
Time Stamp

Fluoroptic Thermometer Temperature Measurements (deg C)

Sat. Temp = 21.9

Date 7/19 1:50:50 PM Test # 1 MFR 6.6 g/min HBVoltage 48.7

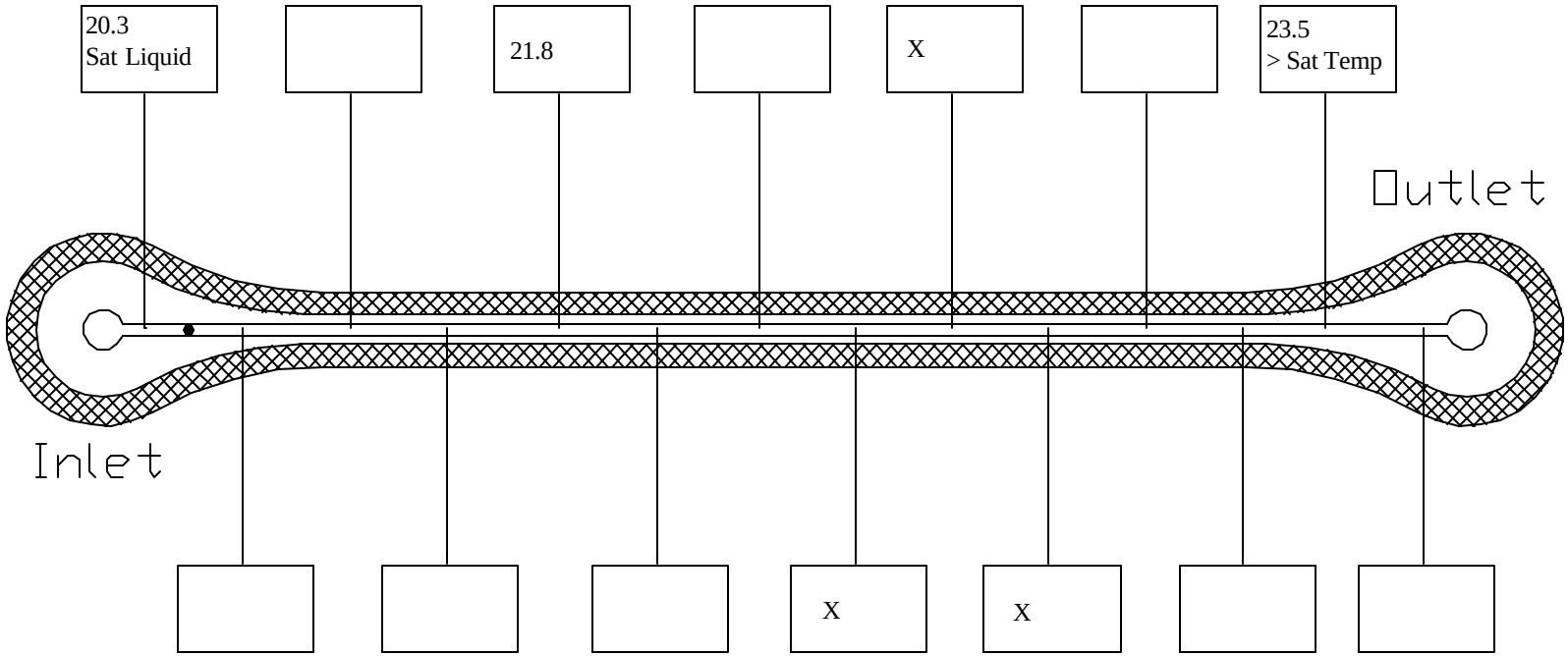

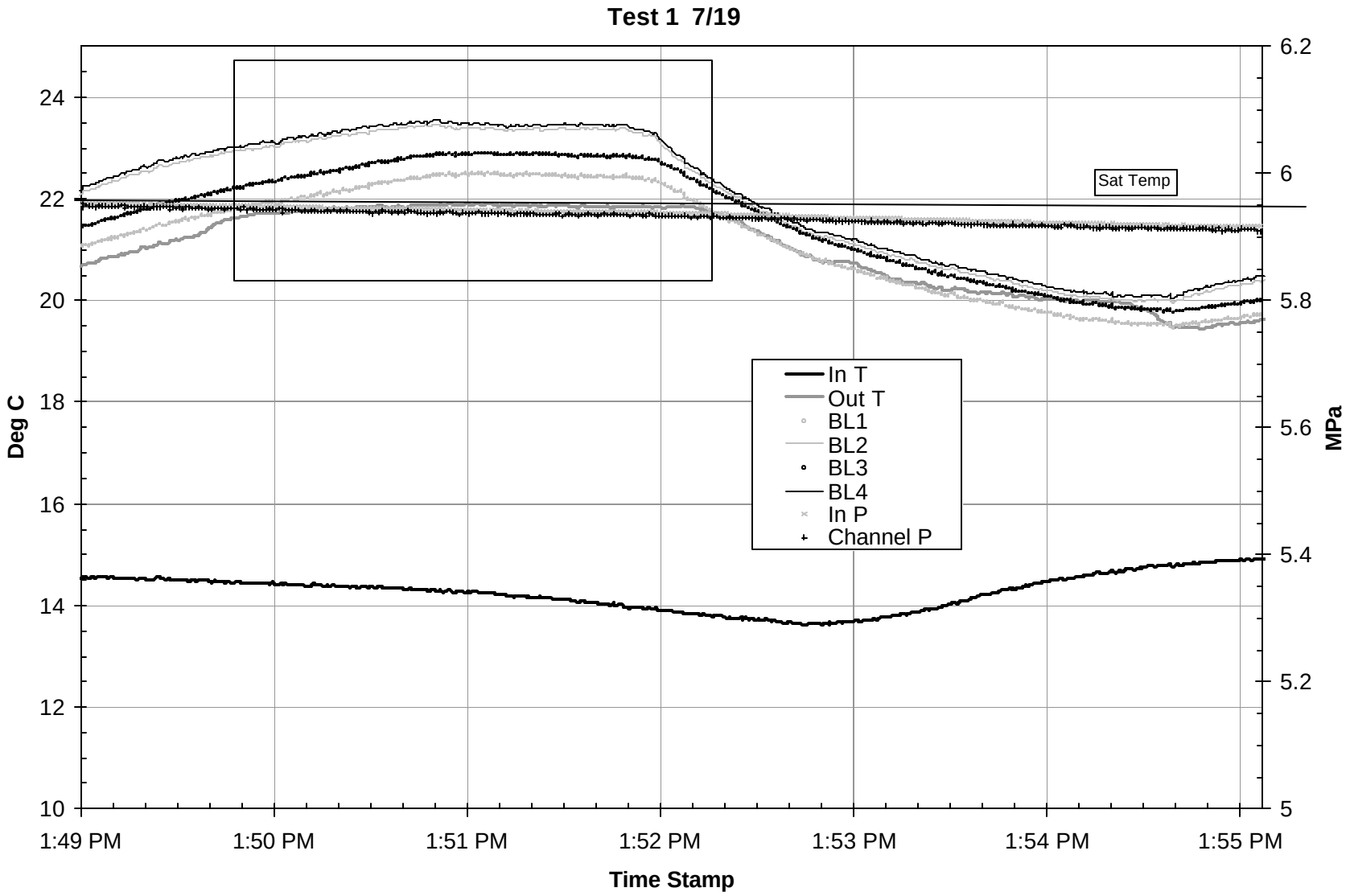
Test 1 7/19
Deg C
MPa
Time Stamp
1:49 PM
1:50 PM
1:51 PM
1:52 PM
1:53 PM
1:54 PM
1:55 PM
10
12
14
16
18
20
22
24
5
5.2
5.4
5.6
5.8
6
6.2
Sat Temp
In T
Out T
BL1
BL2
BL3
BL4
In P
Channel P

Fluoroptic Thermometer Temperature Measurements (deg C)

Sat. Temp = 21.5

Date 7/19 2:00:00 PM Test # 2 MFR 4.2 g/min HBVoltage 41.8

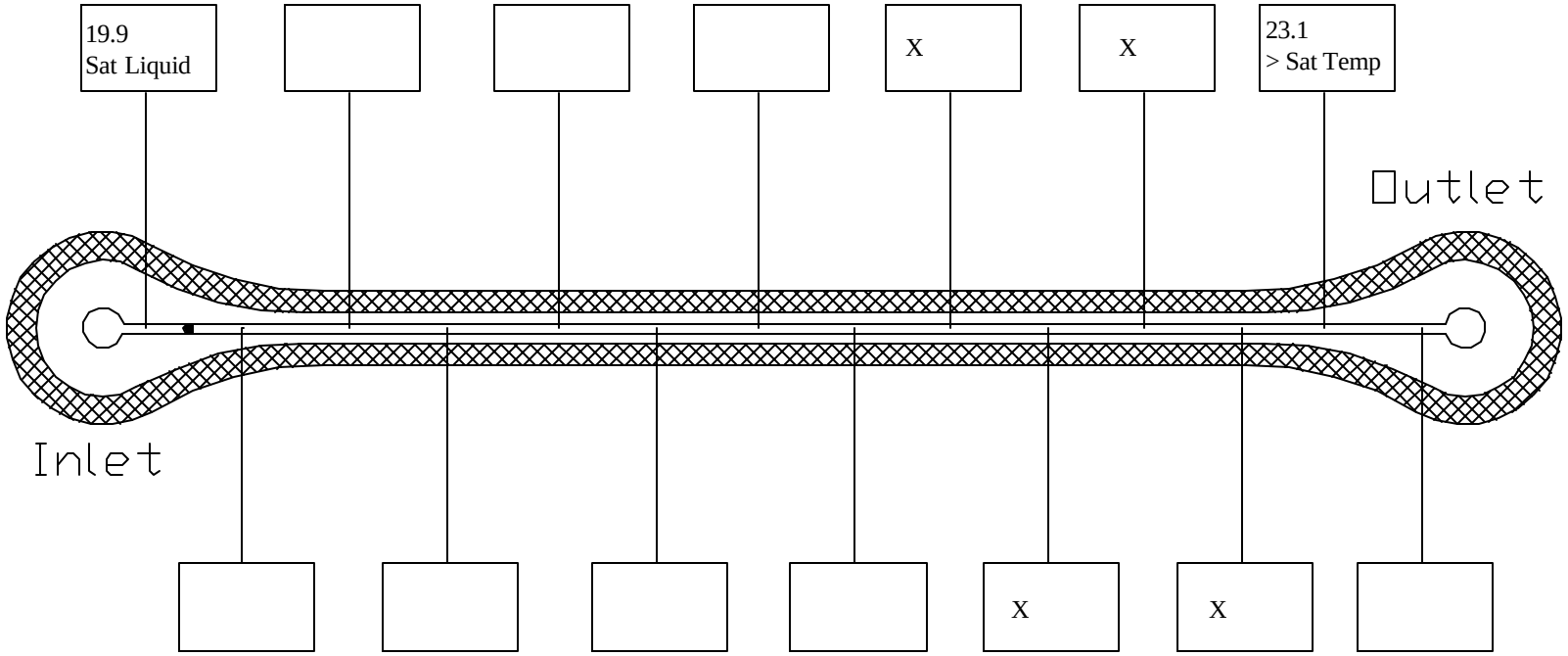

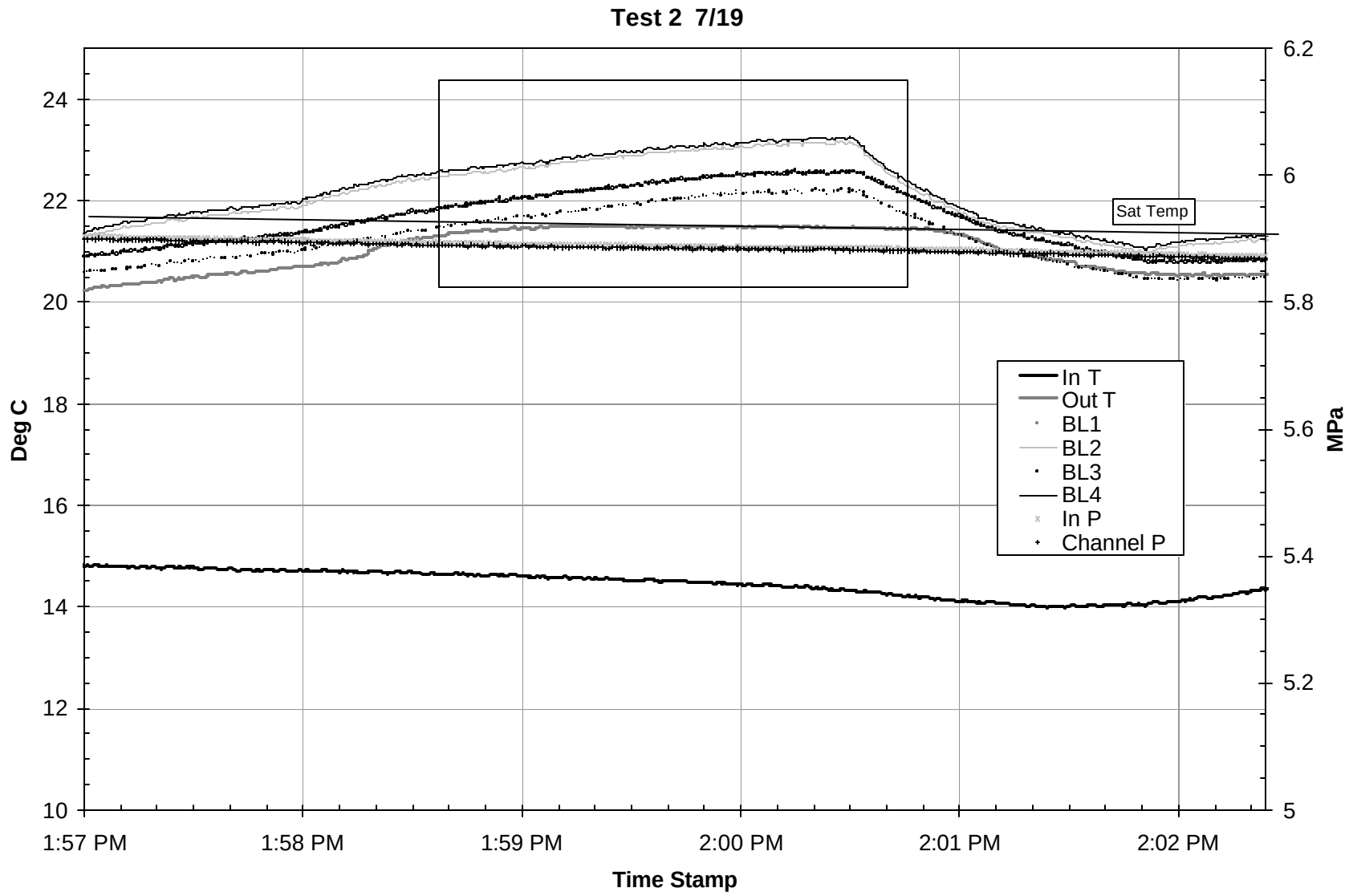
Test 2 7/19
Deg C
MPa
Time Stamp
1:57 PM
1:58 PM
1:59 PM
2:00 PM
2:01 PM
2:02 PM
10
12
14
16
18
20
22
24
5
5.2
5.4
5.6
5.8
6
6.2
Sat Temp
In T
Out T
BL1
BL2
BL3
BL4
In P
Channel P

Fluoroptic Thermometer Temperature Measurements (deg C)

Sat. Temp = 22.0

Date 7/21 10:51:10 AM Test # 1 MFR 3.2 g/min HB Voltage 44.9

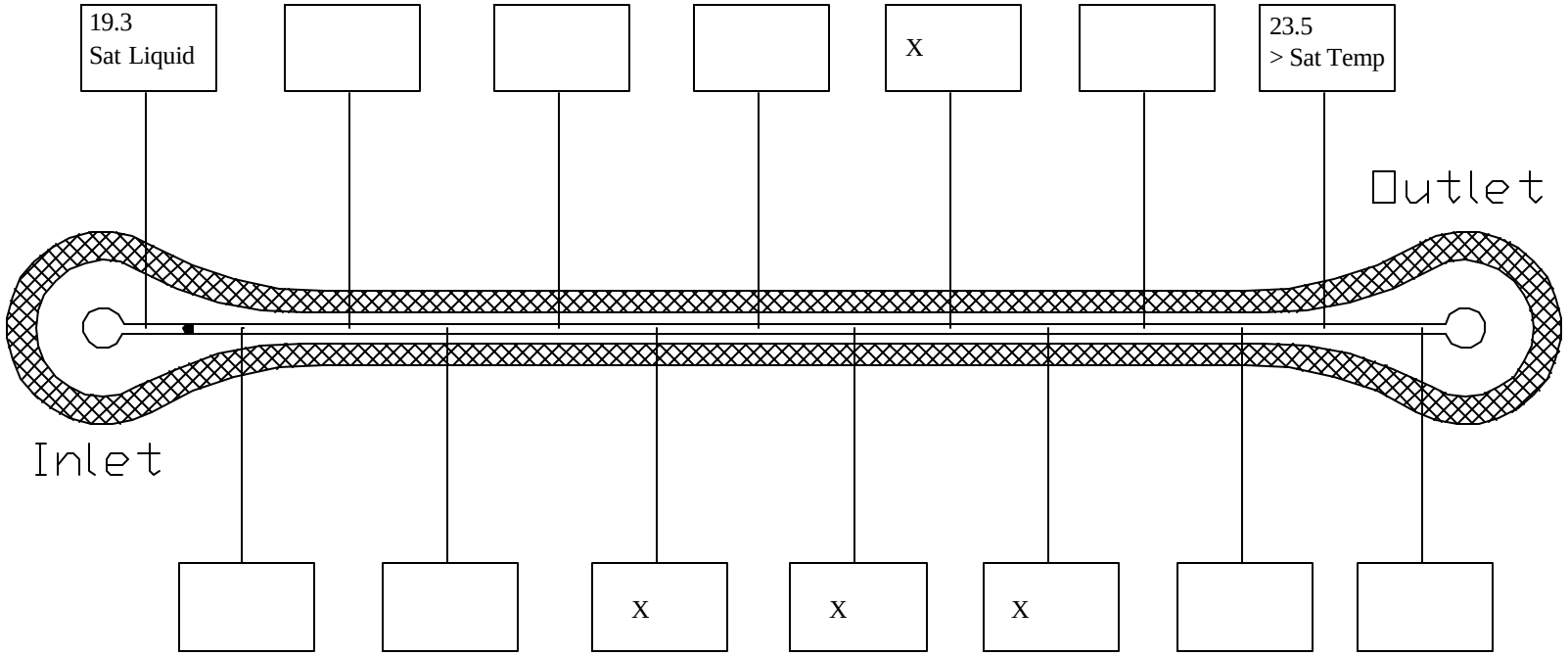

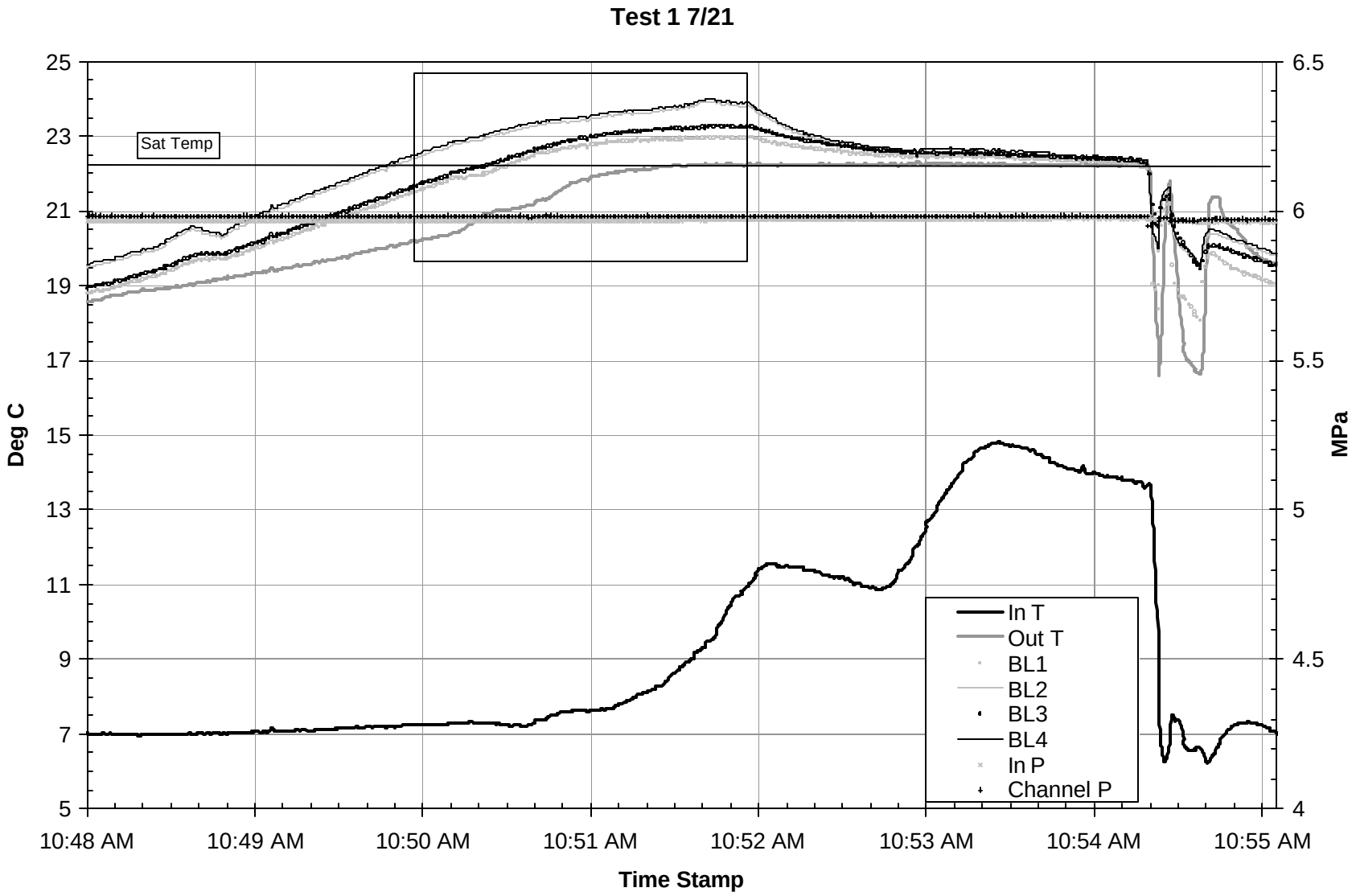
Test 1 7/21
Sat Temp
Deg C
MPa
Time Stamp
10:48 AM
10:49 AM
10:50 AM
10:51 AM
10:52 AM
10:53 AM
10:54 AM
10:55 AM
In T
Out T
BL1
BL2
BL3
BL4
In P
Channel P

Fluoroptic Thermometer Temperature Measurements (deg C)

Sat. Temp = 21.9

Date 7/21 11:00:00 AM Test # 2 MFR 36 g/min HBVoltage 122.1

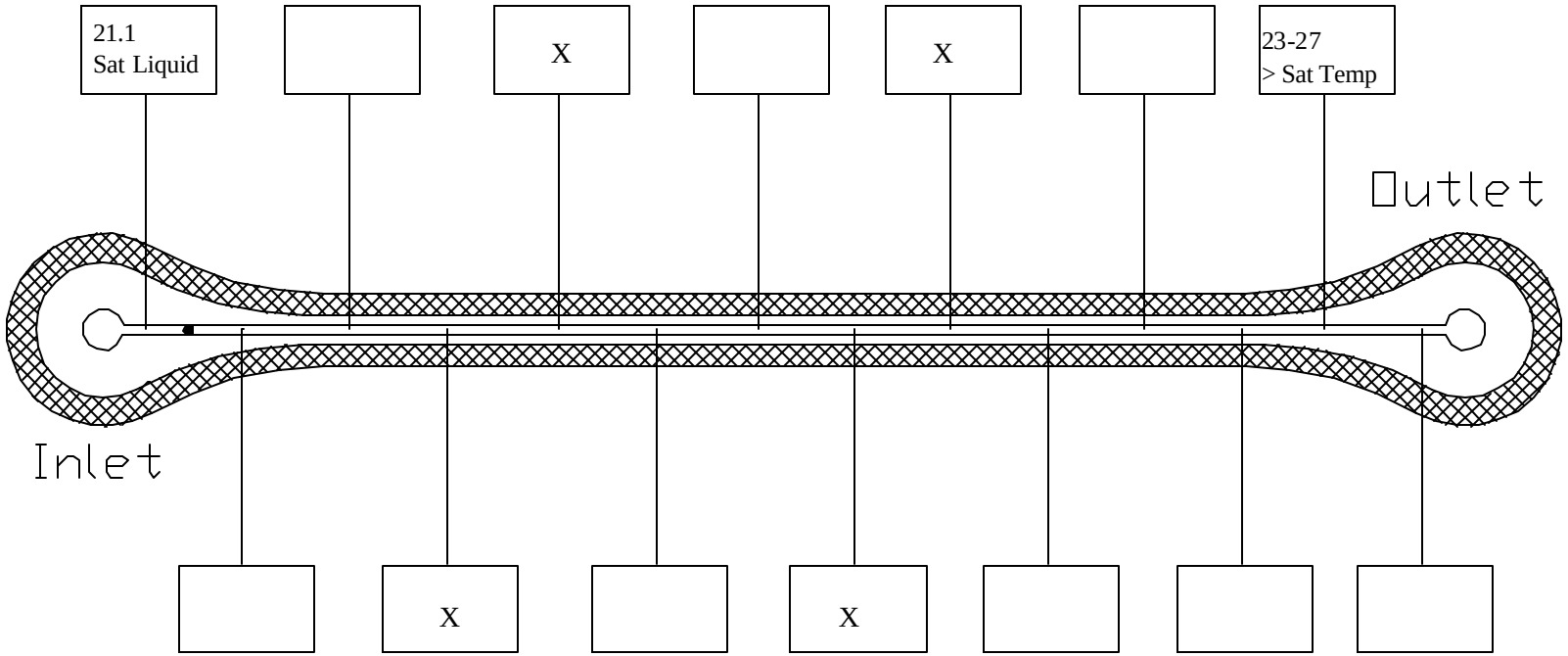

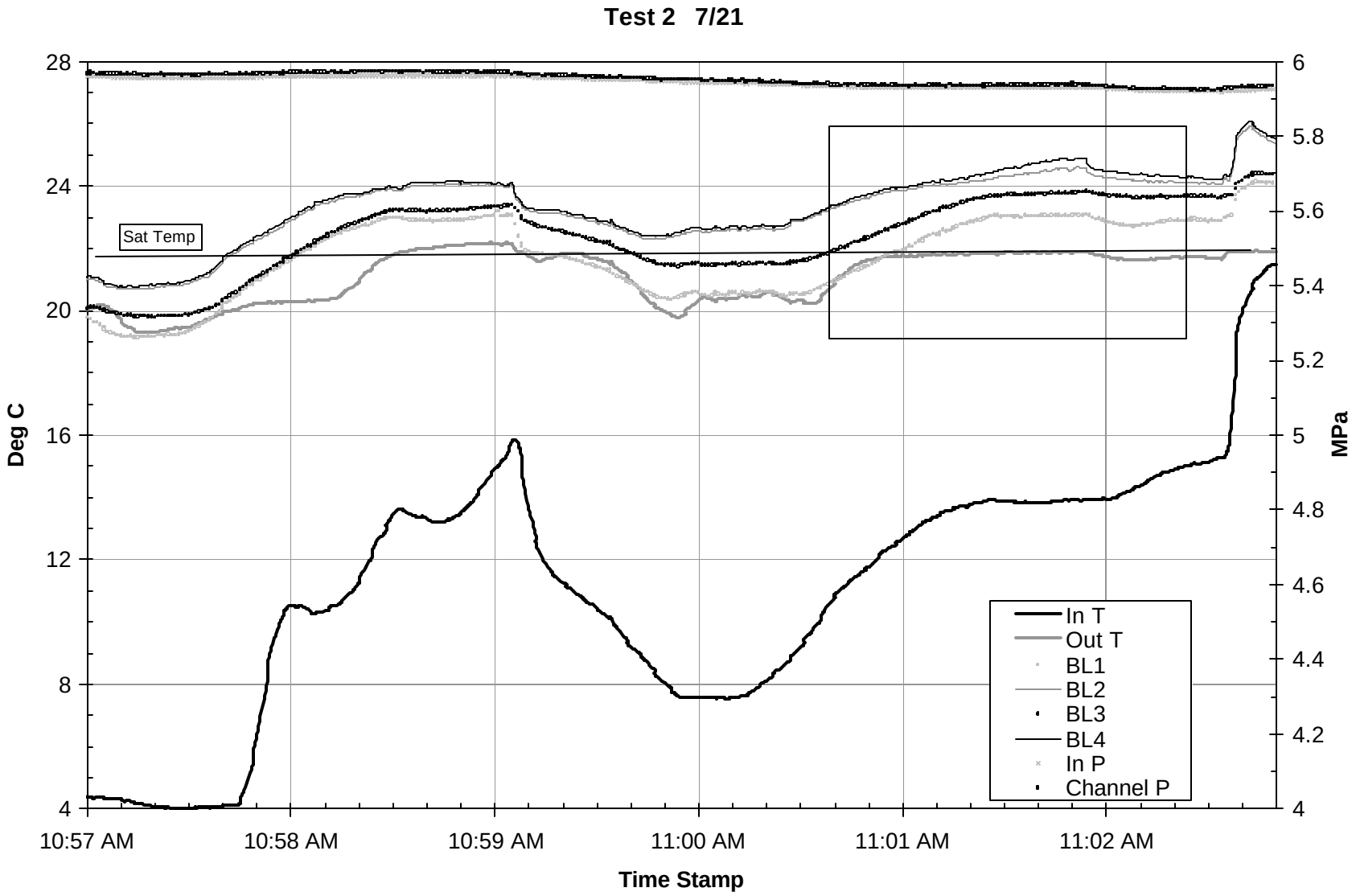
Test 2 7/21
Sat Temp
Deg C
MPa
Time Stamp
10:57 AM
10:58 AM
10:59 AM
11:00 AM
11:01 AM
11:02 AM
28
24
20
16
12
8
4
6
5.8
5.6
5.4
5.2
5
4.8
4.6
4.4
4.2
4
In T
Out T
BL1
BL2
BL3
BL4
In P
Channel P

Fluoroptic Thermometer Temperature Measurements (deg C)

Sat. Temp = 21.3

Date 7/21 11:26:07 AM Test # 3 MFR 9 g/min HBVoltage 40.4

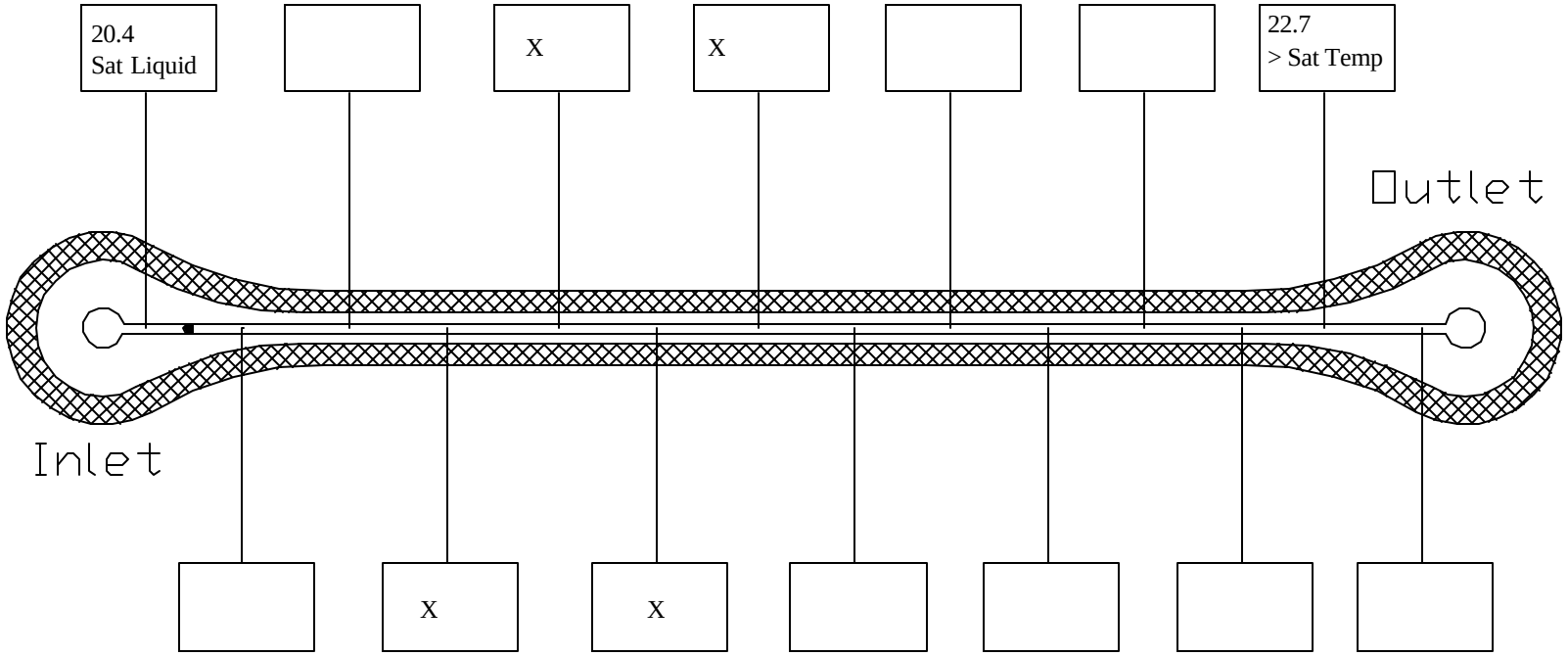

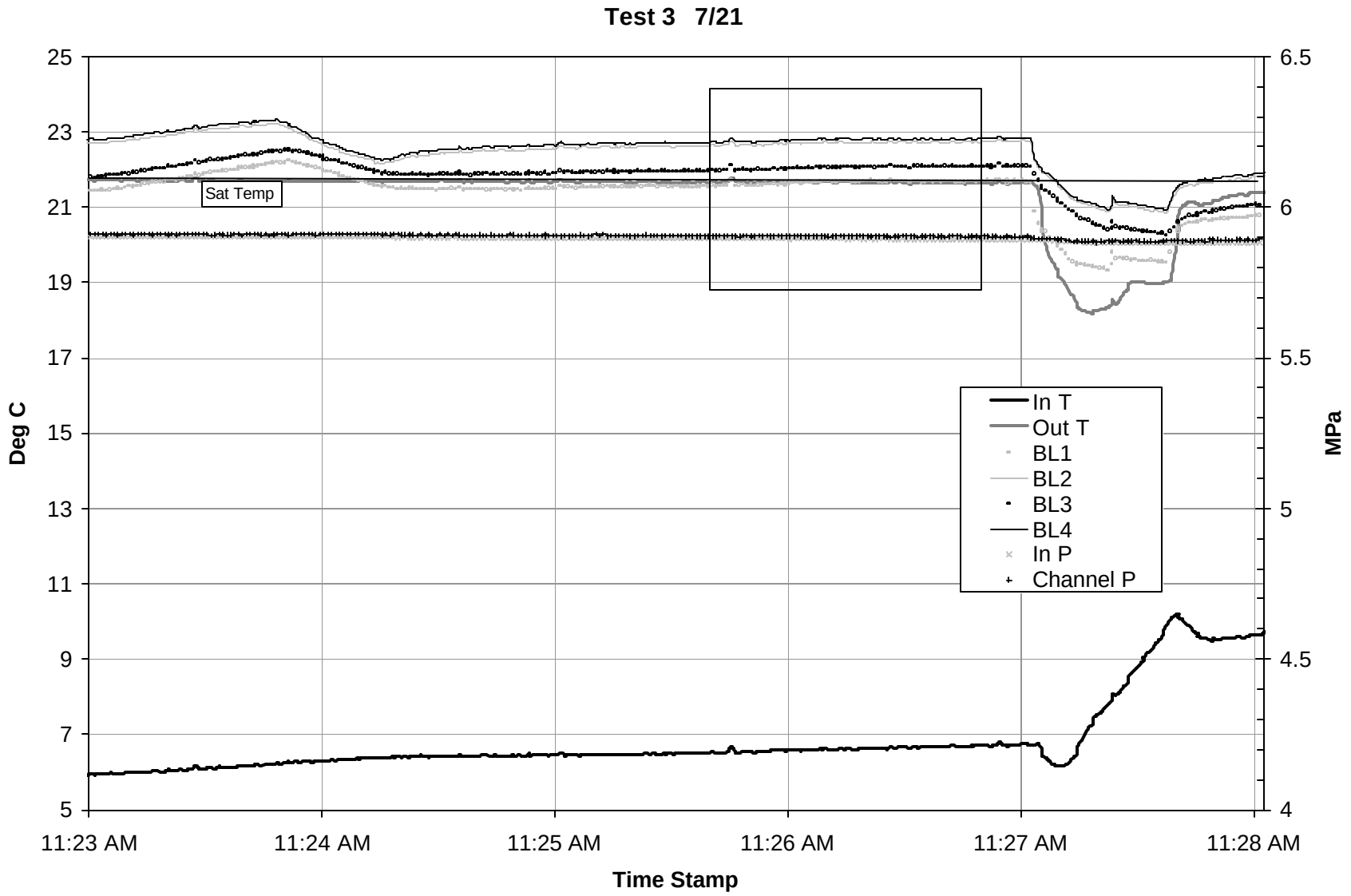
Test 3 7/21
Deg C
MPa
Time Stamp
Sat Temp
In T
Out T
BL1
BL2
BL3
BL4
In P
Channel P
25
23
21
19
17
15
13
11
9
7
5
6.5
6
5.5
5
4.5
4
11:23 AM
11:24 AM
11:25 AM
11:26 AM
11:27 AM
11:28 AM

Fluoroptic Thermometer Temperature Measurements (deg C)

Sat. Temp = 21.0

Date 7/21 11:39:50 AM Test # 4 MFR 30 g/min HB Voltage 102

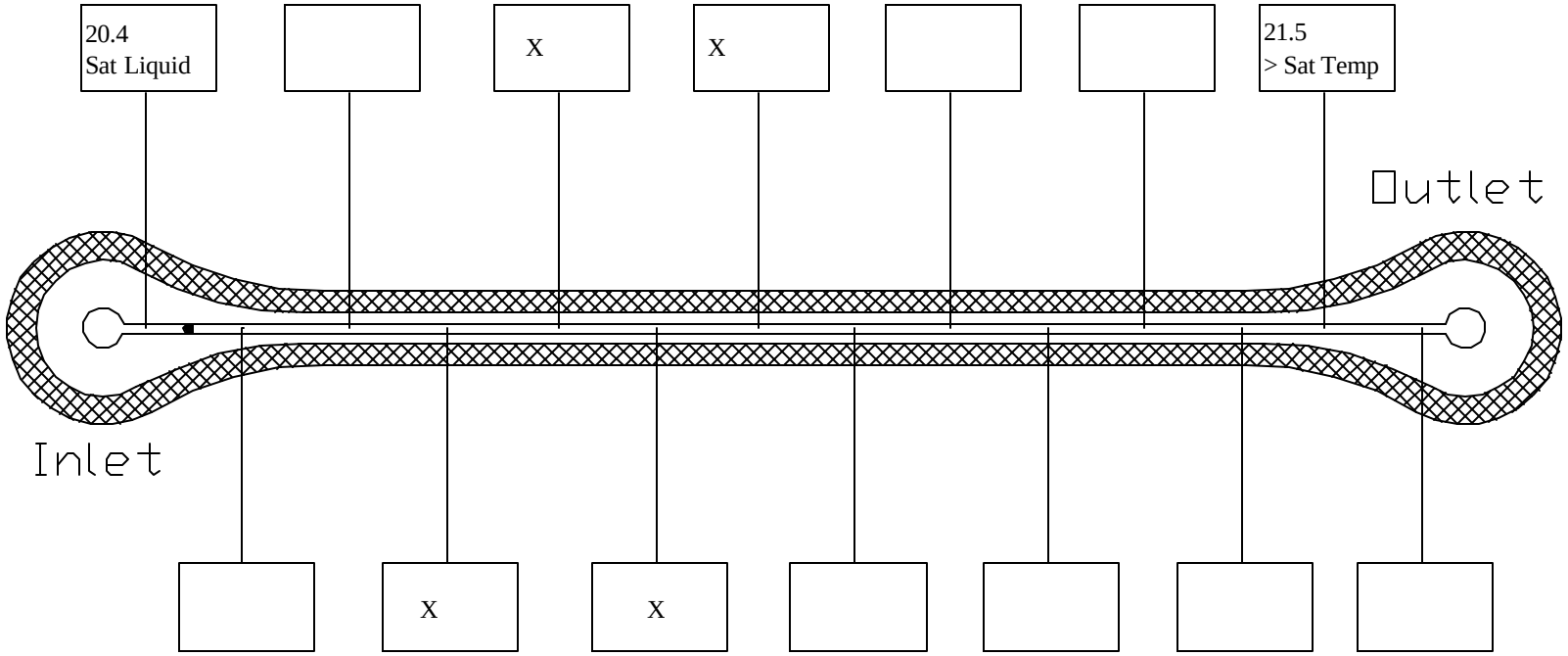

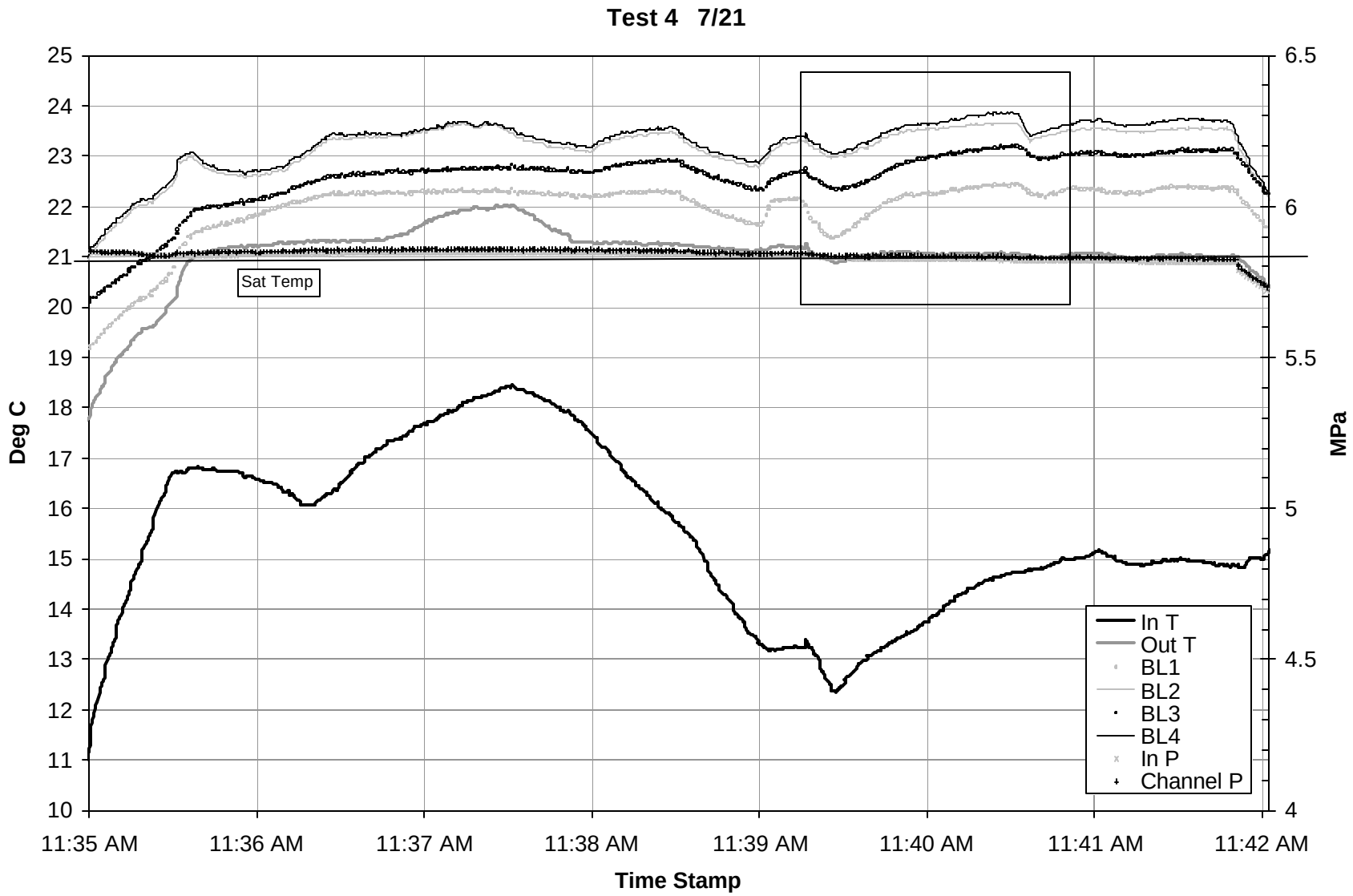
Test 4 7/21
Deg C
MPa
Time Stamp
Sat Temp
In T
Out T
BL1
BL2
BL3
BL4
In P
Channel P
25
24
23
22
21
20
19
18
17
16
15
14
13
12
11
10
6.5
6
5.5
5
4.5
4
11:35 AM
11:36 AM
11:37 AM
11:38 AM
11:39 AM
11:40 AM
11:41 AM
11:42 AM

Appendix B: Calibration and Uncertainty

B.1 Temperature Calibrations

B.1.1 Reference Instrumentation

The following instruments were used as calibration reference sources or reference points while performing the thermocouple calibrations.

B.1.1.1 DP251 RTD Thermometer and Platinum Calibration Probe

Temperature calibrations were performed using an OMEGA DP251 Precision Digital Thermometer with an NIST-traceable, 100-ohm platinum reference probe (PRP-2) as the temperature reference. The DP251 is a Resistance Temperature Device (RTD) electronic thermometer. The probe resistance (R_t) is determined by measuring the ratio (n) of R_t to a reference resistor (R_s):

$$n\,(measured) = \frac{R_t}{R_s\ (known)}$$

$$R_t = n \cdot R_s \qquad \text{(B.1)}$$

The thermometer then references R_t against a stored probe-specific calibration lookup table to determine the probe temperature. The DP251 stated accuracy of the DP251 is 0.01°C (without probe).

The PRP-2 was NIST-calibrated at a frequency of 90 HZ and a constant current of 1.0 mA, in accordance with NIST Technical Note 1265, "Guidelines for Realizing the International Temperature Scale of 1990 (ITS-90)". Total calibration uncertainty is estimated not to exceed 0.005°C with a 95% confidence interval.

All thermocouple calibrations using the PRP-2 reference probe were performed before the 9/00 probe-calibration due date. Total system accuracy is sum of the DP-251 and the reference probe, and is taken as 0.015°C.

B.1.1.2 Electronic Ice Point

Thermocouple signals were routed through the LabVIEW DAS. Unlike the RTD reference probe, accurate interpretation of the thermocouple junction temperature requires a known reference temperature. The total thermocouple voltage read by Labview is the sum of the temperature measuring point (the thermocouple junction) and the terminal junction. Therefore, the associated voltage at a known reference temperature must be subtracted from the input voltage to determine the actual voltage at the thermocouple junction, which can then be used to determine the calibration curve. The SCXI-1300 terminal block comes equipped with an internal cold junction compensation (an integrated circuit which uses NIST calibration curves in conjunction with an amplifier offset to determine the temperature of an isothermal junction block). However, the stated error was ±1.3°C in the desired temperature range, and while thermocouple calibration reduced this error to approximately 0.8°C, this error was found to be unacceptably high. Therefore, a 0°C-ice bath was chosen as the independent temperature reference.

A reference thermocouple was placed in a Dewar containing finely ground ice chips and water, creating a two-phase ice bath. The ice bath voltage was subtracted from each thermocouple undergoing calibration. However, the reference voltage was found to fluctuate significantly, indicating unacceptable temperature gradients within the

Dewar. Therefore, a TRC Ice Point™ Reference Chamber from Omega was used give the reference temperature for the calibration and all subsequent temperature measurements.

The TRC Ice Point™ Reference Chamber maintains an equilibrium of distilled, deionized water and ice at atmospheric pressure to maintain six reference wells at 0°C (with a stated accuracy of ±0.1°C and a stability of ±0.04°C, or better). The wells extend into a thermally and electrically isolated chamber containing the two-phase mixture. The outer wall of the chamber is cooled until an expansion of a bellows indicates an increase in volume produced by the creation of ice crystals within the chamber. A microswitch then shuts off the cooling elements and the chamber thaws until the sensors again start the cooling elements. The alternate freezing and thawing of the ice accurately maintains a 0°C environment around the reference wells. An on-off cycling of a pilot light indicates proper operation of the unit at ice point temperature, and a two-to-three-hours stabilization time is required to reach equilibrium.

B.1.2 Procedure

Temperature calibrations were performed using a temperature bath filled with an equal mixture of 50% water and 50% ethylene glycol by volume. Four 1/32" -diameter block thermocouples (used for determining the channel wall temperature) and the inlet and outlet thermocouples were simultaneously calibrated using the reference probe and thermometer. All thermocouples are grounded, type-K (Chromega®/Alomega®) thermocouples. The thermocouples were attached to the PRP-2 probe using aluminum tape. The tape served the dual purpose of binding the thermocouple junctions as close as possible to the PRP-2 resistance measuring point (ensuring a minimum temperature gradient across the total measuring area of the probe and thermocouples) while providing a sheath against any temperature bath currents.

The expected experimental temperature range was –10C°C to 35°C. The temperature bath was first brought down to the minimum temperature, then calibrations points were chosen at approximately 2 degree intervals to the maximum temperature. At each point the reference temperature was allowed to stabilize before the measurement was taken. Temperature calibrations were made at the 0.01°C resolution, although the 0.001°C resolution was used to check temperature fluctuation at each calibration measurement point. The Labview vi was written so that the raw voltage from each thermocouple was read and logged into a spreadsheet format, allowing data reduction using Excel and EES to determine the voltage-to-temperature curve.

B.1.3 Calibration Results

The LabVIEW data acquisition vi was designed to read each thermocouple voltage, subtract the ice point voltage, then multiply the resulting voltage by the specific thermocouple calibration curve. Signal limit setting reduced the device range (-5 to +5 volts) to voltages corresponding to the maximum and minimum expected temperature (-30 to +40°C) to maximize the resolution of the signal. Each thermocouple voltage-to-temperature reading was transported to the Engineering Equation Solver (EES Version 5.029©) to generate a curve fit. Each curve fit was then inputted into an equation node in the LabVIEW vi. To minimize the curve-fit error, separate curve fits were developed above and below 0°C for the inlet and outlet flow thermocouples (wall thermocouples temperature measurements were not expected to fall below 0°C). Figure B.1 shows the computed thermocouple

junction temperature vs. the RTD reference temperature, and a post-calibration thermocouple reading at known reference temperature.

It is noted fluctuations in the reading may be caused by bath temperature. Similar reading were taken at several temperature between -15°C and 45°C. Statistical analysis shows an accuracy of approximately ±0.05°C within a 95% confidence level for the test shown in Figure B.1. Tests at other reference temperatures fluctuate at approximately ±0.07°C within a 95% confidence level, with greater fluctuations around 0°C. For simplicity and conservatism, the accuracy is taken as ±0.1°C.

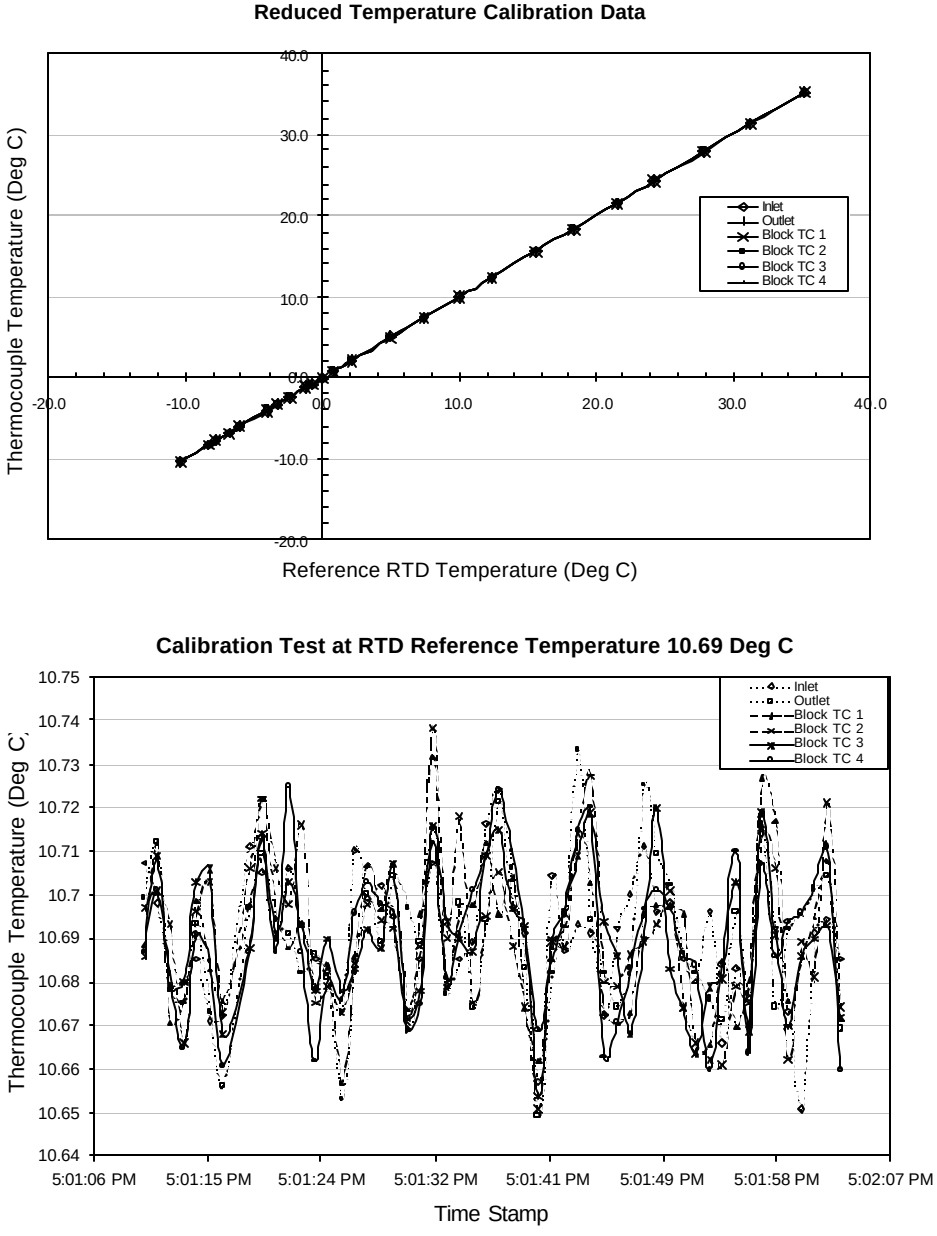

Figure B.1 Thermocouple Vs. Reference Temperature Calibration Curve and Reference Temperature Test

B.4 Uncertainty Analysis

B.4.1 Mass Flux Uncertainty

The Sartorius scale has an accuracy of ±1 gram, and no readout fluctuations were noticed for static measurements. The desired measurement is the decrease in weight over time and not the absolute weight of the source cylinder. Therefore, scale readout uncertainty was not considered a significant source of error. Rather, the significant cause of error in determining the mass flux was establishing and maintaining a stable mass flow rate. As described in Section 4, maintaining a steady flow rate was hindered by flow choking at the exit throttle valve. After several preliminary tests, the best stability achieved was ±5% of the average flow rate for at least 3 minutes leading to the dryout measurement. Because the mass flux is linearly dependent on the mass flow rate, the mass flux uncertainty is estimated as ±5% of the average flow rate.

B.4.2 Heat Flux Uncertainty

Errors associated with the calculating the heat flux from the test section heater are the measurement of the applied voltage to the heater and the dependence of the heater resistance R on temperature. The power cord leading from the variable transformer to the test section was connected to a Fluke Voltmeter that measured the applied voltage. The voltmeter had an accuracy of 0.1 VAC. The dryout measurement was found to be very sensitive to the input voltage. As the voltage increased, the fluoroptic thermometer remained at a constant temperature until the fluctuation representing dryout was observed. If the critical voltage was overshot significantly, all thermocouple readouts and the fluoroptic thermometer display increased in temperature, signifying post-dryout heat transfer. This behavior allowed for accurate measurements of the applied voltage. Voltage measurement error is taken as less than 2% of the measured VAC.

The dependence of R on temperature follows the relation:

$$R = R_o\left(1 + a\left(T - T_o\right)\right) \qquad \text{(B.2)}$$

Where R is the resistance at the measured temperature T, R_o is the resistance at the reference temperature T_o, and α is the temperature coefficient of resistance. The heating element is aluminum, with α = 0.00429 per degree C. The manufacturer states R = 330.6Ω (40 W at 115 VAC) at the reference temperature of 20°C. Under all conditions of dryout, the wall thermocouples temperature never exceeded 30°C. At an estimated maximum blanket temperature of 40°C, R = 359.0Ω. Therefore, R is estimated as 344.8Ω ± 4%.

The applied heat flux to the CO_2 is determined using Equation 4.2. The error associated with determining R and V are statistically independent. Therefore, the error estimated in heat flux is conservatively estimated as the maximum combination of errors associated with the resistance and the voltage, or ±8.4% of the calculated average. Likewise, the error associated with the change in flow enthalpy from the microchannel inlet to the dryout point is ±14.1%, and the error associated with the quality measurement is ±15%. Again, these are conservative estimations.

A summary of the uncertainty is included in Table B.1. These uncertainties are included in Figures 4.2 and 4.3

Table B.1 Estimated Experimental Uncertainty

Parameter	Major Source of Uncertainty	Magnitude of Uncertainty
Thermocouples	Instrument Calibration	±0.1°C
Fluoroptic Thermometer	Instrument Calibration	±0.5°C
CO_2 Absolute Pressure	Instrument Calibration	±0.15%
CO_2 Differential Pressure	Instrument Calibration	±0.15%
CO_2 Thermodynamic Data	Equation of State	±1%
Heat Flux	Resistance and Voltage	±8.3%
Mass Flux	Mass Flow Rate	±5%
Enthalpy Input to Flow	Heat and Mass Flux	±14.1
Quality at Dryout	Heat and Mass Flux	±15.0

Appendix C: Instrumentation

C.1 Transducers and Controls

The following is a list of instrumentation, transducers, controls and hardware used in the test loop and test section:

PID Controller	Toho Electronics, Inc., Model TTM-1520
Pressure Transducer	Setra, Model 206 (Absolute), Omega PX771 (Differential)
Transformers	Payne Model 18-TBP
Scale	Sartorius AG, Model #QC65EDE-SOUR
Glass Window	GE-124 glass, 0.01" tolerance, uncoated
O-ring (Test Section)	-029 Burna-N
Thermocouples	Omega Type K (Chromega®/Alomega®)
Fiber Optic Coupler	ThorLabs C230260P-A, 350-600nm
Fiberoptic Patch Cable	ThorLabs, 2-meter, 600μm/0.39NA FT-600-EMT)
Aspheric Lens Adapter	ThorLabs S1TM09
Lens Tube	ThorLabs SM1L10
1" Optics Mount	ThorLabs KMI-T
Fluoroptic Thermometer	Luxtron® 790
Fluorescent Phosphor	Magnesium Fluorogermanate activated with Tetravalent Manganese

C.2 Data Acquisition Hardware and Software

PCI-MIO-16XE-10

The PCI-MIO-16XE-10 (National Instruments E-Series 6030E) allows up to 100 kS/s data acquisition capability, (the actual streaming rate limited by the PC hard drive). This DAQ devices features up to 16 single-ended or 8 differential analog inputs with 16-bit resolution; two 16-bit voltage outputs (at up to 100 kS/s streaming rate); and 8 digital input/output lines. There are two 24-bit, 20 MHz counter/timers with analog and digital triggering capability. The PCI-MIO-16XE-10 was configured in bipolar mode (± 5V limits) with one digital channel for the multiplexed signal from the SCXI-1000 chassis.

SCXI – 1000

The SCXI-1000 is a compact, 4-slot AC chassis used to house the SCXI-1100 module. This low-noise, forced-air cooled chassis holds up to 4 modules (3 were unused) and uses internal timing bus circuitry for high-speed module multiplexing. The SCXI-1000 integrates all the SCXI module operations, although only the SCXI 1100 was used in these experiments. The SCXIbus in the backplane of the chassis includes guarded analog buses for signal routing and digital buses for transferring data and timing signals.

SCXI – 1100

The SCXI-1100 is a 32 differential-channel multiplexer used for general-purpose analog input applications (mV, V, and current inputs). Current inputs (e.g., the differential pressure gauge) were converted to voltages by

installing resistors on the inputs. The gain and bandwidth settings were configured to condition millivolt and volt signals. The SCXI-1100 multiplexes the 32 conditioned inputs (along with a cold-junction temperature sensor) onto a single channel, which was connected to the SCXIbus for routing to the PCI-MIO-16XE-10 device. The PCI-MIO-16XE-10 24-bit, 20 MHz counter/timers was used to synchronize the scanning

The SCXI-1100 has eight CMOS analog input multiplexers connected to 32 differential analog input channels. The input multiplexers have an input range of ±10 V and overvoltage protection of ±25 V powered on and ±15 V powered off. The SCXI-1100 multiplexes the 32 inputs into a single software-programmable gain instrumentation amplifier (PGIA) allowing gains ranging from 1 to 2,000 (allowing for both voltage-range strain gauge measurements and millivolt-range thermocouple measurements).

SCXI – 1300

The SCXI-1300 is a general-purpose voltage module/terminal block mounted to the front of SCXI-1100 module. The SCXI provided direct transducer connections at screw terminals located within a shielded enclosure, and provided strain relief clamps for the signal wires.

Mounting Rack

The mounting rack was hardwired directly to the SCXI-1300. The rack allowed any combination of 24 thermocouple (8 Type T, 7 Type E, and 9 Type K) and 8 direct voltage inputs to be connected to the input hardware. All thermocouple connects were miniature quick-disconnects made by Omega®. Direct voltage connection were made using standard screw terminal blocks.

LabVIEW 5.0™

Data manipulation was performed using LabVIEW 5.0 by National Instruments©. LabVIEW incorporates a graphical programming platform for the development of data acquisition and control, data analysis, and data presentation virtual instruments (VIs). The VI front panel contains the controls and data displays for the system, including numeric displays, meters, gauges, etc. Control the running VI is performed by using computer inputs (keyboard, mouse, etc.) to manipulate the graphical controls on the front panel.

The instrumentation is graphically programmed using block diagrams. Icons representing subroutines are symbolically wired to pass data from one block to the next. These blocks are used to perform all computations and manipulations, including acquisition and analysis routines, and file I/O operations. These VIs are modular in design and can be incorporated as subroutines into higher-order VIs. Analysis libraries containing statistics, evaluations, regressions, linear algebra, signal generation algorithms, time and frequency-domain algorithms, windowing routines, and digital filters are available for data manipulation and reduction.